Mechanistic Investigations of Photoelectrochemical Water and Methanol Oxidation on Different Titanium Dioxide Single Crystal Surfaces

Der Naturwissenschaftlichen Fakultät der

Gottfried Wilhelm Leibniz Universität Hannover

zur Erlangung des Grades

Doktorin der Naturwissenschaften

Dr. rer. nat.

genehmigte Dissertation

von

M.Sc. Amira Yehya Mohamed Ahmed
geboren am 01.10.1977 in Sohag, Ägypten

2012

Referent: Prof. Dr. Jürgen Caro

Korreferent: Prof. Dr. Detlef Bahnemann

Tag der Promotion: 27.07.2012

Erklärung zur Dissertation

Hiermit erkläre ich, dass ich die vorliegende Dissertation **„Mechanistic Investigations of Photoelectrochemical Water and Methanol Oxidation on Different Titanium Dioxide Single Crystal Surfaces"** als Mitarbeiterin des Institutes für Physikalische Chemie und Elektrochemie der Gottfried Wilhelm Leibniz Universität Hannover selbständig verfasst und alle benutzten Hilfsmittel sowie evtl. zur Hilfeleistung herangezogene Institutionen vollständig angegeben habe.

Die Dissertation wurde nicht schon als Diplom- oder ähnliche Prüfungsarbeit verwendet.

Hannover, 05.06.2012

M.Sc. Amira Yehya Mohamed Ahmed

Acknowledgements

I thank the Egyptian Ministry of Higher Education for granting me a doctoral scholarship (channel system), to get my PhD degree from Germany and Chemistry Department, Faculty of Science at Sohag University for granting me a leave of absence. My kindly thanks go to my Egyptian supervisors Prof. Dr. Fathalla M. El-Cheikh and Prof. Dr. Farouk Rashwan for their continuance support and encouraging me to get my PhD degree from advanced country like Germany.

I sincerely thank Prof. Dr. Jürgen Caro for accepting me as PhD student in the Institute of Physical Chemistry and Electrochemistry at Leibniz University of Hannover, Germany, for his continuance support, and for his kind agreement to act as the referee of my thesis.

My grateful thanks go to Prof. Dr. Detlef Bahnemann at Institute of Technical Chemistry, Leibniz University of Hannover for his fruitful collaboration and discussions and for his very kind agreement to revise and to be the co-referee of my PhD thesis.

My sincere and special thanks go to Dr. Torsten Oekermann for his guidance and supervision, for his fruitful scientific discussions, and for his stimulating support and help during the time course of my PhD work.

My kindly thanks go to Mr. Olivar Merka and Dr. Inga Bannat for the XRD measurements, Mr. Frank Steinbach for the SEM measurements, Mrs. Verena Becker for the AFM measurements, and Dr. Patrick Linder for the fitting program and collaboration. I would like also to express my sincere appreciation to Mrs. Kerstin Janze and Mrs. Yvonne Gabbey-Uebe for their administrative support and to all members of Prof. Caro's group for the very good atmosphere of work.

I am gratefully thanks to my family, special thanks to my husband Tarek Kandiel for his encouragement and support and to my lovely kids Ahmed, Rukaia and Mohamed.

Abstract

To further improve the performance of TiO_2-based photoelectrodes and photocatalysts, a detailed knowledge of the underlying reaction mechanisms on differently oriented surfaces is of high importance. In this study, the photooxidation of methanol in aqueous solution as a model substance for pollutants was investigated on well-defined rutile TiO_2 (100), (001), (110) and anatase TiO_2 (101) single crystals surfaces as well as anatase thin-films prepared by the sol-gel method using intensity-modulated photocurrent spectroscopy (IMPS). The obtained results have been explained with a model combining the theory of IMPS for a bulk semiconductor surface and the nature of the surface-bound intermediates (alternatively surface mobile or immobile $OH_s^{\bullet}$ radicals) and interpreted in view of the influence of the surface structure on the rate constants of charge transfer and recombination. In order to evaluate the meaning of these rate constants for the photocatalytic performance of the different surfaces, photocatalytic activities were determined for methanol photooxidation as well as for the photocatalytic hydroxylation of terephthalic acid, which is usually regarded as an indirect detection of $OH^{\bullet}$ radicals.

The results indicate that water photooxidation proceeds via surface mobile $OH_s^{\bullet}$ radicals on all investigated surfaces, while methanol addition gives rise to the involvement of immobile $OH_s^{\bullet}$ radicals on the rutile (100) and (110) surfaces and the anatase thin-film. Detailed analysis in view of the surface structures suggests that the latter observation is due to efficient hole transfer from bridging $OH_s^{\bullet}$ radicals to methanol, while coupling of two of these radicals occurs in the absence of methanol, making them appear as mobile $OH_s^{\bullet}$ radicals. In case of the rutile (001) and the anatase (101) surfaces, the coupling reaction dominates even in the presence of methanol due to the smaller distance between the bridging $OH_s^{\bullet}$ radicals, leading to less efficient

direct hole transfer from surface $OH_s^\bullet$ radicals to methanol on these surfaces. At the same time, these surfaces exhibit the highest overall photocatalytic activities for $OH_s^\bullet$ radical generation as well as for methanol oxidation. In combination, these results prove that efficient coupling of surface $OH_s^\bullet$ radicals is the main route to the generation of free $OH^\bullet$ radicals in the solution, and that these free $OH^\bullet$ radicals are mainly responsible for the photooxidation of methanol, while direct hole transfer from surface $OH_s^\bullet$ radicals to methanol plays a minor role. This leads to higher photocatalytic activities of surfaces with an efficient coupling of surface $OH_s^\bullet$ radicals and to lower photocatalytic activities of surfaces with an efficient direct charge transfer from surface $OH_s^\bullet$ radicals to methanol, but an inefficient coupling of surface $OH_s^\bullet$ radicals.

Kurzzusammenfassung

Um die Effizienz von TiO_2-basierten Photoelektroden und Photokatalysatoren weiter zu erhöhen, ist eine detaillierte Kenntnis der zu Grunde liegenden Reaktionsmechanismen auf verschieden orientierten TiO_2-Oberflächen von hoher Wichtigkeit. In dieser Arbeit wurde die Photooxidation von Methanol in wässriger Lösung, als Modellsubstanz stellvertretend für organische Schadstoffe, auf wohl definierten Rutil-(100)-, (001)-, (110)- und Anatas-(101)-Einkristalloberflächen sowie auf Sol-Gel-Anatasfilmen mit Hilfe der intensitätsmodulierte Photostromspektroskopie (IMPS) untersucht. Die Ergebnisse wurden mit einem Modell ausgewertet, das die grundlegende IMPS-Theorie für Halbleiteroberflächen mit der Art des oberflächengebundenen Zwischenproduktes der Photooxidation (alternative auf der Oberfläche bewegliche oder unbewegliche $OH^•$-Radikale) verbindet und im Hinblick auf den Einfluss der Oberflächenstruktur auf die Geschwindigkeitskonstanten von Ladungstransfer und Rekombination interpretiert. Um die Bedeutung der verschiedenen Geschwindigkeitskonstanten auf die photokatalytische Gesamteffizienz der verschiedenen Oberflächen zu bewerten, wurden auch die photokatalytischen Aktivitäten der Oberflächen in der Photooxidation von Methanol sowie in der photokatalytischen Hydroxylierung von Terephthalsäure, die oft zum indirekten Nachweis von $OH^•$-Radikalen eingesetzt wird, gemessen.

Die Ergebnisse zeigen, dass die Photooxidation von Wasser auf allen untersuchten Oberflächen über oberflächenbewegliche $OH^•$-Radikale verläuft, während nach der Zugabe von Methanol auf Rutil-(100) und (110)-Oberflächen sowie Anatas-Sol-Gel-Filmen unbewegliche $OH^•$-Radikale eine Rolle spielen. Eine detaillierte Analyse im Hinblick auf die Struktur der Oberflächen ergab, dass die letzte Beobachtung auf effizienten Lochtransfer von Brücken-$OH^•$-Radikalen zu Methanol-Molekülen zurückzuführen ist,

während in Abwesenheit von Methanol die Kopplung zweier solcher Radikale erfolgt, wodurch sie als oberflächenbewegliche $OH^{\bullet}$-Radikale erscheinen. Im Falle der Rutil-(001)- und Anatas-(101)-Oberflächen dominiert die Kopplungsreaktion sogar in Anwesenheit von Methanol. Dies wird durch die günstigere Lage der Oberflächen-$OH^{\bullet}$-Radikale zueinander erklärt, wodurch kaum noch direkter Lochtransfer von Oberflächen-$OH^{\bullet}$-Radikalen zum Methanol stattfindet. Gleichzeitig weisen gerade diese Oberflächen jedoch die höchsten photokatalytischen Gesamtaktivitäten sowohl bei der Erzeugung von freien $OH^{\bullet}$-Radikalen als auch bei der Oxidation von Methanol auf. Die Kombination dieser Ergebnisse beweist, dass die Kopplung von Oberflächen-$OH^{\bullet}$-Radikalen den Haupt-Reaktionsweg zur Erzeugung von freien $OH^{\bullet}$-Radikalen in der Lösung darstellt, und dass diese freien $OH^{\bullet}$-Radikale hauptsächlich für die effiziente Photooxidation von Methanol verantwortlich sind, während der direkte Lochtransfer von Oberflächen-$OH^{\bullet}$-Radikalen zu Methanol-Molekülen eine untergeordnete Rolle spielt. Dies führt zu höheren photokatalytischen Gesamt-Aktivitäten auf Oberflächen mit einer effizienten Kopplung von Oberflächen-$OH^{\bullet}$-Radikalen und zu einer geringeren photokatalytischen Gesamt-Aktivitäten auf Oberflächen mit effizientem direkten Ladungstransfer von Oberflächen-$OH^{\bullet}$-Radikalen zu Methanol aber ineffizienter Kopplung von Oberflächen-$OH^{\bullet}$-Radikalen.

Schlagwörter: Intensitätsmodulierte Photostromspektroskopie (IMPS); Einkristalloberflächen TiO_2; Photoelektroden; Photokatalysatoren; Rutil; Anatas; Ladungstransfer und -rekombinations-Geschwindigkeitskonstanten.

Contents

Contents   ix

1. Introduction

Following the early report on the photoelectrochemical water photolysis at rutile titanium dioxide (TiO_2) single crystal electrodes by Fujishima and Honda in 1972 [1], many studies have been published about water photoelectrolysis at semiconducting metal oxide electrodes, especially on TiO_2, for understanding the photoinduced oxygen evolution process in water splitting reactions [2-5]. Afterwards, the research has been extended to include the photocatalytic water splitting employing powdered anatase TiO_2 suspensions, with Pt deposited on TiO_2 particles as a cathodic catalyst [6-9]. Moreover, the research activities have also been focused on the photocatalytic oxidation of air and water pollutants using TiO_2 photocatalysts [10, 11]. TiO_2 is an n-type semiconductor with the fair probability that the electron-hole pairs created upon irradiation with sunlight may separate, and that the resulting charge carriers might migrate to the surface where they react with adsorbed water and oxygen to produce radical species. These radicals can attack adsorbed organic molecules leading, ultimately, to the complete decomposition of organic pollutants into CO_2 and H_2O. The applications of this process range from purification of wastewaters [12], disinfection based on the bactericidal properties of TiO_2 [13], and self-cleaning coatings [14] to protective coatings [15]. It was even shown that subcutaneous injection of TiO_2 slurry in rats, and subsequent near-UV illumination, could slow or halt the development of tumor cells [16-18]. There are several reviews summarizing what is known about titanium dioxide photocatalysis and photoelectrochemistry [19-26].

The strong oxidizing power of the photogenerated holes, the chemical inertness of the material and its non-toxicity have made TiO_2 a superior photocatalyst and photoelectrode. However, despite the tremendous amount of attention paid to photocatalytic and photoelectrochemical processes

involving TiO_2 from both applied and fundamental viewpoints, many details of the reaction mechanisms are still not fully understood. During the past decades, most photocatalytic studies employing TiO_2 nanomaterials indicate that their photocatalytic activity for the decomposition of organic molecules is an extremely complex matter and appears to depend strongly on both the model substrate and the physical properties of the employed TiO_2 particles [27]. In general, research to examine the surprising differences between the photocatalytic activity of different TiO_2 modifications has so far focused almost exclusively on the comparison of the powdered forms. These studies are important, but by their nature, the powdered forms of TiO_2 are poorly defined, and it is thus almost impossible to draw any conclusive scientific concepts concerning the photocatalytic activities of TiO_2 photocatalysts from this work. Thus, to further improve the performance of TiO_2-based photocatalysts and photoelectrodes, a thorough knowledge of the photocatalytic and photoelectrochemical properties of different well-defined surfaces of different crystal modifications is of high importance.

In this study, the mechanisms of the photolectrochemical oxidation of water and methanol, as a model pollutant, were investigated employing intensity modulated photocurrent spectroscopy (IMPS). Employing this technique, the rate constants of charge transfer and recombination occurring at semiconductor/electrolyte interfaces can be determined. The studies were performed on well-defined surfaces of rutile and anatase TiO_2 single crystals. It was found that the nature of the surface intermediates formed upon illumination depends on the surface structure of the TiO_2 single crystal, and thus, the mechanism and the activity of methanol photooxidation significantly depend on the employed TiO_2 surfaces.

2. Theory

2.1. Basic Principles of Semiconductors

The properties of semiconductors strongly depend on their electronic structure [28, 29]. Due to the essentially infinite number of atoms that must be considered, the electronic structure of these solids is typically discussed in terms of energy bands. The band model stems directly from the picture of atomic energy levels. As described by the Pauli exclusion principle [28, 29], the energy levels of identical overlapping electronic orbitals cannot be equal, and analysis shows that the discrete energy levels of the atoms forming the solid broaden when the orbitals overlap, forming bands of energy levels two times the number of atoms in the crystal [28]. The valence electrons interact with each other in such a way that their sharp atomic energy levels are broadened into wider regions called energy bands. There are two atomic levels, which are of considerable importance: the last occupied and the first unoccupied by electrons. These two atomic levels give rise to two different bands in the solid. The band resulting from the last occupied level is called the valence band (E_{VB}) and that resulting from the first unoccupied level is called the conduction band (E_{CB}). Thus, the valence band will be totally occupied by electrons, whereas the conduction band will be partially or totally free of electrons. The metallic, semiconductor or dielectric properties of a solid are determined by the fact how the two bands are filled by electrons. The difference between the top of E_{VB} and bottom of E_{CB} is called the electronic band gap (E_g). Usually if the (E_g) between valence and conduction bands is in the 1 eV- 4 eV range, the material is considered a semiconductor [30]. Thus, in the semiconductors, the band gap is not so large and the electrons can be transferred into the conduction band, e.g. by thermal excitation. The transferred electrons will behave like electrons in a metal, however, the number of electrons in the conduction band of semiconductors

will be much lower as compared with metals. The excitation of electrons leaves positively charged vacancies in the valence band of the semiconductor, these positively charged vacancies are mobile as well and are normally called "holes". A hole is an empty level in the valence band, or in other words, a valence bond with a missing electron. As a result, the current in semiconductors is made up of two components: the mobile electrons in the conduction band and the mobile holes in the valence band [28]. The electrons can be excited into the conduction band either electrically, thermally, or optically as will be described in detail below.

2.1.1. Optical Properties of Semiconductors

Electrons can be optically excited by absorption of photons which have sufficient energy. Figure 2.1 summarizes the possible optical transitions in a semiconductor [29].
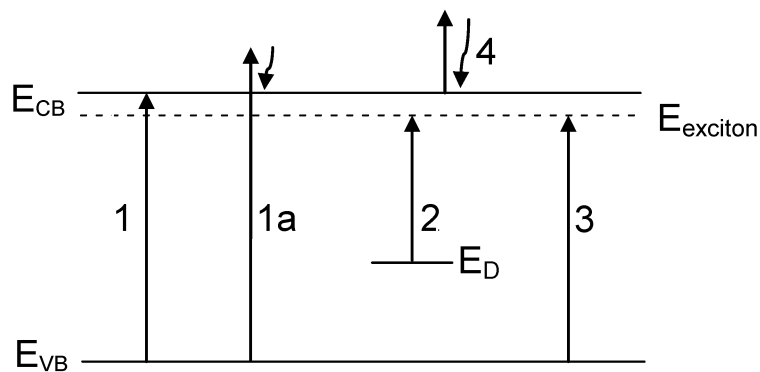
Figure 2.1. Optical transition in a semiconductor [29].

Transition 1 in Figure 2.1 represents the transition from the upper edge of the valance band to the lower edge of the conduction band. The electrons excited into higher energy levels of the conduction band (transition 1a in Figure 2.1) are thermalized to the lower edge of the conduction band within about 10^{-12} to 10^{-13} s. Transition 3 in Figure 2.1 represents the formation of an

exciton, formed by an electron and a hole, as a result of their Coulomb attraction, i.e., it is a neutral quasi-particle, which can move through the semiconductor crystal [29]. Its energy state is close to the conduction band, and it can be split into an independent electron and a hole by thermal excitation. Other electronic transitions are possible upon light excitation. An excitation of an electron from a donor state or an impurity level into the conduction band is feasible (transition 2 in Figure 2.1). However, since the impurity concentration usually is very small, the absorption cross-section and therefore the corresponding absorption coefficient will be smaller by many orders of magnitude than that for a band-band transition. At lower photon energies, i.e., if the photon energy E_{ph} (which is equal to $h\upsilon$, where h and υ are Planck's constant and frequency, respectively) is smaller than E_g, an absorption increase with decreasing E_{ph} has frequently been observed for heavily doped semiconductors. This absorption has been related to an intraband transition (transition 4 in Figure 2.1), and is approximately described by the Drude theory [31]. This free carrier absorption increases with the carrier density. It is negligible for carrier densities below about 10^{18} cm^{-3}.

Usually, the simplest method for probing the band structure of semiconductors is to measure the absorption spectrum [29]. The absorption coefficient, α, is defined as

$$\alpha = \frac{1}{d} \ln \frac{I_0}{I}$$
(Eq. 2.1)

in which d is the thickness of the sample, and I and I_0 are the transmitted and the incident light intensities, respectively. Since the refractive index of semiconductors is frequently quite high, accurate measurements require the determination of the transmission coefficient, as well as the reflection coefficient. Regarding the fundamental interband transition and the corresponding photogeneration of electron-hole pairs, the interband

transitions have to be divided into direct and indirect transitions. The meaning of these terms is as follows:

Within each band the different electron states are characterized not only by their energy E, but also by their momentum p. The electron energy E is a function of the momentum p, which is specific to each crystal and its structure, and to each of its energy bands. In the simplest case, the minimum of $E_{CB}(p)$ and the maximum of $E_{VB}(p)$ occur at $p = 0$. An optical transition from the valence band into the conduction band can occur for $E_{ph} = E_g$ without changing the momentum of the electron (direct transition). The momentum of the photon is in the order of hv/c and is negligible compared to the momentum of an electron (where c is speed of light). There are, however, many semiconductors for which the maxima and minima of the bands do not coincide. The law of conservation of momentum excludes here the possibility of the absorption of a photon of energy close to the band gap. A photon absorption becomes possible, however, if a phonon supplies the missing momentum to the electrons (indirect transition). Such a transition requires a "3-body"-collision (photon, electron, phonon), which occurs less frequently than a "2-body"-collision, i.e. the absorption coefficient will be considerably smaller for a semiconductor with an indirect band gap. Figure 2.2 shows an example of the optical transition in a semiconductor with an indirect band gap transition.
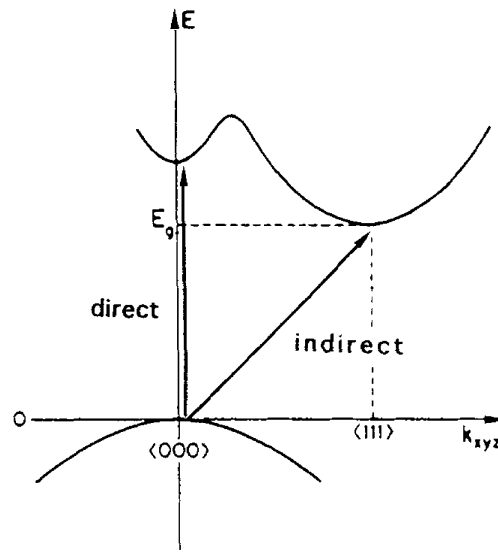
Figure 2.2. Optical transition in semiconductors with an indirect band gap [29].

2.1.2. Doped Semiconductors

Semiconductor single crystals grown from extremely pure material exhibit a low conductivity because of their low carrier density. The latter can be increased by orders of magnitude by doping the material. The undoped semiconductors are known as intrinsic, while doped semiconductors are called extrinsic semiconductors [28-30]. Doped semiconductors with the dominant charge carriers being the electrons are referred to as n-type semiconductors (donor doped), whereas those where the holes constitute the majority are referred to as p-type semiconductors (acceptor doped). A very important concept used to describe the thermodynamic equilibrium of charges in solid state materials is the so called Fermi level (E_F) [29]. The Fermi level is defined as the energy level where the probability of population by an electron is equal to 0.5. In the semiconductors, the occupied and unoccupied levels are separated by a band gap and for example, for an intrinsic semiconductor the

Fermi level lies (at T = 0) at the middle point of the band gap (see Figure 2.3.a).

As it already mentioned, doping changes the energy distribution of electrons, hence, it changes the position of the Fermi level as well [28]. For n-type semiconductors the Fermi level lies just below the conduction band (see Figure 2.3.b), whereas for p-type semiconductors is just above the valence band (see Figure 2.3.c). Such semiconductors are called non-degenerated. However, at very high doping levels the Fermi level may pass the band edge of the conduction or valence band of the semiconductor, respectively. In this case, the semiconductor becomes degenerated and shows a metal-like behavior.
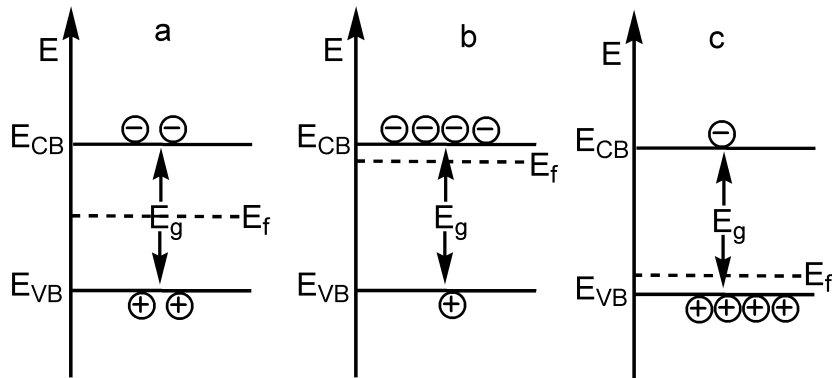

Figure 2.3. Band diagram of (a) intrinsic semiconductors, (b) n-type semiconductors, and (c) p-type semiconductors [29].

For the non-degenerated semiconductors, the electron concentration in the conduction band and the hole concentration in the valence band are related to the Fermi energy E_F [30] and to the effective densities of states in the conduction and valence bands (N_{CB} and N_{VB} respectively) by [30]:

$$n = N_{CB}e^{-(E_{CB}-E_F)/k_BT}$$ (Eq. 2.2.a)

$$p = N_{VB}e^{-(E_F-E_{VB})/k_BT}$$ (Eq. 2.2.b)

2.1.3. The Semiconductor/Electrolyte Junction

When a semiconductor is immersed in a redox electrolyte, the electrochemical potential (Fermi level) is disparate across the interface. Equilibration of this interface thus necessitates the flow of charge from one phase to the other and a ''band bending'' ensues within the semiconductor phase. The situation before and after contact of the two phases is illustrated in Figure 2.4.a and b for an *n*-type and *p*-type semiconductor, respectively. After contact, the net result of equilibration is that $E_F = E_{F,redox}$ and a ''built-in'' voltage, $\Delta\phi_{SC}$ develops within the semiconductor phase, as illustrated in the right hand frames of Figure 2.4.a and b.
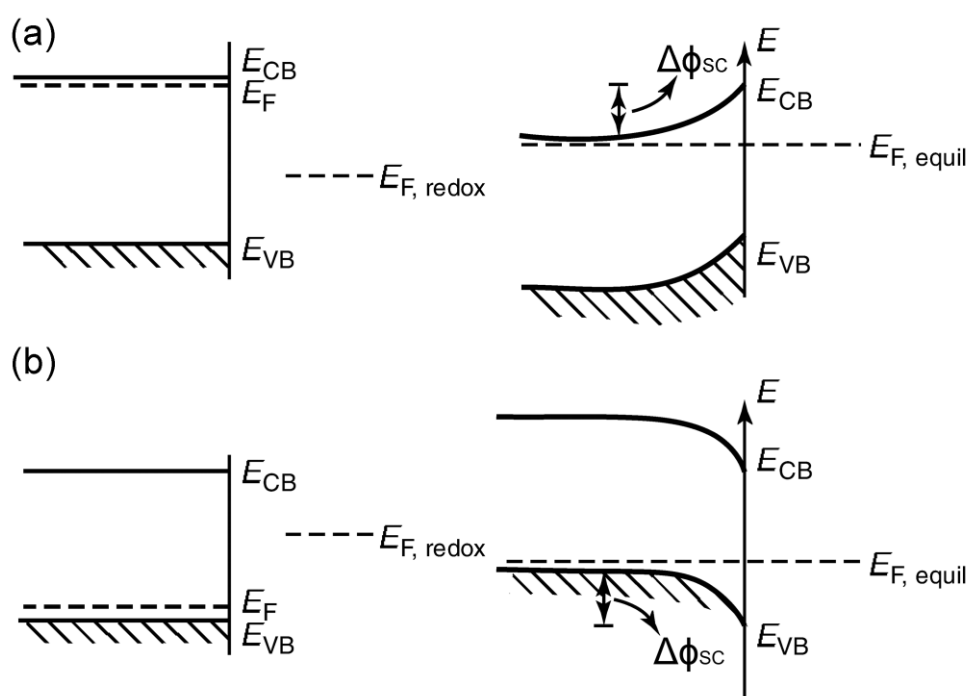

Figure 2.4. The semiconductor-electrolyte interface before and after equilibration (i.e. contact of the two phases) shown for (a) a *n*-type semiconductor, (b) a *p*-type semiconductor [30].

Considering an *n*-type semiconductor for illustrative purposes (Figure 2.4.a), the electronic charge needed for Fermi level equilibration in the semiconductor phase originates from the donor impurities (rather than from bonding electrons in the semiconductor lattice) [30]. Thus, as a consequence within the semiconductor a surplus of positive charges results from these ionized donors. The Fermi level in the semiconductor ($E_{F,n}$) moves ''down'' (i.e., to a lower energy), and the process stops when the Fermi level is the same on either side of the interface.

There is a characteristic region near the semiconductor surface from which the charge is removed by the equilibration process. Beyond this boundary in the bulk of the semiconductor, the ionized donors (for an *n*-type semiconductor) have their compensating charge (electrons), and the semiconductor as a whole is electrically neutral. This layer near the surface is called space charge region or depletion layer, so termed because the layer is depleted of the majority carriers [30]. The potential distribution in this interfacial region can be quantified by relating the charge density and the electric field strength $\Delta\phi$ as embodied by the Poisson equation [32, 33]:

$$\Delta\phi(x) = \left(\frac{qN_D}{2\varepsilon\varepsilon_0}\right)x^2 \qquad (0 \leq x \leq W) \qquad \text{(Eq. 2.3)}$$

In Eq.2.3, q is the electronic charge, ε_0 the vacuum permittivity, ε is the dielectric constant of the semiconductor and W the width of the space charge layer. The potential distribution across the whole semiconductor / electrolyte interface, i.e., the space charge layer in the semiconductor and the Helmholtz and Gouy layers in the electrolyte, is mapped in Figure 2.5.
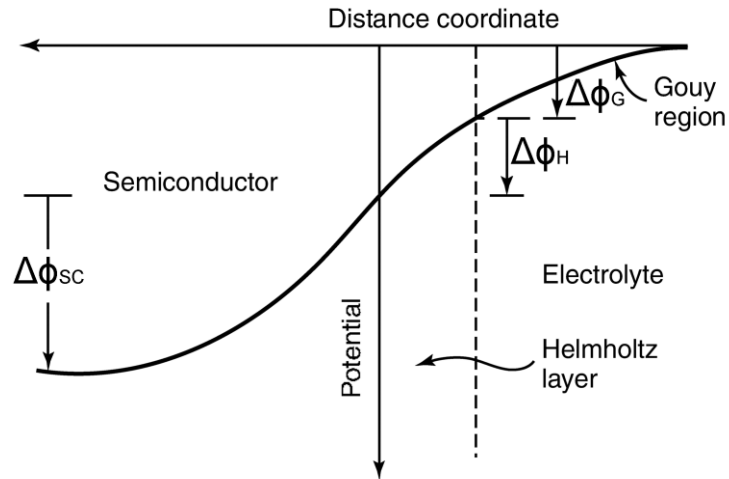
Figure 2.5. Electrostatics at a semiconductor–electrolyte interface [30].

The thickness of the depletion layer is related to the potential drop between the bulk and the surface of the semiconductor, $\Delta\phi_{SC}$, by the following expression:

$$W = \sqrt{\frac{2\Delta\phi_{SC}\varepsilon\varepsilon_0}{qN_D}}$$
(Eq. 2.4)

It is obvious from Eq. 2.4 that the magnitude of W should depend on the semiconductor doping level N_D. Consider two cases of a semiconductor, one that is lightly doped (say $N_D \sim 10^{16}$ cm^{-3}) and another that is heavily doped ($N_D \sim 10^{18}$ cm^{-3}). Obviously, in the former case, the charge needed for Fermi level equilibration has to come from deeper inside the solid and so the magnitude of W will be larger. This suggests a strategy for chemical control of the electrostatics at the semiconductor–electrolyte interface [34]. Nominal dimensions of W are in the 10–1000 nm range. This may be compared with the corresponding Helmholtz layer width, typically 0.4–0.6 nm [30]. With the capacitor-in-series model, the semiconductor space charge layer is usually the determining factor in the total capacity of the interface. As shown in Figure 2.5, when a semiconductor is brought into contact with an electrolyte solution,

besides the space charge region in the semiconductor, a charged layer is also present on the electrolyte side called electrical double layer or Helmholtz layer [28-30]. This layer is formed as a results of adsorption of ions at the electrode surface causing a corresponding potential $\Delta\phi_H$ across the interface. It partly consists of specifically adsorbed ions (inner Helmholtz layer) and in addition of solvated ions (outer Helmholtz layer). Assuming for instance that the formation of the inner Helmholtz layer is due to the reaction of the electrode with the solvent, then an outer Helmholtz layer may be formed due to electrostatic forces resulting from solvated ions of a supporting salt added to the electrolyte. At high concentrations of the supporting salt all of these charges are concentrated within the outer Helmholtz layer, at low concentrations the charges are distributed over a much thicker diffuse layer known as Gouy layer [28-30]. The capacity of the Gouy layer is much lower than the Helmholtz layer capacitance for ion concentrations higher than 10^{-3} M. Accordingly, any potential drop across the Gouy layer can be neglected for higher ion concentrations. Since in experiments with semiconductor electrodes, the occurrence of a Gouy diffuse double layer complicates the analysis of the data, only solutions containing a high concentration of a supporting salt ($>10^{-2}$ M) are used.

2.2. Semiconductor Photoelectrochemistry

The foundations of semiconductor electrochemistry were laid more than forty years ago [33-37], but initially semiconductor photoelectrochemistry remained a rather academic topic. An excellent overview of work up to 1980 has been given by Morrison [28]. Interest in potential applications of photoelectrochemistry was triggered in the 1980s by suggestions that semiconductor/electrolyte junctions could be used for solar energy

conversion. Development of this concept led to the development of regenerative photovoltaic cells based on redox electrolytes, and the 1980s saw a rapid expansion of activity in semiconductor photoelectrochemistry [38]. In the early 1990s Grätzel and co-workers developed the efficient dye-sensitized nanocrystalline TiO$_2$ cells [39-41]. As a consequence, the photoelectrochemical properties of nanocrystalline semiconductor electrodes have become the subject of widespread research activity. Light driven electron transfer is central to many important processes. In the following the electron transfer in the dark and under illumination will be discussed.

2.2.1. Electron Transfer at Semiconductor Electrodes in the Dark

For an n-type semiconductor electrode immersed in solution in the dark, the rate of electron transfer does not only depend on the concentration of redox species in the solution but also on the potential-dependent density of electrons at the surface of the semiconductor electrode (n_s). Under depletion conditions, i.e., when the surface electron density is depleted with respect to the bulk concentration being much higher than the surface hole density, most of the potential drop is located in the solid, hence, to a good approximation the activation energy for the electron transfer will be independent of the potential. The electron transfer at semiconductor electrodes is therefore characterised in terms of a second order heterogeneous rate constant (k) with units cm^4 s^{-1} where the electron flux is defined as $kc_{ox}n_s$ using the unit cm^{-3} for c_{ox} and n_s [32, 42]. Under ideal conditions, the electron concentration (n_s) at the surface varies exponentially with the potential, E, according to the Boltzmann equation [32, 42]:

$$n_s = n_{bulk}e^{-q(E-E_{FB})/k_B T} \qquad\qquad \text{(Eq. 2.5)}$$

2.2.2. Electron Transfer at Illuminated Semiconductor Electrodes

When a photon with an energy exceeding that of the band gap is absorbed in a semiconductor, an electron is promoted from the valence band to the conduction band, creating an electron hole pair. In an n-type semiconductor, the electron is the majority carrier and the hole is the minority carrier. The minority carrier is not a stable species; it will eventually recombine with an electron returning from the conduction band to the valence band. Since, by definition, majority carriers are in large excess, the recombination process in the bulk (uncharged) region of the semiconductor is pseudo-first-order and characterized by the lifetime, τ_p or τ_n for electrons or holes respectively [21]. In contrast to the situation in the dark, where only majority carrier reactions can take place at any appreciable rate, photogenerated minority carriers generally take part in photoelectrochemical reactions. Formulation of the kinetics of photoelectrochemical reactions are complicated by the fact that the rates depend on the concentration of minority carriers at the interface, and this is not known a *priori*. It depends on the potential, the illumination intensity, the concentration of redox species and the rate constant for interfacial electron transfer.

In the following, the generation and collection of photogenerated minority carriers is discussed for the case of n-type semiconductors, where holes generated by absorption of light in the bulk of the semiconductor are collected at the interface by diffusion and migration. Under depletion conditions, electrons are withdrawn from the surface, leaving a space charge region due to ionized electron donors in the crystal lattice. The electric field in the space charge region will drive holes to the surface, where they can take part in electron transfer reactions. Holes generated deeper in the bulk of the semiconductor can reach the edge of the space charge region by diffusion or

they may be lost by recombination with electrons. As shown in the Figure 2.6, the generation/collection problem is defined in terms of three characteristic lengths: the width of the space charge region as defined in Eq. 2.3, the penetration depth of the light $1/\alpha$ and the diffusion length of holes $L_p=(D_p\tau_p)^{1/2}$, where τ_p is the hole lifetime and D_p is the hole diffusion coefficient [43].
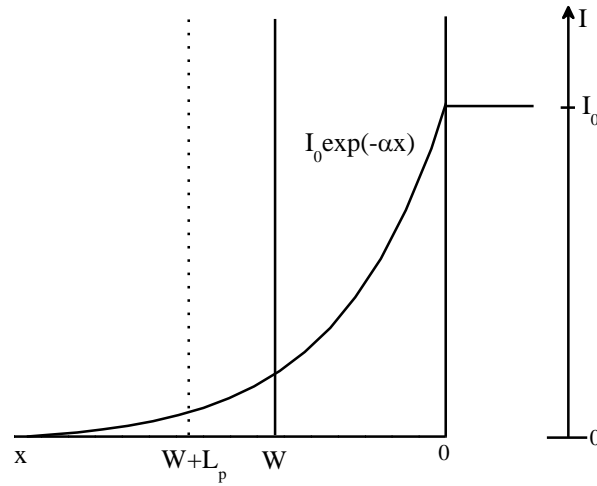

Figure 2.6. Profile of light intensity (I) at the semiconductor electrolyte junction. W is the width of the depletion layer and L_p is the hole diffusion length. The penetration depth of the light is defined as $1/\alpha$ [21].

The solution of this boundary value problem was given originally by Gärtner [44] for the solid state junction. It is assumed that holes generated within the space charge region are all collected at the contact and that holes generated in the neutral region are swept rapidly to the surface when they reach the edge of the space charge region, so that their concentration at $x=W$ approaches zero. The so-called Gärtner flux, g_1, of holes at $x=0$ and therefore the measured photocurrent is linearly dependent on I_0, the incident photon flux (corrected for reflection):

$$j_{photo} = qg_1 = qI_0\left(1 - \frac{e^{-\alpha W}}{1+\alpha L_p}\right)$$ (Eq. 2.6)

The Gärtner equation (Eq. 2.6) provides a satisfactory description of the photocurrent-voltage-curves measured at many semiconductor electrodes, but it contains no information about electron transfer kinetics because its derivation involves an a *priori* assumption concerning the boundary conditions.

Under steady state conditions, the concentration of holes at the surface is determined by the rate of their flux from the bulk and the rate of their removal by electron transfer and surface recombination. It is usually assumed that the potential distribution across the semiconductor/electrolyte junction is not affected by illumination under potentiostatic conditions, so that W is independent of I_0. In fact, W may change under illumination due to the release of carriers from traps or due to charge accumulation at the interface.

2.3. Titanium Dioxide Photocatalysis and Photoelectrochemistry

In the previous sections, the basics of semiconductor photochemistry have been briefly described. In this section a brief summary of the photocatalytic and the photoelectrochemical oxidation mechanisms of water and methanol on TiO_2 will be presented. Since it is highly expected that the mechanisms strongly depend on the crystal and surface structures of TiO_2, the different phases and surface structures of TiO_2 will also be presented.

2.3.1. Crystal Structure of TiO_2

Due to the mixed ionic and covalent bonding in TiO_2, the surface crystal structure has an even stronger influence on local surface chemistry as compared to metals or elemental semiconductors [26, 45]. Titanium dioxide crystallizes in three different major structures; rutile, anatase and brookite. Among the three modifications, rutile and anatase have been extensively studied because of their fundamental and practical interests. Rutile is

thermodynamically more stable, while anatase is more widely used in practice, as small particles tend to form as anatase unless annealed at high temperature. Both rutile and anatase are fundamentally made up of [TiO_6] octahedrons, but the modes of arrangement as well as of the distortion are different. In rutile, [TiO_6] octahedrons link by sharing an edge along the c axis to form chains, which are further linked by sharing vertices to form a three-dimensional structure. In anatase, the three-dimensional framework is assembled only by edge-shared bonding among the [TiO_6] octahedrons. Figure 2.7 illustrates the bulk structure of anatase and rutile [46]. In view of the different constructions of [TiO_6] octahedrons, the surface chemistry is expected to be significantly different for rutile and anatase. For example, theoretical calculations predict that water is molecularly adsorbed on anatase (101)[47], while on rutile (110) it is dissociatively adsorbed at low coverage [48].
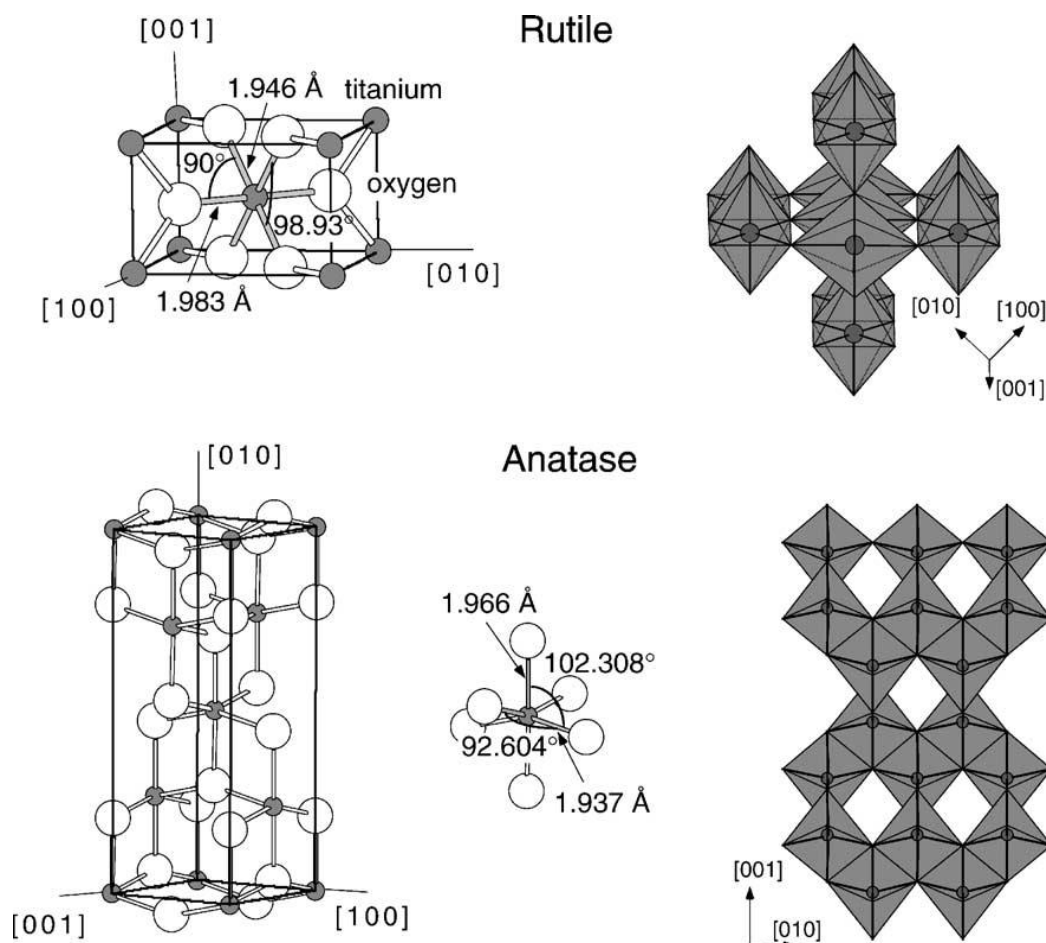
Figure 2.7. Bulk structures of rutile and anatase. The tetragonal bulk unit cell of rutile has the dimensions, $a = b = 4.587$ Å, $c = 2.953$ Å, and the one of anatase $a = b = 3.782$ Å, $c = 9.502$ Å. The bond lengths and angles of the octahedrally coordinated Ti atoms are indicated and the stacking of the octahedra in both structures is shown on the right side [46].

2.3.2. Structure of Different TiO$_2$ Surfaces

The energetics of several low-index surfaces of TiO$_2$, using first-principles total-energy calculation methods, have been calculated by Ramamoorthy *et al.* [49]. The calculations indicate that the (110) surface has a much lower surface energy than the (001) surface. The (100) and (011) surfaces have surface energies lying in between these extremes. The (100) surface is clearly stable with respect to forming facets of the (110) orientation, while the (001)

surface appears to be marginally stable with respect to forming macroscopic (011) facets. From the calculated energies a three-dimensional (3D) Wulff plot was constructed as shown in Figure 2.8. The Wulff construction yields the equilibrium crystal shape of a macroscopic crystal. For comparison with experimental crystal shapes one has to take into account that only four planes were considered and that the calculations are strictly valid only at absolute zero. For rutile, the (110), (001) and (100) surfaces have been studied, with (110) being the most stable. For anatase, typically, (101) and (100)/(010) surface planes are found, together with some (001) [46, 47]. Several theoretical studies have predicted the stability of the different low-index anatase surfaces [47, 50]. The (101) face is the thermodynamically most stable surface as concluded from the calculated surface energies values [46, 51, 52]. The calculated Wulff shape of an anatase crystal, based on these values, compares well with the shape of naturally grown mineral samples as shown in Figure 2.9.a and b [53].
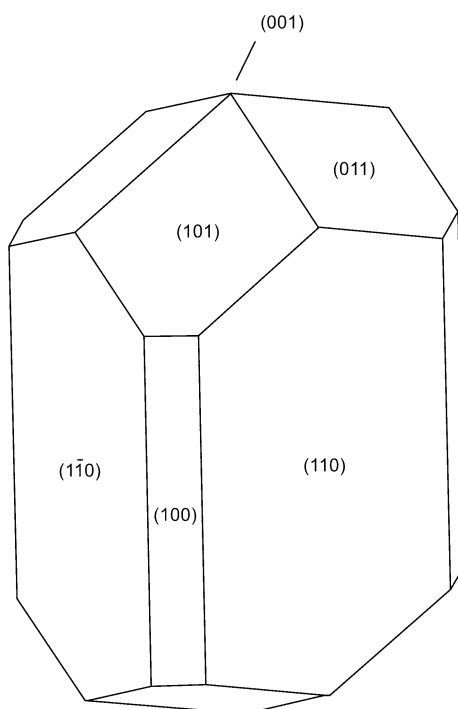

Figure 2.8. The equilibrium shape of a macroscopic crystal of TiO_2 using the Wulff construction and the surface energies reported in ref. [49].
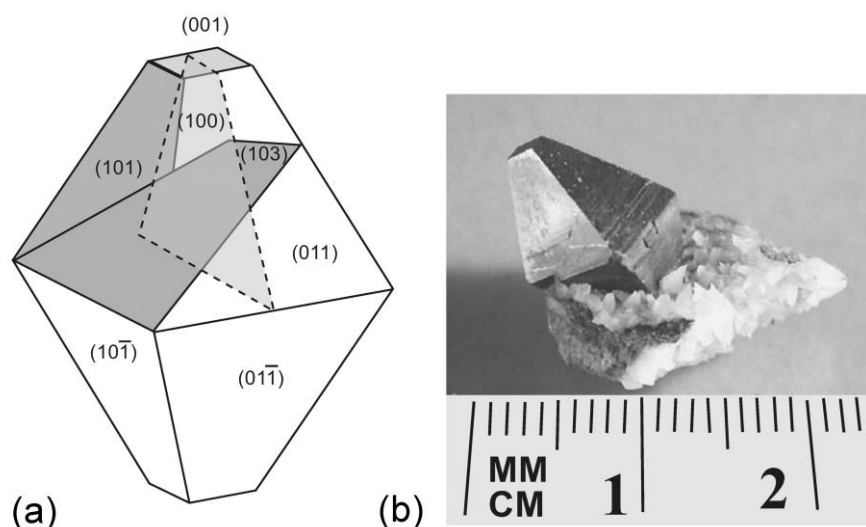
Figure 2.9. (a) Equilibrium shape of a TiO$_2$ crystal in the anatase phase, according to the Wulff construction and surface energies, and (b) Photograph of an anatase mineral crystal [53].

The surface structures of rutile TiO$_2$ (110), (100), and (001) single crystal faces are shown in Figure 2.10, 2.11 and 2.12, respectively. One-half of the Ti cations on a perfect (110) surface (Figure 2.10) are 6-fold coordinated (e.g. 7, 8, etc.), with the remaining one-half being 5-fold coordinated as in the bulk (e.g. 1, 2, etc.), the sixth bond being formed with electrolyte water species (OH$^-$ or H$_2$O). On the other hand, 2/3 of terminal oxygen anions (e.g., a, b, g, h, etc.) are 3-fold coordinated, with the remaining 1/3 being 2-fold coordinated bridging oxygen anions (e.g., k, l, etc). Unlike the (110) surface, the (100) surface (Figure 2.11) is entirely formed of 5-fold coordinated surface Ti cations (e.g., 1, 2, 5, 6, etc.), and 2-fold coordinated oxygen anions (e.g., a, b, m, n, etc.), while the (001) surface (Figure 2.12) has a lower coordination of Ti cations, which are only 4-fold coordinated (e.g., 3, 7, etc.), and 2-fold coordinated oxygen anions (e.g., a, g, etc.) [45, 54]. The electronic structures of the (110) and the (100) surfaces are similar in that the 5-fold coordinated Ti ions on both surfaces have the same O ligand environment. Furthermore, bridging site oxygen atoms, which are higher in position and

energetically more reactive than their surrounding atoms, exist on both of these planes. The slight difference between them is that the oxygen anions on the (100) surface are rotated by 45° relative to those on the (110) surface, and thus the perfect (100) surface is more active to dissociative water adsorption than an ideal (110) surface [55]. On the other hand, the (001) surface differs from the (110) and (100) surfaces in that all the surface Ti cations are 4-fold coordinated with two oxygen atoms within the surface plane and the other two in the plane below.
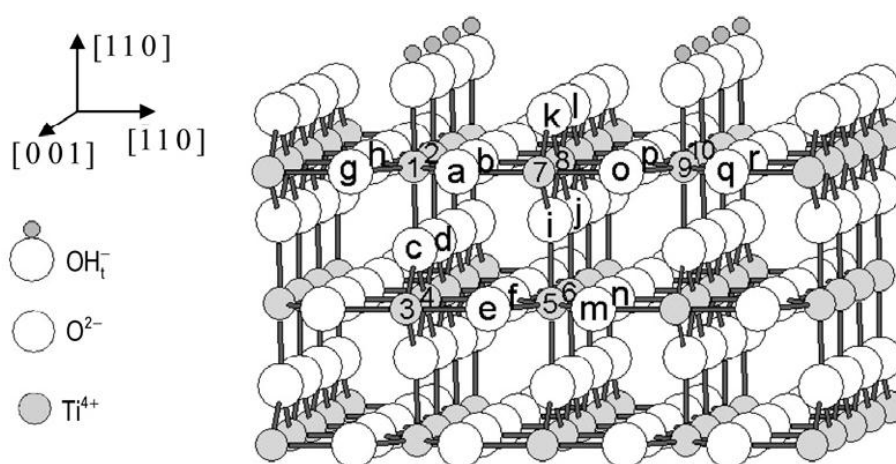

Figure 2.10. Ideal atomic arrangement of the TiO_2 rutile crystal structure with (110) top face. Titanium cations are identified with numbers and oxygen anions with letters [26].
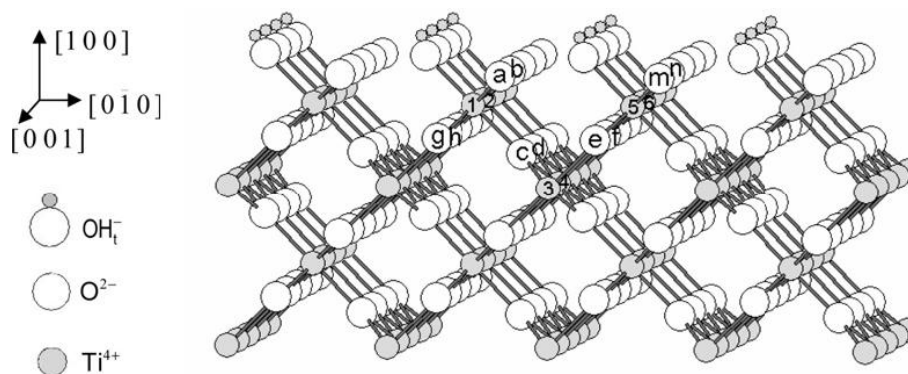

Figure 2.11. Ideal TiO_2 rutile crystal structure with (100) top face. Titanium cations are identified with numbers and oxygen anions with letters [26].
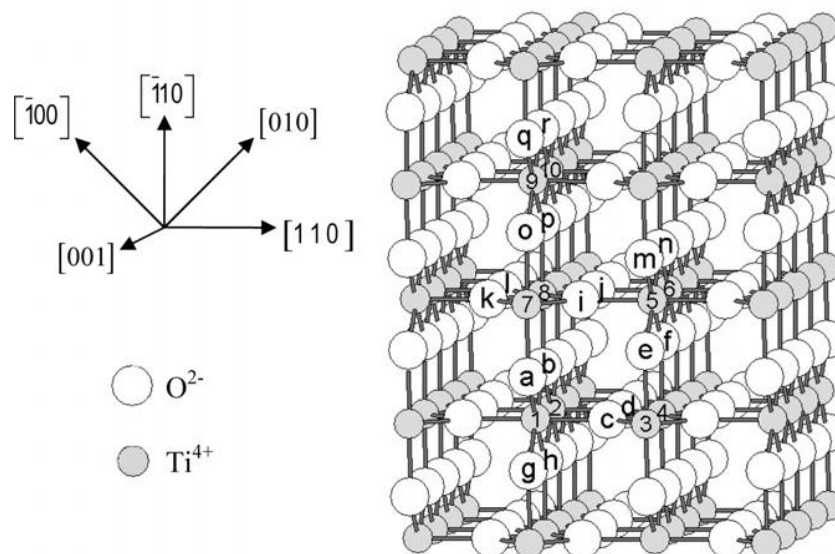
Figure 2.12. Ideal atomic arrangement of the TiO_2 rutile crystal structure with (001) front face. Titanium cations are identified with numbers and oxygen anions with letters [26].

The surface structure of anatase TiO_2 (101) is shown in Figure 2.13. It has 5-fold coordinated Ti cations and 2-fold coordinated O anions with a surface concentration of 5.16 x 10^{14} sites cm^{-2} for each species. Both 6-fold coordinated Ti cations and 3-fold coordinated O anions make up the remainder of the sites at the surface. The anatase TiO_2 surface has a saw tooth profile in which the 2-fold coordinated O anions are bound to the 5-fold coordinated Ti cations. Removal of one 2-fold coordinated bridging oxygen results in two 4-fold coordinated Ti^{3+} cations [56, 57]. These highly under-coordinated Ti cations are likely to be unstable.
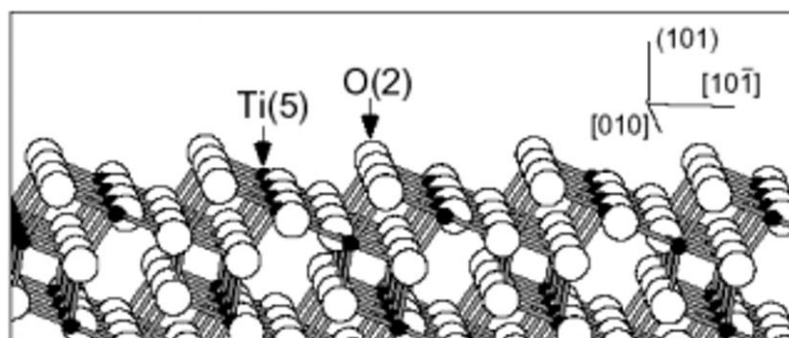

Figure 2.13. Schematic representation of the anatase (101) surface. The large open circles represent oxygen anions, and the small filled circles represent titanium cations [56].

2.3.3. Photocatalytic and Photoelectrochemical Water and Methanol Oxidation Mechanisms

Following the early work by Fujishima and Honda [1] reporting the photolysis of water on TiO_2 electrodes employing an external bias potential, and the suggestion that surface defect states may play a role in the decomposition of water into H_2 and O_2, many research efforts have been devoted to the understanding of the fundamental processes in TiO_2 photocatalysis and photoelectrochemistry [21, 22, 24, 26, 58]. It is generally accepted that, when TiO_2 is exposed to light of energy higher than the band gap, electrons are excited from the valence band into the conduction band. The holes generated in the valence band can be used for the photooxidation of organic compounds, either directly or indirectly via $OH^{\bullet}_s$ radical formation from adsorbed OH^- or water molecules, while the photogenerated electrons must be removed from the TiO_2 surface by transfer to a suitable electron acceptor, usually molecular oxygen in case of TiO_2 suspensions or Pt electrodes in case of photoelectrochemical cells, as shown in Figure 2.14 a and b, respectively. In principle, the photocatalytic reactions at a semiconductor surface can be regarded as irreversible photoelectrochemical reactions. In fact, the use of photoelectrochemical cells has been proposed as an alternative for the decomposition of pollutants in recent years [59-61]. Compared to reactors containing only the photocatalyst and the solution to be cleaned, one advantage of such a setup is that the photogenerated electrons can be removed from the photocatalyst surface through an external electrical circuit. Furthermore, the hole concentration at the surface of the photocatalyst can be turned by applying different potentials to the electrode *vs.* a reference electrode with stable potential.
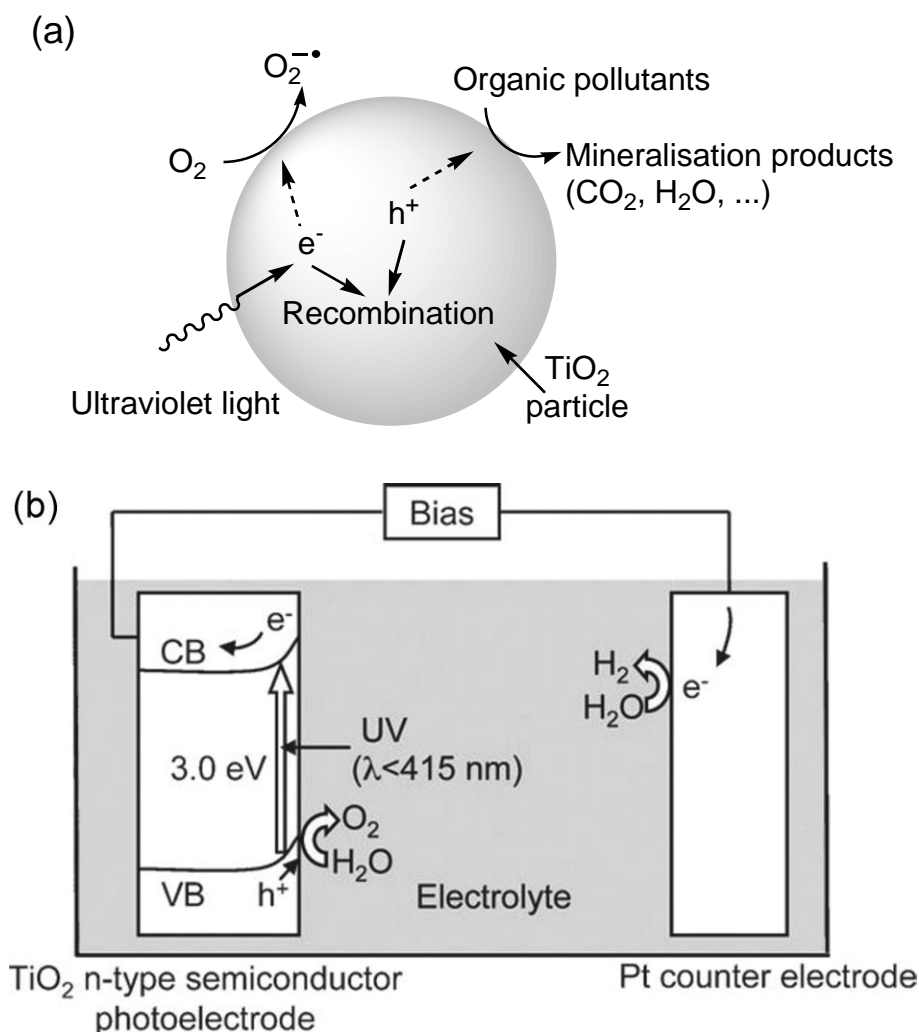
(a)

(b)

Figure 2.14. (a) Processes involved in the photocatalytic degradation of organic pollutants on TiO_2 particles, and (b) Photoelectrochemical water oxidation on a rutile TiO_2 photoelectrode.

As mentioned in the previous section, TiO_2 exhibits different ionic surface states associated with the unsaturated titanium and oxygen terminal ions. These ionic surface states are able to electronically interact with electrolyte species (water molecules, hydroxyl ions, protons and dissolved pollutants) as shown schematically in Figure 2.15. On the one hand, 3d orbitals of 5-fold coordinated terminal titanium cations (Ti_t) behave like Lewis acid sites able to form strong bonds with electron pairs of water species; on the other hand, 2p orbitals of 2-fold coordinated terminal oxygen ions, known as bridging oxygen $>O^{2-}_{br}$ species, behave like Lewis base sites able to share a pair of

valence band electrons with otherwise empty 1s orbitals of H^+ cations of the aqueous electrolyte [62]. Therefore, in contact with water vapor, if H_2O dissociative adsorption is assumed, two types of hydroxyl groups appear at the TiO_2 surface: (a) adsorbed hydroxyl groups 1-fold coordinated to terminal titanium atoms ($-OH^-_t$), (b) terminal hydroxyl ions resulting from the protonation of terminal 2-fold coordinated bridging oxygen ions ($>OH^-_{br}$) [62, 63]. Since the uptake of OH^- and H^+ ions is assumed to take place in equal amount, electric charge neutrality at the semiconductor surface is preserved. This situation changes when TiO_2 comes in contact with an aqueous electrolyte, either acidic or basic. If the electrolyte is sufficiently strongly acidic, most adsorbed hydroxyl groups become protonated, the formal charge of the TiO_2 surface becoming more positive. In contrast, in contact with a strong sufficiently alkaline electrolyte, bridging hydroxyl ions become deprotonated, the formal charge of the TiO_2 becoming more negative. It must be pointed out that oxygen atoms of $-OH^-_t$ groups behave like Brönsted base sites, while $>OH^-_{br}$ ions behave like Brönsted acid sites.
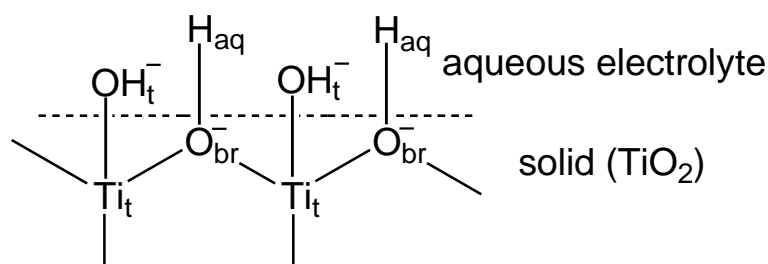

Figure 2.15. Two types of surface hydroxyl groups resulting from the dissociative adsorption of water (vapor phase) on TiO_2 rutile [26].

It is generally accepted that water species adsorbed on 5-fold coordinated terminal Ti atoms are efficient traps for photogenerated free valance band holes (h^+_{VB}) at the TiO_2 surface and, therefore, the main source of surface $OH^\bullet_s$ radicals active in photocatalytic reactions. However, based on the

interpretation of ultraviolet photoelectron spectroscopy (UPS) and metastable impact electron spectroscopy (MIES) of well defined, hydrated TiO_2 surfaces, obtained by Kurtz et al. [64] and Krischok et al. [65], respectively, evidence has been provided that the photooxidation of adsorbed water species on TiO_2 is not only kinetically but also thermodynamically hindered [62]. At the bulk of stoichiometric TiO_2, titanium and oxygen atoms are 6-fold and 3-fold coordinated, respectively. In contrast, at the TiO_2 surface, no matter whether the anatase or the rutile crystal face are considered, terminal Ti atoms are 5-fold coordinated, while a large part of terminal oxygen atoms (bridging oxygen ions) are 2-fold coordinated. Due to the partial ionic character of Ti–O bonds a decrease in the electrostatic interaction of terminal oxygen ions with Ti atoms, and therefore a shift towards higher energies of their corresponding O:2p energy levels, is to be expected when coordination diminishes from 3-fold to 2-fold. The same conclusion is reached if the Ti–O bond is considered to be partially covalent, as in this case a higher Ti–O bond energy is to be expected for 3-fold than for 2-fold coordinated oxygen atoms, so that a higher energy stabilization should be expected for O:2p orbitals in the former case. Since the upper energy levels of 3-fold coordinated O:2p orbitals of oxygen ions constitute the VB edge at the bulk (E_{VB}), the energy levels of 2-fold coordinated terminal oxygen ions should be located in the bandgap. This means that after thermalization, when reaching the semiconductor surface, VB free holes must not be trapped at 3-fold but at 2-fold coordinated bridging oxygen ions ($>OH^-_{br}$), leading to the generation of one-fold coordinated bridging oxygen radicals $-OH^{\bullet}_{br}$ [62]. Because of the loss of one electron, the bond strength of ($-OH^{\bullet}_{br}$) oxygen radicals to terminal Ti ions is considerably weakened with respect to that of ($>OH^-_{br}$) bridging oxygen ions, making the former reactive towards the oxidation of organic molecules [62]. It is noteworthy that the bridging oxygen radicals ($-OH^{\bullet}_{br}$) do

not originate from the direct photooxidation of an adsorbed hydroxyl ion from the electrolyte, but just of a protonated terminal oxygen atom from the TiO_2. The involvement of these radicals in the water photooxidation mechanism explains the fact that some of the detected oxygen on TiO_2 electrodes is coming from the oxygen lattice of TiO_2 as detected in ref. [66].

Depending on the aforementioned information, the trapping of a photogenerated VB free hole by a 2-fold coordinated bridging hydroxyl ion will lead to Ti–O bond breaking and simultaneous photogeneration of a 1-fold coordinated bridging hydroxyl radical. Simultaneously, the coordination of the corresponding Ti atom decreases from 6-fold to 5-fold as shown in step (a) in Figure 2.16. In step (b) a new bridging hydroxyl radical at an adjacent site is photogenerated with the participation of a second hole, with the coordination of another Ti atom decreasing from 6-fold to 5-fold. As the coordination of adjacent bridging hydroxyl radicals is not 2-fold but 1-fold, they can approach each other at a short distance (lower than 2.5 Å), which renders the $O_{br}=O_{br}$ bond formation possibility [67], so that a $HO_{br}=O_{br}H$ hydrogen peroxide molecule attached to two adjacent Ti atoms is generated (step c); and a bridging hydroxyl vacancy is simultaneously generated. Further photooxidation in step (d) of the adsorbed hydrogen peroxide molecule generated in (c) leads to the evolution of an oxygen molecule and the simultaneous generation of a second bridging hydroxyl vacancy. Finally, in step (e), two water molecules are dissociatively adsorbed at adjacent bridging hydroxyl vacancies generated in steps (c) and (d) and two bridging hydroxyl ions with their respective oxygen atoms belonging to electrolyte water molecules are regenerated.
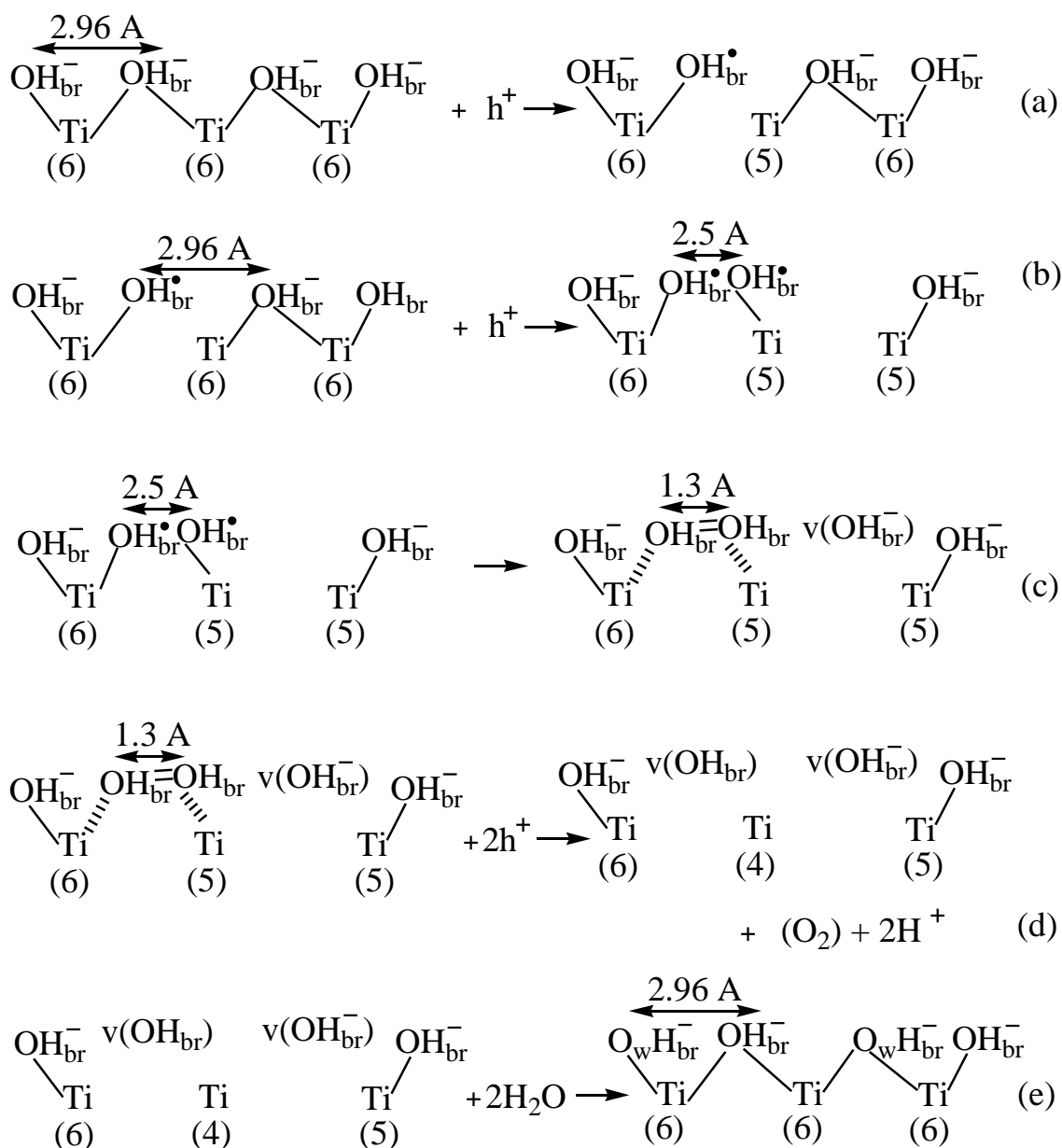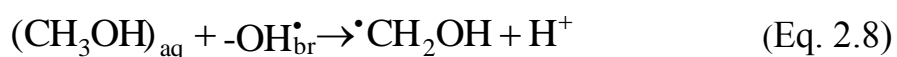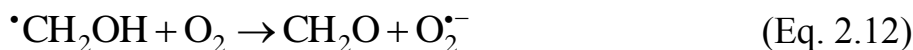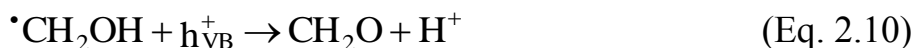
Figure 2.16. Sequence of reaction steps involved in the redox photooxidation mechanism of water on TiO_2. Sub-indices indicate the coordination numbers of the Ti atoms [26].

In the presence of organic molecules in aqueous solution, e.g. methanol, the photocatalytic steps can be described as follows: Upon UV illumination, free holes (h_{VB}^+) are generated at any energy level within the VB, depending on the energy of the incident UV photons. After thermalization, holes reach the TiO_2 surface and are trapped at band gap surface states. These may be intrinsic, associated with the terminal oxygen ions ($>OH_{br}^-$) as mentioned

above (Eq.2.7), or extrinsic, associated with either chemisorbed methanol molecules or water species adsorbed at terminal Ti atoms. Since the filled VB energy levels of adsorbed water species are below the VB edge of TiO_2, their photooxidation with photogenerated free holes to produce adsorbed $OH^{\bullet}$ radicals is thermodynamically hindered and has been excluded as described above [26, 62]. Therefore, the photooxidation of non-adsorbed methanol, $(CH_3OH)_{aq}$, can exclusively take place via adiabatic hole transfer from photogenerated surface radicals $(-OH^{\bullet}_{br})$ (Eq. 2.8), while adsorbed methanol, $(CH_3OH)_{ads}$, might be photooxidized via direct, inelastic hole transfer of photogenerated free holes (Eq. 2.9) [68, 69]. Both reactions lead to the formation of $^{\bullet}CH_2OH$ radicals by hydrogen abstraction. In the absence of O_2, further oxidation of the $^{\bullet}CH_2OH$ radical can occur by capture of another photogenerated hole or electron injection from the radical into the conduction band of TiO_2 (Eq. 2.10 and 11). The latter process is referred to as "photocurrent-doubling" and has been observed in many related systems including the photoanodic oxidation of alcohols on TiO_2 electrodes [70-72]. However, it was previously noted that the amount of the current doubling for methanol never reaches the same extent as the hole current and that the extent of the photocurrent doubling depends on many factors such as the degree of TiO_2 crystal doping, the methanol concentration, the acidity of the solvent and the light intensity [70, 73, 74]. For example, low values of the TiO_2 doping level and the solvent acidity were found to lead to a lower extent of the photocurrent doubling [73]. In presence of O_2, the $^{\bullet}CH_2OH$ radical and the photogenerated CB electrons react with dissolved oxygen molecules according to Eq. 2.12 and 13.

$$> OH^{-}_{br} + h^{+}_{VB} \rightarrow -OH^{\bullet}_{br} \qquad\qquad\qquad (Eq.\ 2.7)$$

$$(CH_3OH)_{aq} + -OH^{\bullet}_{br} \rightarrow {}^{\bullet}CH_2OH + H^{+} \qquad\qquad (Eq.\ 2.8)$$

$$(CH_3OH)_{ads} + h^+_{VB} \rightarrow \, ^{\bullet}CH_2OH + H^+ \qquad \text{(Eq. 2.9)}$$

$$^{\bullet}CH_2OH + h^+_{VB} \rightarrow CH_2O + H^+ \qquad \text{(Eq. 2.10)}$$

$$^{\bullet}CH_2OH + TiO_2 \rightarrow CH_2O + H^+ + e^-_{CB} \qquad \text{(Eq. 2.11)}$$

$$^{\bullet}CH_2OH + O_2 \rightarrow CH_2O + O^{\bullet -}_2 \qquad \text{(Eq. 2.12)}$$

$$O_2 + e^-_{CB} \rightarrow O^{\bullet -}_2 \qquad \text{(Eq. 2.13)}$$

It was believed that hydroxyl radical species are responsible for methanol oxidation. For instance, methanol has been employed as $OH^{\bullet}_s$ radical scavenger in order to determine the quantum yield and photonic efficiency of $OH^{\bullet}_s$ radical generation from the photogenerated holes at the TiO_2 surface [75-77]. However, in some studies, direct transfer of photogenerated holes have been proposed. For example, an electron paramagnetic resonance (EPR) study reported by Micici et al. [78, 79] on illuminated colloidal TiO_2 indicates that the transfer of trapped holes from lattice oxygen to methanol molecules occurs, leading to the formation of $^{\bullet}CH_2OH$ radical. The authors have not seen the EPR signal assigned to $OH^{\bullet}_s$ radials. However, the study has been performed at low temperature (1.9 K). In a more recent study Wang et al.[80] have reported that the photooxidation of methanol in water depends on the molecular species adsorbed on the TiO_2 surface, which itself depends on the concentration of methanol. They studied the competitive adsorption process between water and methanol on TiO_2 through the *in situ* use of sum frequency generation (SFG), a nonlinear spectroscopic technique. These authors concluded that the indirect oxidation by $OH^{\bullet}_s$ radicals is the dominant mechanism when water is the dominant species at the TiO_2 surface; the critical molar ratio between water and methanol being about 300, which corresponds to a methanol concentration of 0.47 vol%. For higher methanol concentrations, direct oxidation of methanol by photogenerated holes occurs at the TiO_2 surface.

In general, it remains unclear whether photooxidation of solution species proceeds via direct interfacial transfer of holes [81, 82] or involves the reaction with photogenerated hydroxyl radicals as intermediate step [83, 84]. Thus, in the present thesis, the intensity modulated photocurrent spectroscopy (IMPS) technique will be used in order to understand the mechanisms of water and methanol oxidation at the TiO_2 surface and to understand the behavior of the surface intermediates involved in the photocatalytic and photoelectrochemical processes.

2.4. Intensity Modulated Photocurrent Spectroscopy (IMPS)

2.4.1. Explanation of the IMPS Method

Intensity modulated photocurrent spectroscopy (IMPS) is a method using sinusoidal modulation of the light intensity that can be used to investigate the kinetics of photoelectrochemical reactions at semiconductor electrodes [21, 43, 85-92], i.e., the rate constants of charge transfer and recombination occurring at a semiconductor/electrolyte interfaces can be determined [93-96].

In the IMPS measurements, the working electrode is illuminated by a modulated light source, which can be a light emitting diode (LED) or a laser beam modulated by an acousto-optic device. The amplitude of the illumination function is chosen not to exceed ca. ±10 % to ensure that the system remains near a steady state during the measurement. The phase shift φ of the resulting photocurrent with respect to the light modulation and its amplitude A are measured for different modulation frequencies f. Similar to impedance measurements, the results are usually presented in Bode plots (φ and A vs. f) or, more commonly, in complex plane plots, where a semicircle appears in the positive/positive quadrant as schematically shown in Figure 2.17.b [21, 43]. The modulated illumination leads to a modulated flow of photogenerated minority carriers (holes in this case), the so-called Gärtner

flux g_1 (see section 2.2.2), towards the surface, where they can undergo charge transfer to the electrolyte either directly or through interfacial steps (rate constant k_{tr}) or recombination with electrons (rate constant k_{rec}) as illustrated in Figure 2.17.a.
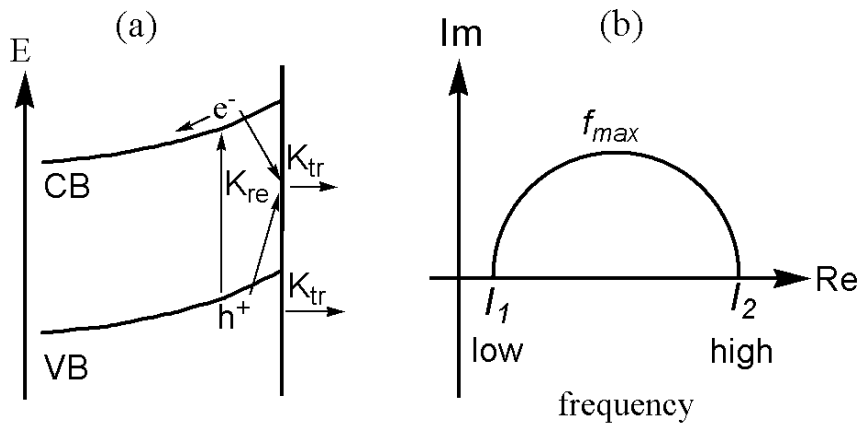

Figure 2.17. (a) Illustration of processes involving photogenerated holes at the electrode surface (b) Scheme of an IMPS complex plain plot.

If surface recombination occurs at an illuminated semiconductor electrode, the response to intensity modulated illumination will be made up of two components, the first being associated with the photogenerated minority carriers and the second with the majority carriers that must flow to the surface in order to take part in surface recombination. The two currents have opposite signs, and generally they will not be in phase. As a consequence, both the phase and magnitude of the net photocurrent will vary with frequency in a way that is related to the kinetics of recombination. A generalized frequency dependent IMPS response can be expressed in terms of the rate constants associate with the recombination and charge transfer by the following equation [74]:

$$j(\omega)/g_1 = \frac{k_{tr} + i\omega\dfrac{C}{C_{SC}}}{k_{tr} + k_{rec} + i\omega}\left(\frac{1}{1 + i\omega RC}\right) \qquad \text{(Eq. 2.14)}$$

where

$$C = \frac{C_{SC} C_H}{C_{SC} + C_H} \qquad\qquad\qquad\qquad \text{(Eq. 2.15)}$$

RC is the time constant of the electrochemical cell, where R is the total series resistance arising from the electrolyte, the semiconductor bulk and the ohmic contact and C is the effective capacitance. C_{sc} and C_H represent the space charge and Helmholtz capacitances, respectively. Eq. 2.14 predicts a semicircle in the upper complex plane quadrant related to the photogeneration of charge carriers and their charge transfer and recombination at the electrode surface and the second term (in brackets) describes the photocurrent attenuation due to the RC constant at high frequencies. Figure 2.18.a and b show the two semicircles in the complex plot of Im($j(\omega)$) vs. Re($j(\omega)$) as a function of frequency ω calculated from Eq. 2.14 at complete and partial recombination, respectively.
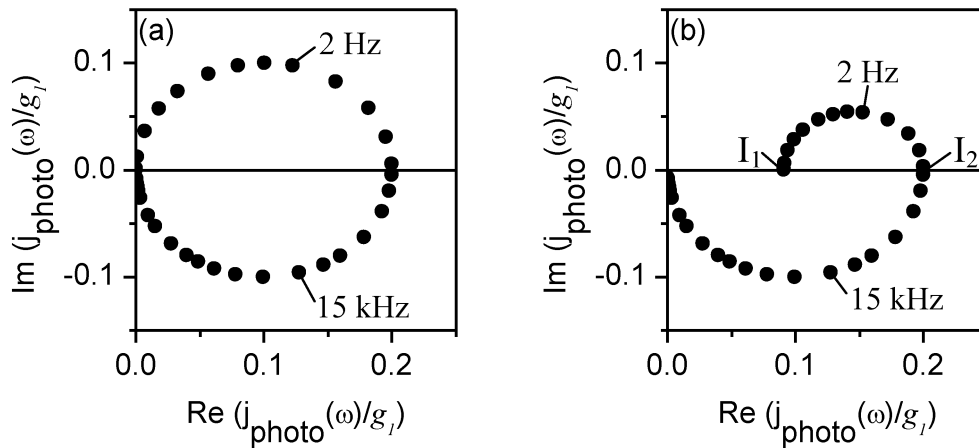
Figure 2.18. Theoretical IMPS plots calculated from Eq. 2.14 with $k_{rec}=10$ s^{-1}, $C_{sc}=4\times10^{-6}$ F cm^{-2}, $C_H=10^{-5}$ F cm^{-2}, R=10 Ω, and (a) $k_{tr}=0$ s^{-1} (complete recombination), (b) $k_{tr}=1$ s^{-1} (partial recombination).

In the low frequency limit, the plot tends towards the real axis at the point $I_1 = j(\omega)_{\omega\to 0} = g_1 k_{tr}/(k_{tr}+k_{rec})$. The low frequency limit I_1 represents the differential steady-state photocurrent increase due to a differential increase in

the light intensity [43]. I_1 should therefore be zero if no electroactive substance is present in the electrolyte as shown in Figure 2.18.a. In this case, only recombination takes place at the electrode surface ($k_{tr} = 0$), giving rise to a recombination current of electrons towards the surface. This is also the explanation for the positive phase shift obtained in IMPS measurements, since a negative recombination current lagging behind the illumination appears like a positive current preceding the illumination. As the frequency increases, the relaxation in the concentration of photogenerated holes at the semiconductor surface is characterized by f_{max}, which is the frequency at the maximum of the semicircle (Eq. 2.16) [96]:

$$2\pi f_{max} = k_{tr} + k_{rec} \qquad\qquad \text{(Eq. 2.16)}$$

Then, the imaginary component of the photocurrent decreases to intersect the real axis at $I_2 = g_1 C_H/(C_{sc} + C_H)$). The high frequency intercept I_2 represents the amplitude of the Gärtner flux g_1 [97] provided that $C_{sc} << C_H$. The absolute values of the phenomenological k_{tr} and k_{rec}, respectively, can be derived, thus, from the intersections of the semicircle with the real axis, I_1 and I_2, respectively. The relationship between I_1, I_2 and the rate constants is therefore

$$\frac{I_1}{I_2} = \frac{k_{tr}}{k_{tr} + k_{rec}} \qquad\qquad \text{(Eq. 2.17)}$$

At the I_2 point in the IMPS plot the frequency is large in comparison with ($k_{tr} + k_{rec}$) but still low in comparison with RC^{-1}. At higher frequencies, the IMPS plot exhibits a second semicircle in the lower quadrant arising from the RC time constant of the cell, and the response tends towards the origin on the complex plane plot as the photocurrent becomes completely attenuated as shown in Figure 2.18. For highly doped semiconductors such as TiO_2, the assumption that $C_{sc} << C_H$ is not valid and hence k_{tr} and k_{rec} cannot be readily calculated from the IMPS response according to Eq. 2.16 and 17 due to the

high *RC* attenuation. In this thesis, the phenomenological k_{tr} and k_{rec} values have been calculated by fitting the IMPS response according to Eq. 2.14.

However, the discussed model only describes the single electron transfer process. It was proven that regardless of the mechanism of the photoelectrochemical process, a semicircular IMPS response can always be described in terms of the two phenomenological rate parameters k_{tr} and k_{rec}. In the simplest case of one-electron charge transfer processes, the phenomenological rate parameters are identical with the true charge transfer and rate recombination constants. In the case of multistep charge transfer mechanisms, the same expressions can be used to analyse the experimental IMPS response, but the k_{tr} and k_{rec} values obtained from the experimental data are in this case phenomenological rate parameters, which are functions of but not identical with the rate constants associated with the elementary steps as will be discussed in the following section.

2.4.2. Multistep Electron Transfer Model

The nature of the surface intermediates generated at TiO_2 upon illumination can be defined by analysis of the IMPS responses as proven by Peter et al. [98]. A model describing the multi-electron transfer reactions has been developed by assuming that charged surface-bound intermediates X^+ are generated by hole capture at the interface as "surface-trapped holes" and removed either by capture of a second hole (Case I) or by reaction of two mobile X^+ species (Case II). Surface electron-hole recombination is assumed to involve trapping of conduction band electrons by the intermediate X^+ species. In the presence of a redox couple in solution, X^+ may react with either the reduced or the oxidized components, but these possibilities have been omitted to simplify the analysis. The mechanism can therefore be represented by the reactions

$$A + h^+ \xrightarrow{\ k_1\ } X^+ \qquad\qquad\qquad\qquad \text{(Eq. 2.18.a)}$$

$$X^+ + h^+ \xrightarrow{\ k_2\ } B^{2+} \qquad\qquad \text{(Case I)} \qquad \text{(Eq. 2.18.b)}$$

$$X^+ + e^- \xrightarrow{\ k_3\ } A \qquad\qquad\qquad\qquad \text{(Eq. 2.18.c)}$$

$$X^+ + X^+ \xrightarrow{\ k_4\ } A + B^{2+} \qquad \text{(Case II)} \qquad \text{(Eq. 2.18.d)}$$

where A is a hole trapping site in the semiconductor crystal lattice, B^{2+} is the final product and X^+ is the (surface mobile) intermediate. For simplicity, the surface concentration of X^+ has been assumed to remain small relative to that of A, in order to treat k_1/s^{-1} as a pseudo first-order rate constant.

The pseudo first-order rate constant k_3 for the recombination step involving electron capture by the intermediate X^+ depends on the surface electron concentration n_s and therefore on the potential drop $\Delta\phi_{sc}$ in the space charge layer of the semiconductor:

$$k_3 = k_3^0 \exp\left(\frac{-\beta q \Delta\phi_{SC}}{k_B T}\right) \qquad\qquad \text{(Eq. 2.19)}$$

where k_3^0 is the value of k_3 at the flatband potential when $n_s = n_{bulk}$ and β is an empirical factor associated with Fermi-Level pinning. Peter et al. [98] have assumed in the derivation of expressions for the IMPS response that n_s is constant under potentiostatic conditions, but this assumption becomes invalid if the band bending is changed by the accumulation of photogenerated holes or charged surface-bound intermediates. This situation is considered in the following.

The differential equations describing the time dependence of the surface concentrations of holes (p_s) and intermediate species (X_s) are

$$\frac{dp_s}{dt} = g - k_1 p_s - k_2 p_s X_s \qquad\qquad \text{(Eq. 2.20)}$$

$$\frac{dX_s}{dt} = k_1 p_s - k_2 p_s X_s - k_3 X_s - 2k_4 X_s^2 \qquad \text{(Eq. 2.21)}$$

For simplicity in the case that αL_p in Eq. 2.6 (see section 2.2.2) is large and/or $W >> 1/\alpha$, it can be assumed that g_1 is independent of potential and equal to the incident photon flux.

The steady state solution

The steady state solution of Eq. 2.20 and 21 gives a cubic equation in X. For simplicity Peter et al. have considered two limiting cases. If the mobility of surface-bound intermediates is vanishingly small ($k_4 \rightarrow 0$), the reaction in Eq. 2.18.d can be omitted (Case I). Conversely, if the coverage of X^+ becomes high and X^+ is mobile, the reaction in Eq. 2.18.d can become the dominant route for decay of the intermediate, and the reaction in Eq. 2.18.b can be omitted (Case II).

Case I (X^+ not mobile):

Solution of Eq. 2.20 and 21 gives the steady state concentration of X^+ and p:

$$X_0 = \frac{k_1 p_0}{k_2 p_0 + k_3} \qquad \text{(Eq. 2.22)}$$

$$p_0 = \frac{g}{k_1 + k_2 X_0} \qquad \text{(Eq. 2.23)}$$

It follows that X_0 is given by

$$X_0 = \frac{-b + \sqrt{(b^2 - 4ac)}}{2a} \qquad \text{(Eq. 2.24)}$$

where

$$a = k_2 k_3$$

$$b = (k_1 k_3 + k_2 g)$$

$$c = -k_1 g$$

It is evident from Eq. 2.22 that in the limit $k_3 \rightarrow 0$ (no recombination), X_0 saturates at a value determined by the ratio k_1/k_2.

The steady state photocurrent is obtained by noting that

$$j_{photo} = g - j_{rec} = g - k_3 X_0 \qquad \text{(Eq. 2.25)}$$

It follows that the steady state quantum efficiency Φ_0 is given by

$$\Phi_0 = \frac{j_{photo}}{g} = 1 - \frac{k_3 X_0}{g} \qquad \text{(Eq. 2.26)}$$

The IMPS response is first considered for Case I (no $X^+ + X^+$ reaction).

The total time-dependent flux of holes is

$$g = g_0 + |g_1| \exp(i\omega t) \qquad \text{(Eq. 2.27)}$$

where $g = |g_1| \exp(i\omega t)$ is the periodic component of the hole flux arising from the intensity modulation. Eq. 2.26 can be rewritten to describe the periodic component of the photocurrent in the form

$$\frac{j(\omega)}{g_1} = 1 - \frac{k_3 X_1}{g_1} \qquad \text{(Eq. 2.28)}$$

where X_1 corresponds to the frequency-dependent periodic component of the surface concentration of the X^+ species.

The total concentrations of intermediates and holes can be written by analogy with Eq. 2.27 as

$$X = X_0 + X_1 \exp(i\omega t) \qquad \text{(Eq. 2.29)}$$

$$p = p_0 + p_1 \exp(i\omega t) \qquad \text{(Eq. 2.30)}$$

It follows that

$$p_1(k_1 + k_2 X_0 + i\omega) = g_1 - k_2 p_0 X_1 \qquad \text{(Eq. 2.31)}$$

$$X_1(k_2 p_0 + k_3 + i\omega) = (k_1 - k_2 X_0) p_1 \qquad \text{(Eq. 2.32)}$$

The frequency-dependent conversion efficiency, $\Phi(\omega)$, can now be derived for Case I. It is

$$\Phi(\omega) = \frac{j(\omega)}{g_1} = \frac{2(k_1 k_2 p_0 + k_2 k_3 X_0) - \omega^2 + i\omega[k_1 + k_2(p_0 + X_0) + k_3]}{2k_1 k_2 p_0 + k_1 k_3 + k_2 k_3 X_0 - \omega^2 + i\omega[k_1 + k_2(p_0 + X_0) + k_3]}$$

(Eq. 2.33)

where X_0 and p_0 are the steady state surface densities of intermediates and of holes, which are given by Eq. 2.22 and 23, respectively.

The complex plane plot of Eq. 2.33 is not always a semicircle since it contains quadratic terms. However, for physically plausible values for the rate constants and modulation depths of ca. 10%, ω^2 can be neglected. Eq. 2.33 then simplifies to

$$\Phi(\omega) = \frac{k_{tr} + i\omega}{k_{tr} + k_{rec} + i\omega}$$

(Eq. 2.34)

where the phenomenological rate constants for Case I are defined as

$$k_{tr}^I = \frac{2k_2(k_1 p_0 + k_3 X_0)}{k_1 + k_2(p_0 + X_0) + k_3}$$

(Eq. 2.35)

$$k_{rec}^I = \frac{k_3(k_1 - k_2 X_0)}{k_1 + k_2(p_0 + X_0) + k_3}$$

(Eq. 2.36)

Eq. 2.35 is formally identical to the expression derived for the IMPS response for a single-step electron transfer reaction (Eq. 2.14) using the phenomenological recombination k_{rec} and charge transfer k_{tr} parameters [99]. The link between phenomenological parameters and real rate constants for Case I is given by Eq. 2.35 and 36.

Analysis of the IMPS responses in terms of the phenomenological rate constants yields the values of k_{rec}^I and k_{tr}^I shown in Figure 2.19. In the case of

a simple one electron process with negligible surface charging, a plot of log k_{rec} vs. potential is expected to have a slope of $(59 \text{ mV})^{-1}$, but the calculation for Case I shows that the plot tends to be steeper. A small but measurable decrease of k^I_{tr} with increasing band bending is expected. This arises from the inclusion of the k_3 term in Eq. 2.22.
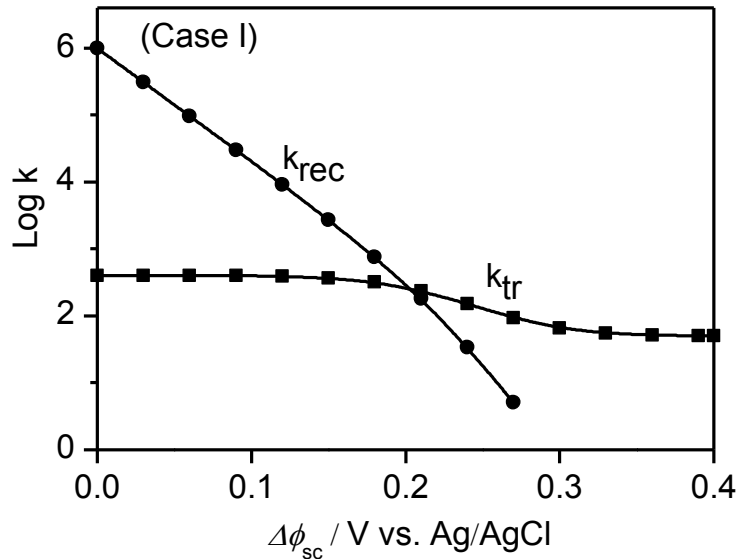
Figure 2.19. Phenomenological rate constants as a function of the band bending for Case I. $k_1 = 10^{-10} \text{ s}^{-1}$, $k_2 = 10^{-3} \text{ cm}^2 \text{ s}^{-1}$, $k_3^0 = 10^5 \text{ s}^{-1}$, $k_4 = 10^{10} \text{ cm}^2 \text{ s}^{-1}$, $g_I = 10^{14} \text{ cm}^{-2} \text{ s}^{-1}$ and $\beta = 1$. These values have been extracted from ref. [98].

Case II (X⁺ mobile):

If the hole capture cross-section of X^+ is small and the surface-bound species are mobile, the decay of X^+ may take place predominantly via the reaction given in Eq. 2.18.d. In this case, the steady state solutions for the concentrations of holes and X^+ are

$$p_0 = \frac{g}{k_1} \qquad \text{(Eq. 2.37)}$$

$$X_0 = \frac{-k_3 + \sqrt{(k_3^2 + 16k_4 g_0)}}{8k_4} \qquad \text{(Eq. 2.38)}$$

If the $X^+ + X^+$ reaction predominates, a similar treatment yields an expression identical to Eq. 2.34 but the phenomenological parameters have a different dependence on the real rate constants. In this case, the phenomenological charge transfer k_{tr}^{II} and recombination k_{rec}^{II} rate constants are given by

$$k_{tr}^{II} = \frac{4k_1 k_4 X_0}{k_1 + 4k_4 X_0 + k_3}$$
(Eq. 2.39)

$$k_{rec}^{II} = \frac{k_1 k_3}{k_1 + 4k_4 X_0 + k_3}$$
(Eq. 2.40)

Figure 2.20 shows that this deviation is a consequence of the fact that k_{tr}^{II} increases with band bending as X^+ accumulates, increasing the rate of the second-order $X^+ + X^+$ process. k_{tr}^{II} reaches a plateau when the surface concentration of the intermediate saturates at a value determined by the light intensity.
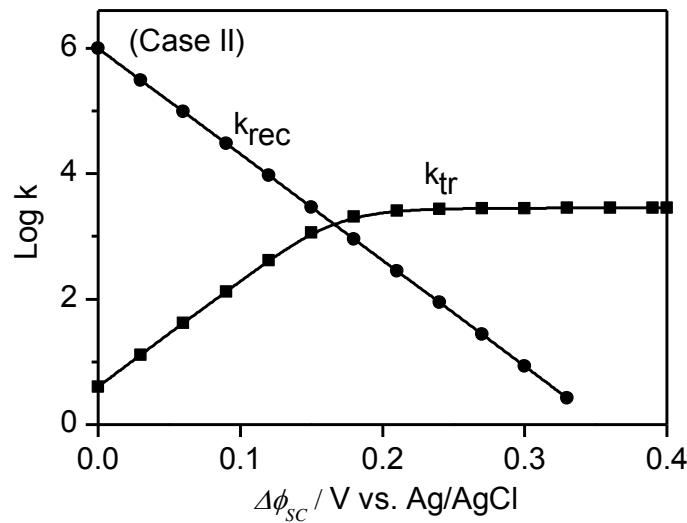
Figure 2.20. Phenomenological rate constants as a function of the band bending for Case II. $k_1=10^{-10}$ s^{-1}, $k_2=10^{-3}$ cm^2 s^{-1}, $k_3^0=10^5$ s^{-1}, $k_4=10^{10}$ cm^2 s^{-1}, $g_I= 10^{14}$ cm^{-2} s^{-1} and $\beta=1$. These values have been extracted from ref.[98].

3. Experimental

3.1. Preparation of TiO$_2$ Electrodes

3.1.1. TiO$_2$ Single Crystal Electrodes

Single crystal rutile TiO$_2$ wafers with a size of 10 x 10 x 0.5 mm^3 exhibiting polished (100), (001) or (110) surfaces on one side were purchased from K&R creation Co., Japan and cut into pieces of 5 x 5 x 0.5 mm^3. To achieve n-type doping by oxygen vacancies, the wafers were exposed to a stream of hydrogen gas at 600°C for 2 h. Electrodes were fabricated by connecting copper wires to the surfaces opposite to the polished surfaces of these wafers using conductive epoxy resin. The copper wires were covered with glass tubes, and the connections between the glass tubes and the wafers except the polished surfaces were sealed with non-conductive epoxy resin (Araldite Rapid, Ciby Geigy).

Prior to the electrochemical measurements a part of the electrode surfaces has been photoetched to remove the thin inactive surface layer formed during the H$_2$ treatment. Photoetching was carried out in 0.05 M H$_2$SO$_4$ using a three-electrode photoelectrochemical cell with a Pt counter electrode and an Ag/AgCl/NaCl(sat) reference electrode as previously reported by Imanishi et al. [100, 101]. The electrode potential was kept at +2.5 V during UV illumination with a 250 W Xe lamp for approximately 15 s, the incident light intensity at the electrode surface being 5 mW cm^{-2}.

The anatase TiO$_2$ single crystal (101) surface has been obtained from a natural mineral single crystal, which has been oriented, cleaved, and polished. The resulting surface was 3 x 3 x 0.5 mm^3 in size. It was initially clear with an orange shade, and turned grey after exposition to a stream of hydrogen gas at 600 °C for 2 h to achieve n-type doping by oxygen vacancies.

3.1.2. TiO$_2$ Thin-Film Electrodes

The TiO$_2$ thin-film was prepared on a cleaned conductive fluorine-tin oxide (FTO) glass substrate (cleaning sequence: distilled water, isopropanol, acetone and compressed air) by a dip-coating method. The dip coating solution was obtained by adding 23 ml of titanium isopropoxide (TISP) and 27 ml ethanol mixture to 100 ml ethanol containing 4.5 ml acetic acid to control the hydrolysis and condensation reactions. This solution was maintained for 1 h under stirring to obtain the complex chelate. Afterwards, 43 ml of ethanol mixed with 1.35 ml aqueous HCl solution (0.1M) was added dropwise to this solution to start hydrolysis and condensation reactions. The final molar ratio of the solution was 1 TISP : 1 acetic acid : 40 EtOH : 1 H$_2$O, with the oxide concentration being fixed to 30 g L^{-1}. The sol solution was aged for 1 day before dip-coating deposition [102]. In the dip-coating process, the FTO substrate slides were dipped into the dipping solution (dipping speed 10 mm s^{-1}) and withdrawn into open air (withdrawing speed 1 mm s^{-1}) after 5 s. The TiO$_2$ films were obtained by calcination of the dip-coated FTO substrate slides at 450 ^{0}C in air for 2 h at a heating rate of 2 ^{0}C min^{-1} and then naturally cooling down to room temperature.

The TiO$_2$ thin-film electrodes were prepared by cutting pieces of 1 x 1 cm^2 and connecting copper wires to the conductive FTO surfaces using conductive epoxy resin. The copper wires were covered with glass tubes, and the connections between the glass tubes and the FTO were sealed with non-conductive epoxy resin (Araldite Rapid, Ciby Geigy).

3.2. Characterization of TiO$_2$ Single Crystal Electrodes

3.2.1. X-ray Diffraction

X-ray diffraction (XRD) data for the TiO$_2$ surfaces have been recorded on a Bruker D8 diffractometer using a reflection geometry with variable divergence slits, Cu-Kα$_{1,2}$ radiation and a secondary monochromator. The scan method for single crystal faces was theta-theta scan (tube and detector scan locked-coupled). The data points were collected with step size of 0.03°, 1.5 seconds measurement time per step in the 2θ range from 20 to 60° and 2.5° soller slit on tube and detector sides. The scan method for thin-film was grazing incidence diffraction, 0.5° 2θ incidence angle (tube fixed, detector scan). The data points were collected with step size of 0.02°, 10 seconds measurement time per step in the 2θ range from 20 to 60°. Soller slit of 2.5° and 0.35° were used on tube and detector sides, respectively. Structural data for the known phases were taken from the PDF-2 database with PDF numbers: anatase [21-1272] and rutile [21-1276].

3.2.2. Scanning Electron Microscopy

Field-emission scanning electron microscopy (FE-SEM) measurements were carried out on a JEOL JSM-6700F field-emission instrument. The instrument functions by using electromagnets to raster a focused electron beam across the sample surface. The electrons emitted by the sample are collected by a secondary electron detector (SE) detector. A tungsten single crystal filament with an accelerating voltage of 2.0 kV was used as an electron source. In order to prevent distortions due to the accumulation of charge in the sample it is important that electrical contact is maintained between the sample surface and the sample holder. For that the TiO$_2$ single crystal surfaces was pressed into conductive carbon tape to achieve this

current leakage path and the instrument was operated under a low vacuum of $6.25\text{x}10^{-5}$ Pa. For the anatase thin-film deposited on FTO glass, conducting silver paint was used to establish contact between the FTO substrate and the sample holder.

3.2.3. Atomic Force Microscopy

Atomic force microscopy (AFM) measurements were carried out on a digital instrument Nanosurf easyscan 2 AFM. The imaging mode used was tapping mode (Intermittent contact), the cantilever was drive to oscillate up and down near its resonance frequency by a small piezoelectric element mounted in the AFM tip holder similar to non-contact mode. However, the amplitude of this oscillation was greater than 10 nm, typically 100 to 200 nm. Due to the interaction of forces was acting on the cantilever when the tip came close to the surface, Van der Waals force, dipole-dipole interaction, electrostatic forces, etc. caused the amplitude of this oscillation to decrease as the tip gets closer to the sample. An electronic servo used the piezoelectric actuator to control the height of the cantilever above the sample. The servo adjusted the height to maintain a set cantilever oscillation amplitude as the cantilever was scanned over the sample. A tapping AFM image was therefore produced by imaging the force of the intermittent contacts of the tip with the sample surface. This method of "tapping" lessens the damage done to the surface and the tip compared to the amount done in contact mode. A dynamic frequency cantilever of ~150 kHz is used.

3.3. Photoelectrochemical Measurements

3.3.1. I-V Measurements

The I-V measurements were performed in a 30 ml glass cell with a quartz window at room temperature, using a rutile TiO_2 (100), (001) or (110),

anatase (101) or thin-film substrate as working electrode, an Ag/AgCl/NaCl (sat) reference electrode, a Pt counter electrode and 20 ml electrolyte solution. Data acquisition was performed with a Zahner IM6e electrochemical workstation. A 250 W Xe lamp served as light source during I-V measurements, the incident light intensity at the electrode surface being 5 mW cm^{-2}. The supporting electrolyte was 0.1 M KCl dissolved in ultra-pure water.

3.3.2. Impedance Measurements

The impedance measurements were carried out in the dark at room temperature in a 30 ml glass cell, using a rutile TiO$_2$ (100), (001) or (110), anatase (101) or thin-film substrate as working electrode, an Ag/AgCl/NaCl (sat) reference electrode, a Pt counter electrode and 20 ml electrolyte solution. Data acquisition was performed with a Zahner IM6e electrochemical workstation. A frequency of 5kHz was used in all Mott-Schottky measurements. The supporting electrolyte was 0.1 M KCl dissolved in ultra-pure water. Aqueous methanol solutions were prepared by addition of pure methanol (Roth, analytical grade 99.9%).

3.3.3. IMPS Measurements

All IMPS measurements were carried out at room temperature in a 30 ml glass cell with a quartz window, using a rutile TiO$_2$ (100), (001) or (110), anatase (101) or thin-film substrate as working electrode, an Ag/AgCl/NaCl (sat) reference electrode, a Pt counter electrode and 20 ml electrolyte solution as schematically shown in Figure 3.1. Data acquisition was performed with a Zahner IM6e electrochemical workstation. A UV-light emitting diode (UV-LED, 375-380 nm) driven by a Zahner PP210 potentiostat connected to the electrochemical workstation was used as light source for IMPS exhibiting a dc light intensity at the electrode surfaces. The light intensity of the UV-LED

was modulated sinusoidally by ± 8 %. The frequency range was from 5kHz to 1 Hz. All solutions were prepared using reagent grade chemicals. The supporting electrolyte was 0.1 M KCl dissolved in ultra-pure water. Aqueous methanol solutions were prepared by addition of pure methanol (Roth, analytical grade 99.9%).
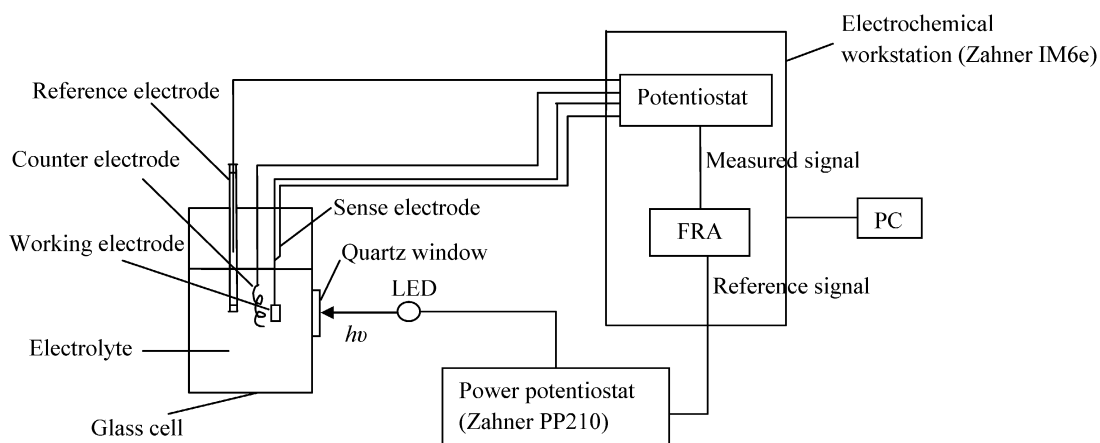
Figure 3.1. Experimental arrangement for intensity modulated photocurrent spectroscopy (IMPS). FRA: frequency response analyzer. LED: light emitting diode.

The photon flux at the TiO_2 electrode surface was measured using ferrioxlate actinometer [103, 104]. Briefly, freshly prepared 10 ml iron(III) sulphate aqueous solution (3.75 mmol) and 10 ml potassium oxalate aqueous solution (11.25 mmol) have been mixed in the cell used for the photoelectrochemical measurements in the dark. Afterwards, 5 ml H_2SO_4 aqueous solution (0.25 M) has been added. Under these conditions, the green colour of the ferrioxalate complex is formed. The cell has been irradiated from the outside using the LED. The quartz window has been covered, i.e., the illuminated area is equal to the electrode area (0.25 cm^2). The ferrioxalate complex absorbs all photons of the incident light and is reduced to iron(II) complex according to the following equation (Eq. 3.1):

$$2[Fe(C_2O_4)_3]^{3-} \xrightarrow{h\nu} 2[Fe(C_2O_4)_2]^{2-} + (C_2O_4)^{2-} + 2CO_2 \quad \text{(Eq. 3.1)}$$
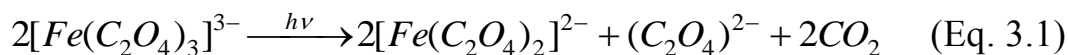
The rate of iron(II) ion formation has been calculated by determining the amount of iron(II) ions after different illumination times using a spectrophotometric method employing 1,10-phenanthroline as reagent [104]. The photon flux has been calculated by dividing the rate of iron(II) ion formation by the quantum yield of the iron(II) ion formation at the applied conditions (0.93 at 380 nm) to be 1.61×10^{15} photons s^{-1}.

3.4. Photocatalytic Measurements

3.4.1. Photocatalytic Hydroxyl Radical Generation

The photocatalytic activities of the different anatase and rutile surfaces have been evaluated by the photocatalytic hydroxylation of terephthalic acid which is usually regarded as an indirect detection of $OH^\bullet$ radicals. Terephthalic acid reacts with the $OH^\bullet$ radicals leading to the formation of 2-hydroxyterephthalic acid according to Eq. 3.2 [105]:
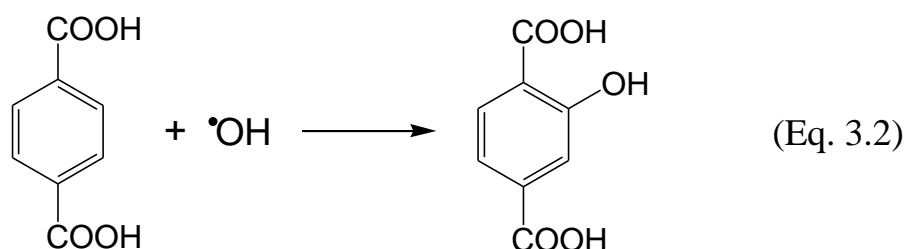
2-hydroxyterephthalic acid exhibits a characteristic fluorescence at 425 nm when excited at 315 nm. Therefore, the $OH^\bullet$ radical formation at the TiO_2 surfaces has been detected by measuring the fluorescence intensity at 425 nm of 2-hydroxyterephthalic acid upon excitation at 315 nm. The different electrodes have been immersed in standard rectangular quartz cuvettes containing 2 ml 4×10^{-4} M basic solution of terephthalic acid and have been illuminated by UV(A) light (15 mW cm^{-2}) for different times using a high-pressure Xe-lamp (OSRAM HBO 450 W).

3.4.2. Photocatalytic Methanol Oxidation

The photocatalytic methanol oxidation experiments have been carried out employing 3.5 ml standard rectangular quartz cuvettes. The different electrodes have been immersed in 3 ml 1 vol% aerated methanol aqueous solutions and illuminated by UV(A) light (35 mW cm^{-2}) for different times using a high-pressure Xe-lamp (OSRAM HBO 450 W). Methanol is photocatalytically oxidized to formaldehyde. The produced formaldehyde has been analyzed employing high-performance liquid chromatography (HPLC) using the Nash reagent [106]. Formaldehyde reacts with acetylacetone in the presence of a nitrogen donor such as ammonium acetate to produce a yellow colour owing to the formation of diacetyldihydrolutidine as shown in Eq. 3.3. HPLC measurements were carried out using a ECOM SPOL SR.O. liquid chromatograph system consisting of a pump, a six-port injector with 50 μl loop auto sampler (MARATHOM), an octadecyl reversed-phase (C18) column, and a variable wavelength detector. The mobile phase was a 20:80 acetonnitrile/water isocratic mixture. The operating conditions were as follows: column temperature (ambient), mobile-phase flow rate (1 ml min^{-1}), detection wavelength (412 nm).

(Eq. 3.3)
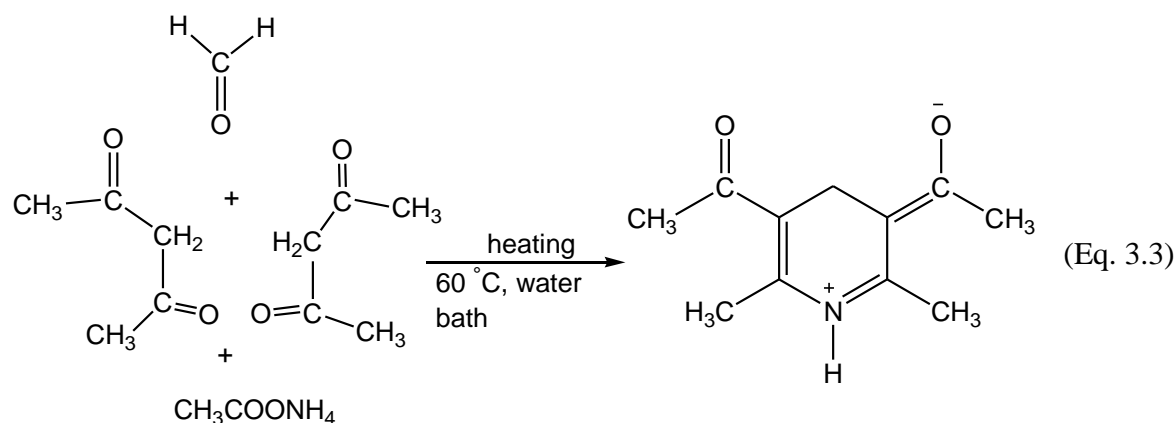
4. Results

4.1. Characterization of the TiO$_2$ Surfaces

4.1.1. X-ray Diffraction

The TiO$_2$ rutile single crystal surfaces have been characterized by X-ray diffraction (XRD). The X-ray diffraction patterns of the rutile TiO$_2$ (100), (001), and (110) surfaces are shown in Figure 4.1.a, b and c, respectively. It is obvious from the high intensity of the diffraction located at 39.2^0 (2θ) in the XRD pattern shown in Figure 4.1.a that the rutile TiO$_2$ (100) surface is of high quality. No other reflections have been observed indicating the perfect crystal growth in the [100] direction. Figure 4.1.b shows the X-ray diffraction pattern of the rutile TiO$_2$ (001) face. The obtained pattern exhibits only one diffraction located at 62.7^0 (2θ) indicating a perfect (001) surface. Figure 4.1.c shows two diffraction peaks located at 27.4 and 56.62^0 (2θ) which are characteristic diffractions for the (110) surface.

The anatase single crystal TiO$_2$ (101) and the anatase TiO$_2$ thin-film surfaces have also been characterized by X-ray diffraction. Figure 4.2.a shows the X-ray diffraction pattern of the TiO$_2$ anatase (101) surface. It is obvious from the very high intensity of the X-ray diffraction located at 25.28^0 (2θ) that the anatase single crystal is of high quality exhibiting a perfect (101) surface. No other reflections have been observed evincing the perfect cutting parallel to the (101) direction. Low intensity diffraction peaks located at 25.28 and 48.05^0 (2θ) appearing in Figure 4.2.b indicate that the TiO$_2$ film is anatase as concluded by comparing the peak positions with the structural data for the commonly known TiO$_2$ phases taken from the PDF-2 database with the following PDF file numbers: anatase [21-1272], rutile [21-1276], brookite [29-1360]. The low intensities of the detected peaks evince that either the thickness of the TiO$_2$ film is very low or the film has low crystallinity. In fact

the thickness of the film is in the range of a few hundreds of nanometers as estimated by using scanning electron microscopy, which makes the first explanation more reasonable.
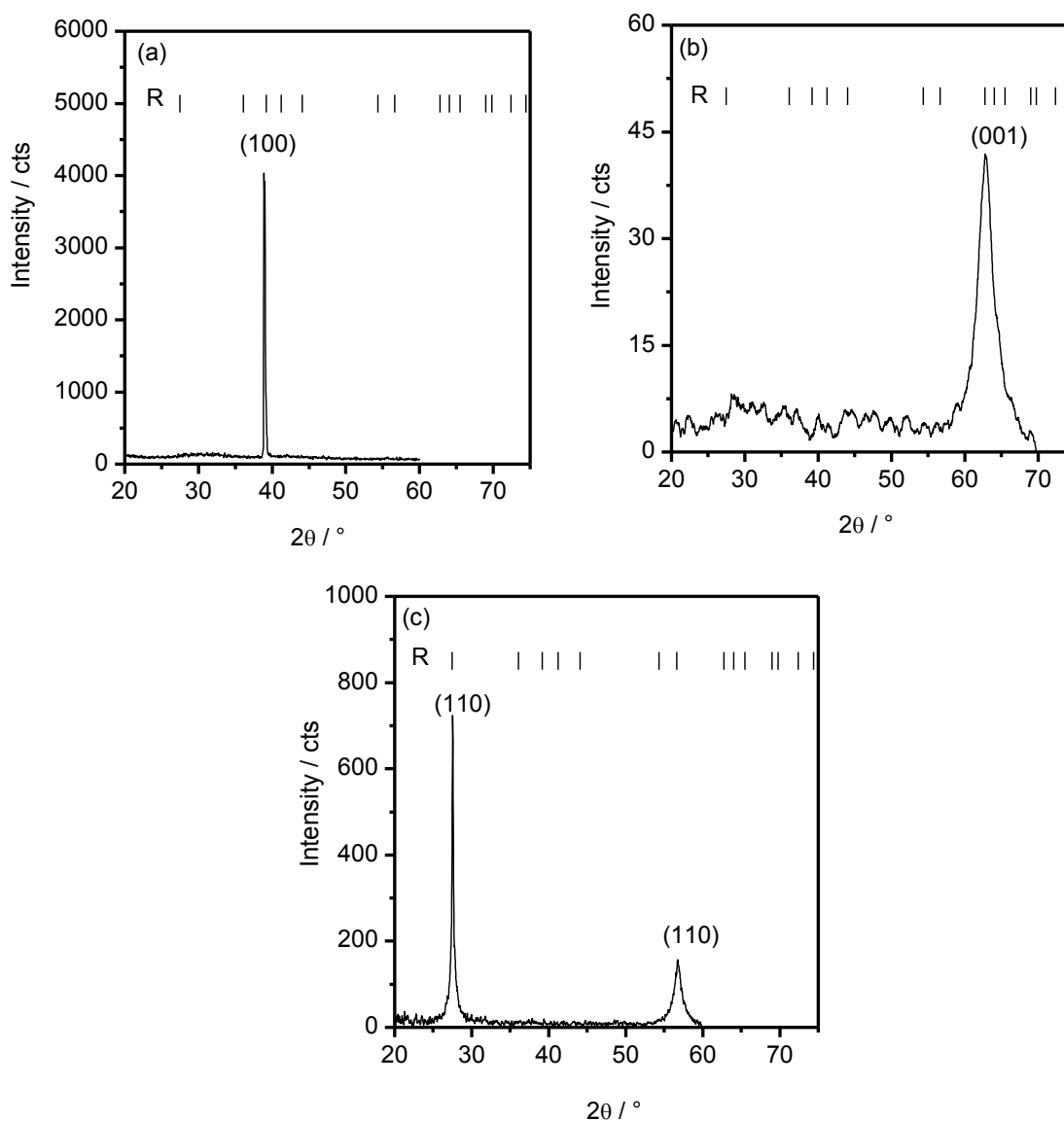
Figure 4.1. XRD diffraction patterns of the rutile TiO_2 single crystal (a) (100), (b) (001), and (c) (110) surfaces. R indicates the diffraction positions of rutile.
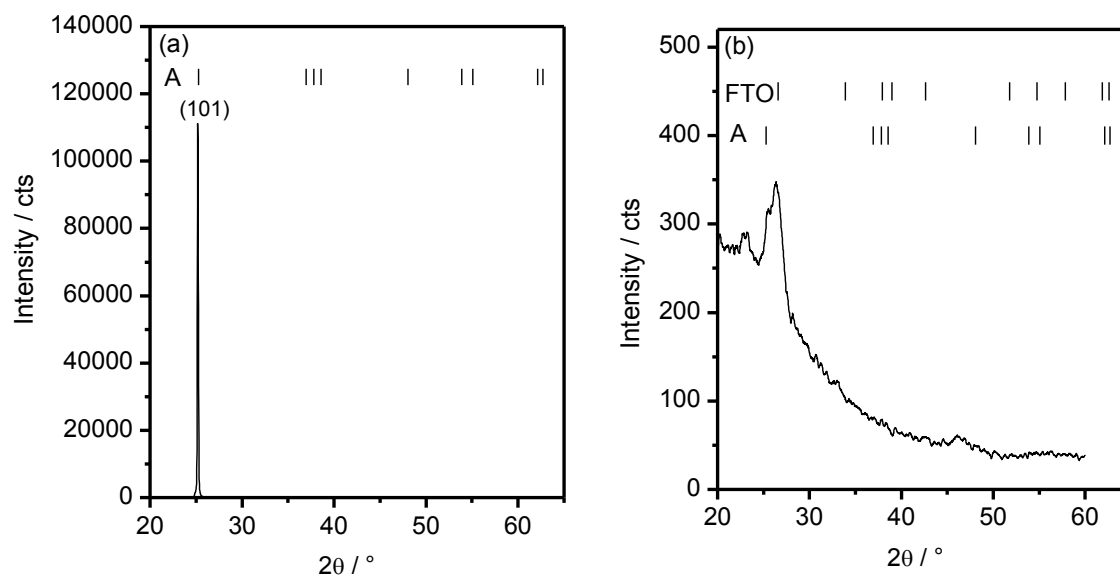
Figure 4.2. XRD diffraction patterns of the anatase TiO_2 (a) single crystal (101) and (b) thin-film surfaces. A indicates the diffraction positions of Anatase.

4.1.2. Scanning Electron Microscopy

The morphologies of rutile TiO_2 have been investigated by scanning electron microscopy (SEM). The obtained SEM micrographs of the rutile TiO_2 (100), (001) and (110) are shown in Figure 4.3.a, b and c, respectively. It is obvious from these micrographs that the rutile TiO_2 single crystal surfaces (100) and (110) are flat, whereas the rutile TiO_2 (001) surface has a porous layer, which might be formed as a result of the heat treatment of the TiO_2 (001) surface under hydrogen gas flow. This observation is in agreement with the published results indicating that the TiO_2 (001) surface is less stable than the other two rutile surfaces, i.e., the TiO_2 (100) and (110) surfaces, under heat treatment conditions [100]. This inactive film hinders the IMPS measurements as will be discussed in the following sections. To remove this layer, the TiO_2 (001) surface has been photoetched and characterized by scanning electron microscopy again. Figure 4.3.d shows the SEM micrograph of the TiO_2 (001) surface following the photoetching process. It can be clearly

seen that the porous layer has been successfully removed and a flat surface has been obtained.
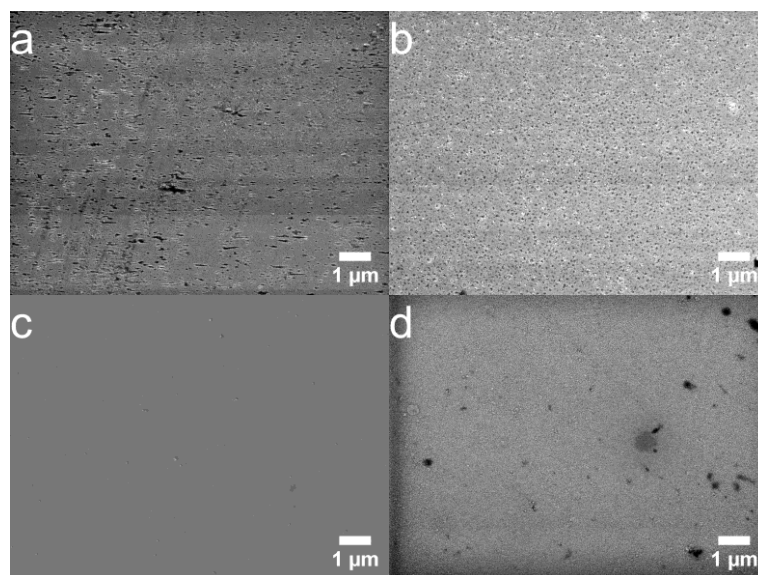
Figure 4.3. SEM of the rutile TiO_2 single crystal (a) (100), (b) (001), and (c) (110) surfaces; and (d) (001) surface after photoetching.

Figure 4.4.a and (b, c) show the SEM micrographs of anatase TiO_2 single crystal and thin-film, respectively. It is obvious from Figure 4.4.a that the anatase single crystal has a rough and irregular surface. Figure 4.4.b and c show the micrographs of the anatase TiO_2 thin-film, it can be seen from these two micrographs that the anatase thin-film exhibits a flat and smooth surface and its thickness can be estimated to be around a few hundreds of nanometers according to the micrograph shown in Figure 4.4.c.
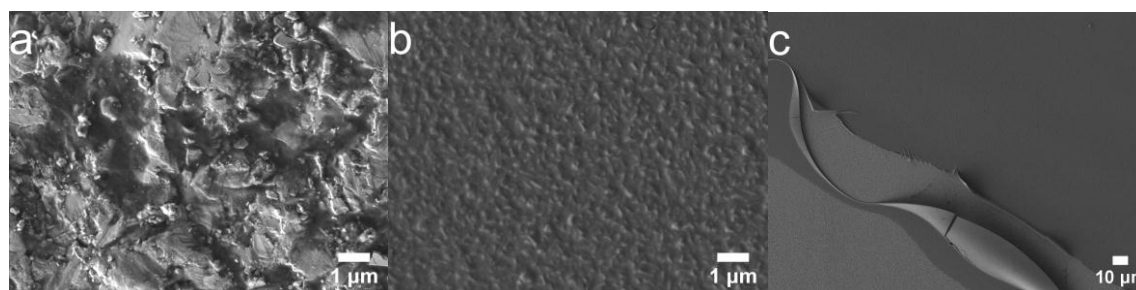
Figure 4.4. SEM of the anatase TiO_2 single crystal (a) (101) and (b, c) thin-film surfaces.

4.1.3. Atomic Force Microscopy

The roughness of rutile TiO_2 single crystal surfaces has been investigated by atomic force microscopy (AFM). The two and three dimensional atomic force microscopy images for rutile TiO_2 (100), (001), and (110) surfaces are shown in Figure 4.5.a, b, and c, respectively. The images show nearly flat surfaces with similar roughness (R_a) values $\leq$ 1 nm, namely 0.7 to 1 nm, 0.6 to 1 nm and 0.3 to 0.8 nm for the rutile TiO_2 (100), (001) and (110) surfaces, respectively. It is worth to mention that the rutile TiO_2 (001) surface has been characterized by AFM after the photoetching process.
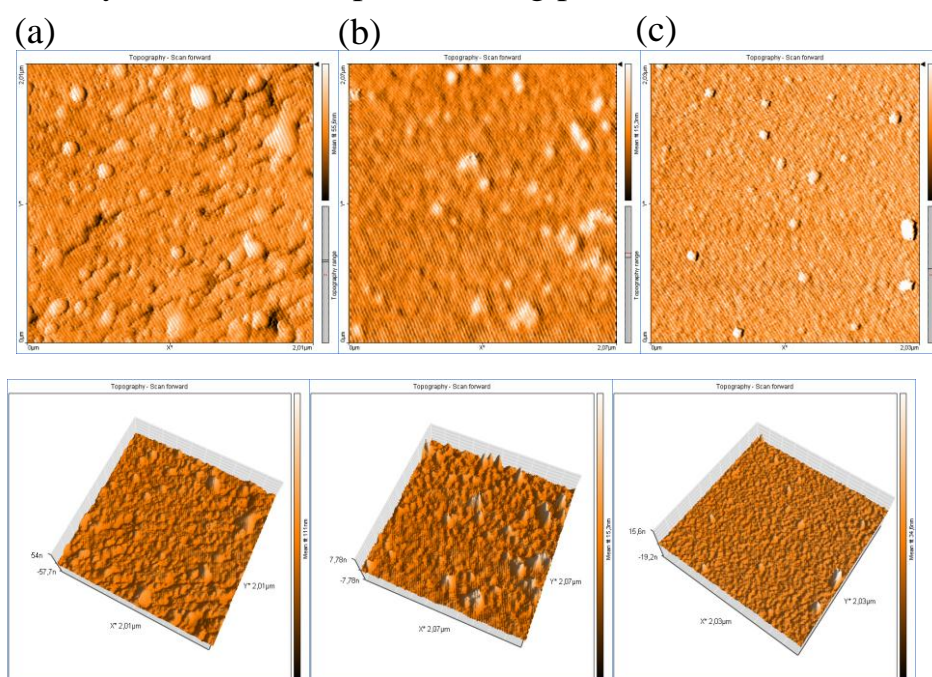
Figure 4.5. Two and three dimensional AFM images of the rutile TiO_2 single crystal (a) (100), (b) (001), and (c) (110) surfaces.

Figure 4.6.a and b show the two and three-dimensional AFM images of anatase single crystal (101) and thin-film, respectively. It is obvious from Figure 4.6.a and b that the anatase TiO_2 single crystal and the TiO_2 thin-film exhibit rough surfaces with roughness (R_a) values of 23 to 26 nm and 13 to 15 nm, respectively.
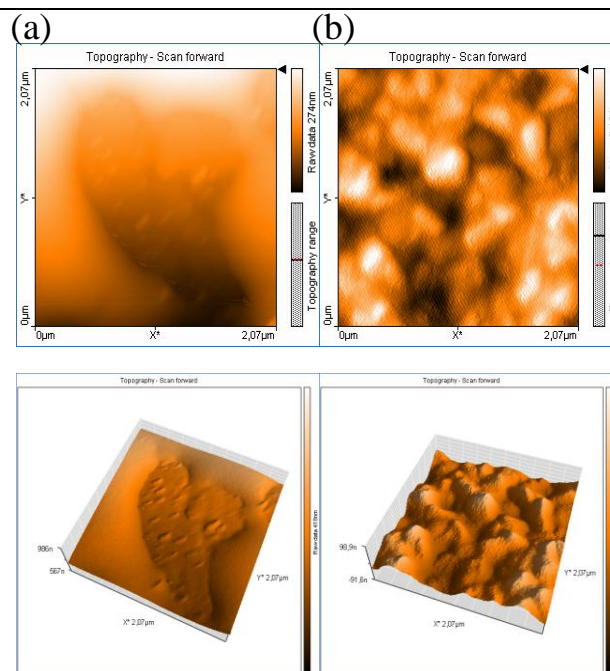
Figure 4.6. Two and three dimensional AFM images of (a) anatase TiO$_2$ single crystal (101) and (b) thin-film surfaces.

4.2. Photoelectrochemical Oxidation of Water and Methanol

4.2.1. I-V Curves

I-V curves of the TiO$_2$ electrodes have been measured in order to determine the potentials of photocurrent onset and photocurrent saturation. In general, IMPS measurements are usually performed in the photocurrent onset region, since recombination and therefore the typical semicircle in the IMPS complex plane plot disappear in the saturation region, for this reason it is very important to perform I-V measurements before doing IMPS measurements.

For the rutile TiO$_2$ (001) electrode, it was found that an inactive thin surface layer is formed during H$_2$ treatment as previously reported [100] and supported in this study by scanning electron microscopy measurements (SEM) (see Figure 4.3.b and d). For this reason, it was essential to remove this inactive film by photoetching before the IMPS measurements. It was not possible to obtain a well-resolved IMPS response without photoetching of the

rutile TiO$_2$ (001) surface. After photoetching of the rutile TiO$_2$ (001) surface, a three-fold increase of the current under illumination is observed (see Figure 4.7). At the same time, the current decreases in the dark. Both observations can be explained by the presence of surface states initially present at the electrode surface, which may promote charge transfer in the dark, while, however, leading to an increased recombination of photogenerated holes under illumination. Following these results, the photoetched rutile TiO$_2$ (001) electrodes have been employed for all further IMPS investigations, whereas the rutile TiO$_2$ (100) and (110) surfaces have been employed without photoetching, since no notable changes have been observed due to photoetching.
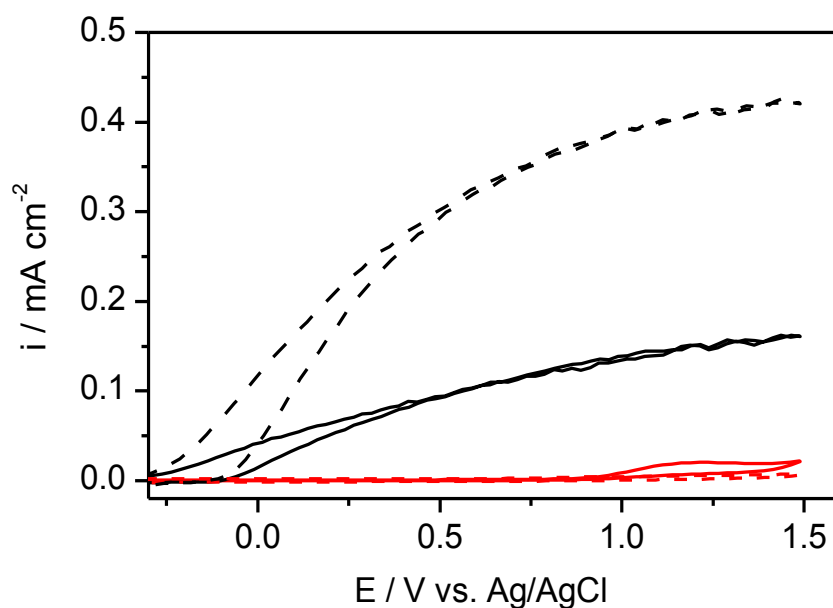
Figure 4.7. I-V curves measured at the rutile TiO$_2$ (001) surface in the dark (red) and under illumination (black) with 250 W Xe lamp in 0.1M KCl (aq), scan rate = 200 mV s^{-1}. The measurements have been made before (solid lines) and after (dashed lines) photoetching.

Figure 4.8.a, b and c show the I-V curves for the rutile TiO$_2$ single crystal (100), (001), and (110) surfaces, respectively. The measurements have been performed in the dark and under illumination employing aqueous 0.1 M KCl

solution. As it is typical for n-type semiconductors, all the electrodes show anodic photocurrents towards positive potentials corresponding to the photooxidation of water (or adsorbed OH⁻). The increase in the photocurrent in case of the rutile TiO_2 (100) face (see Figure 4.8.a) is rather fast, but already reaches a saturation value at +0.3V vs. Ag/AgCl. The photocurrent increase of the rutile TiO_2 (110) face is about equally fast, but it further increases to a much higher saturation value, which is therefore reached at a more positive value: +0.75V vs. Ag/AgCl (see Figure 4.8.c). Figure 4.8.b shows that the photocurrent of the TiO_2 (001) face increases rather slowly and a saturation level is still not reached at the highest employed potential of +1.5V vs. Ag/AgCl.
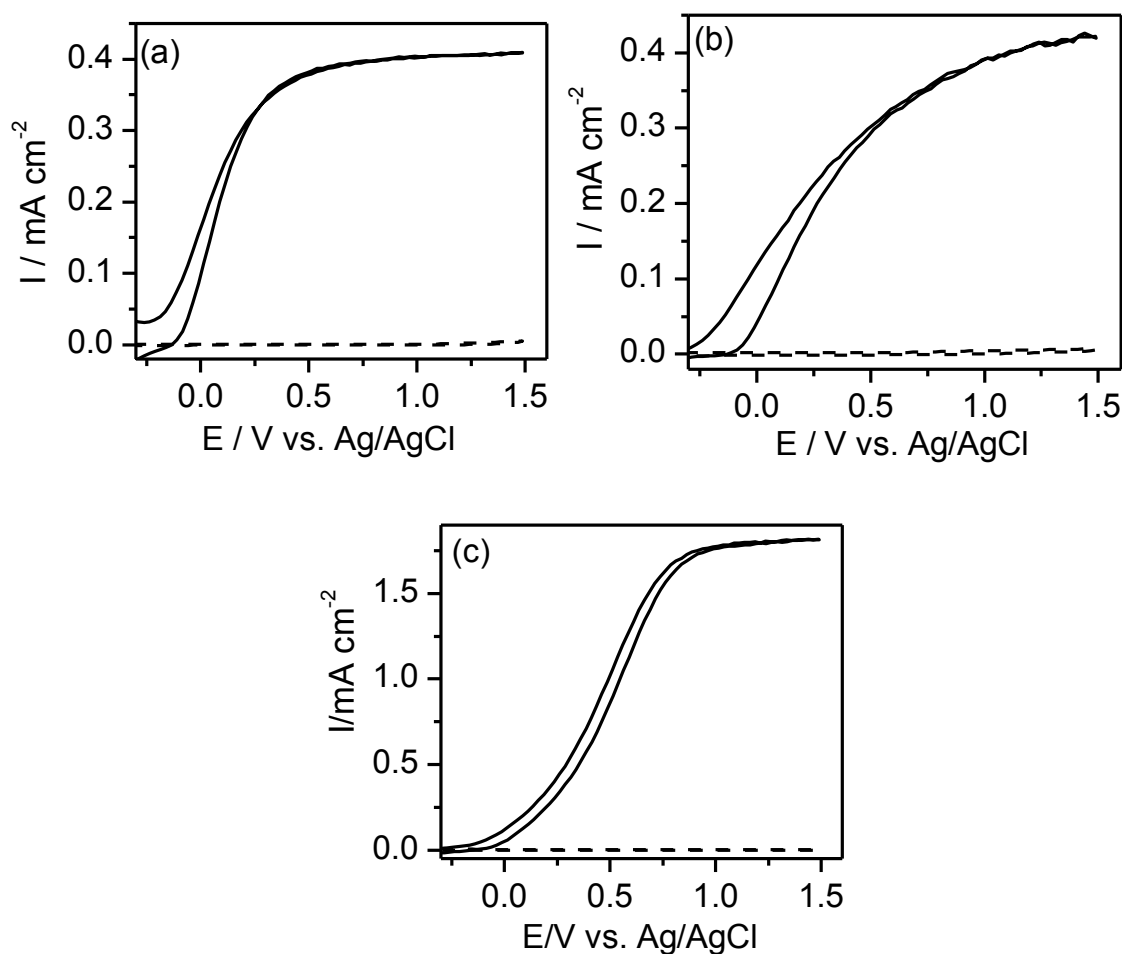
Figure 4.8. I-V curves measured at the rutile TiO_2 single crystal (a) (100), (b) (001) and (c) (110) surfaces in the dark (dashed) and under illumination (solid) with 250 W Xe lamp in 0.1M KCl (aq), scan rate = 200 mV s^{-1}.

For the rutile TiO_2 (110) face (see Figure 4.8.c) it is observed that the photocurrent is higher than in case of the (100) and (001) faces by factors of 4.5, at a potential of +1.0 V vs. Ag/AgCl, indicating different activities of the surfaces towards water oxidation under the given conditions. Note that these differences are observed despite similar roughnesses of the surfaces (see 4.1.3) and comparable flatband potentials. The latter is proven by the fact that all rutile TiO_2 electrodes investigated here have the same photocurrent onset value of -0.3V vs. Ag/AgCl (see Figure 4.8.a, b and c). Figure 4.9.a and b shows the I-V curves of anatase TiO_2 single crystal and thin-film electrodes, respectively. It can be clearly observed from Figure 4.9.a that the photocurrent is quite low in comparison with that of the rutile single crystal surfaces. The anatase TiO_2 (101) electrode surface area is 0.09 cm^2, the highest possible surface area obtained from naturally grown anatase single crystals. The photocurrent normalized to the same surface area as for rutile single crystal electrodes has been calculated to be 35 $\mu A/0.25$ cm^2 at 1.0 V vs. Ag/AgCl. Due to the higher band gap of anatase as compared with that of rutile, i.e., 3.2 eV for anatase [107] and 3.0 eV for rutile [108], the plateau current for anatase is lower than that for rutile, i.e., due to the larger band gap only a smaller portion of light can be absorbed. In addition, the onset of the anodic photocurrent of the former is displaced negatively by -0.25V with respect to the latter, which is in good agreement with the results published by Kavan et. al. [108]. This confirms that the increased band gap of anatase affects only the position of the conduction band edge and not that of the valence band edge. It has been also observed from Figure 4.9.a that the photocurrent increases very slowly towards positive potentials without reaching a saturation value, which implies the presence of surface states acting as a recombination centers. The I-V curve of the TiO_2 thin-film electrode is shown in Figure 4.9.b. By comparison of the photocurrent at the

plateau for the anatase thin-film and the anatase single crystal, i.e., 0.35 and 0.14 mA per 1.0 cm^2 at 1.0 V vs. Ag/AgCl, respectively, it has been found that the photocurrent at the anatase thin-film is almost 2.5 times higher than that at the anatase single crystal. Since the roughness of the thin-film is even lower than that of the anatase single crystal, different crystal orientations, like in the case of the different rutile surface, are the most probable explanation for the observed difference.
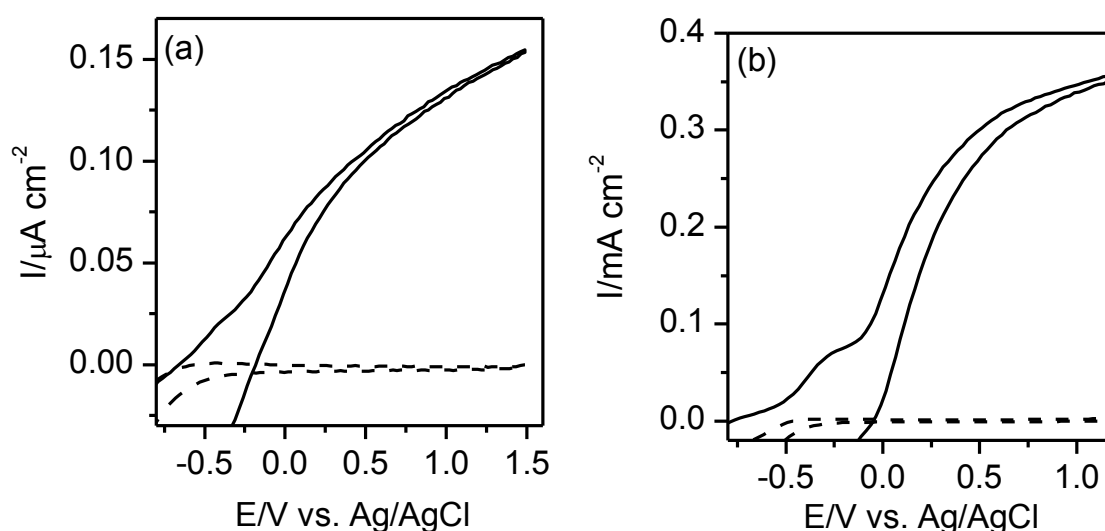
Figure 4.9. I-V curves measured at the anatase TiO$_2$ (a) single crystal (101) and (b) thin-film surfaces in the dark (dashed) and under illumination (solid) with 250 W Xe lamp in 0.1M KCl (aq), scan rate = 200 mV s^{-1}.

4.2.2. Frequency-Resolved Measurements

4.2.2.1. Impedance Measurements

The impedance measurements have been performed for the heat-treated TiO$_2$ electrodes as described in the experimental section and these measurements have been done employing a frequency of 5 kHz. The flatband potentials of TiO$_2$ semiconductor electrodes at the semiconductor/electrolyte junction can be obtained from Mott-Schottky plots (measured in the dark) using the following equation [109, 110].

$$\frac{1}{C_{SC}^2} = \frac{2}{\varepsilon\varepsilon_0 q N_D A^2}(E - E_{FB} - k_B T/q) \qquad\qquad \text{(Eq. 4.1)}$$

where C_{SC} is the capacitance of the space charge layer, ε the dielectric constant of the semiconductor, ε_0 the vacuum permittivity, A the actual area of the electrode exposed to the electrolyte, N_D the donor density, E the applied potential, E_{FB} the flatband potential, q the elementary charge, k_B the Boltzmann´s constant and T the temperature. Plotting C_{SC}^{-2} vs. E should thus yield a straight line, intersecting the potential axis at E_{FB}-$k_B T/q$.

According to Eq. 4.1 N_D can be obtained from the slope of the C_{SC}^{-2} vs. E plot. Eq. 4.1 assumes that $C_{SC} < C_H$, where C_H is the Helmholtz layer capacitance, which means that the applied voltage fully drops in the space charge (SC) depletion layer. However, when the potential drop in the Helmholtz layer $\Delta\varphi_H$ is not negligible, which is the case for high $N_D \geq 10^{19}$ cm^{-3} and/or small C_H, De Gryse et al. [109] showed that Eq. 4.1 must be substituted by the following equation:

$$\frac{1}{C^2} = \frac{1}{C_H^2}[1 + (\frac{2C_H^2}{\varepsilon\varepsilon_0 q N_D A^2})(E - E_{FB} - \frac{k_B T}{q})] \qquad\qquad \text{(Eq. 4.2)}$$

Eq. 4.2 predicts the same slope as Eq. 4.1, but E_o is shifted towards more negative potentials by an amount ΔV given by

$$\Delta V = \frac{\varepsilon\varepsilon_0 q N_D}{2C_H^2} \qquad\qquad \text{(Eq. 4.3)}$$

Mott-Schottky plots measured at rutile TiO$_2$ (100), (001) and (110) surfaces at different methanol contents in the electrolyte are shown in Figure 4.10.a, b, and c, respectively. The corresponding doping densities N_D and flatband potentials E_{FB} have been calculated from the slopes and intersections with the potential axis, respectively, according to the Mott-Schottky relationship (Eq.

4.1). The N_D values have been calculated assuming a dielectric constant of 173 [108] for rutile and they are summarized in Table 4.1.
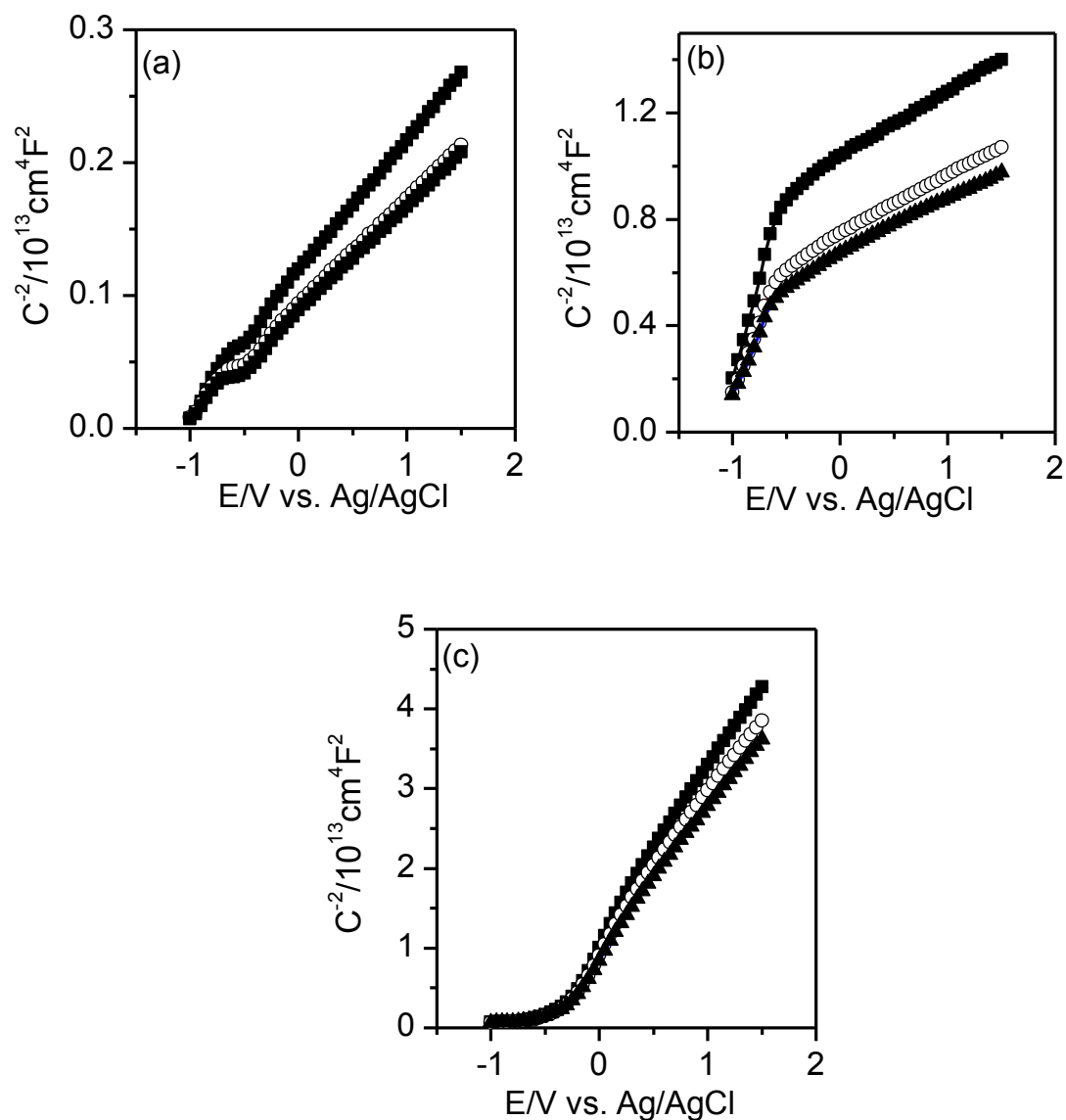
Figure 4.10. Influence of methanol addition on the Mott-Schottky plots of the rutile TiO_2 single crystal (a) (100), (b) (001) and (c) (110) electrodes in 0.1M KCl (aq): 0% (■), 1% (○) and 10% (▲) methanol.

Table 4.1. Flatband potentials E_{FB} and doping densities N_D extracted from Mott-Schottky plots of the rutile TiO_2 single crystals measured at a frequency of 5 kHz in 0.1 M KCl (aq) in the dark.

Rutile TiO_2 surface	methanol content / vol%	E_{FB} / V vs. Ag/AgCl	N_D / 10^{19} cm^{-3}
(001)	0	-1	0.53
(001)	1	-1	0.59
(001)	10	-1	0.63
(100)	0	-0.95	1.31
(100)	1	-0.94	1.61
(100)	10	-0.94	1.62
(110)	0	-0.9	0.07
(110)	1	-0.9	0.07
(110)	10	-0.9	0.08

Figure 4.11.a and b shows the Mott-Schottky plots of the anatase single crystal (101) surface and the anatase thin-film, respectively. The corresponding doping densities N_D and flatband potentials E_{FB} have been also calculated from the slopes and intersections with the potential axis, respectively, according to the Mott-Schottky relationship (Eq. 4.1). The N_D values have been calculated assuming a dielectric constant of 31 for anatase and they are summarized in Table 4.2 [108, 111].
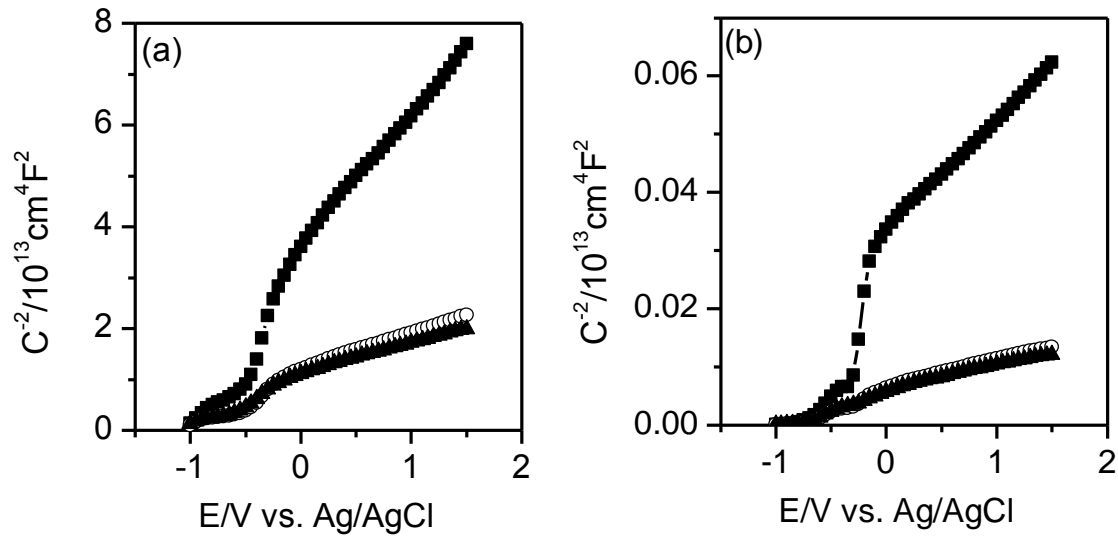
Figure 4.11. Influence of methanol addition on the Mott-Schottky plots of the anatase TiO$_2$ (a) single crystal (101) surface and (b) thin-film electrodes in 0.1M KCl (aq): 0% (■), 1% (○) and 10% (▲) methanol.

Table 4.2. Flatband potentials E_{FB} and doping densities N_D extracted from Mott-Schottky plots of anatase TiO$_2$ measured at a frequency of 5 kHz in 0.1 M KCl (aq).

Anatase TiO$_2$ surface	methanol content / vol%	E_{FB} / V vs. Ag/AgCl	N_D / 10^{19} cm^{-3}
(101)	0	-1.2	2.22
(101)	1	-1.2	8.33
(101)	10	-1.2	9.97
(thin-film)	0	-1.2	2.39
(thin-film)	1	-1.2	10
(thin-film)	10	-1.2	11.5

Table 4.1 summarizes the values of E_{FB} and N_D for rutile TiO$_2$ (100), (001) and (110) faces in the absence and presence of 1% and 10% methanol, whereas, Table 4.2 contains the E_{FB} and N_D values for the anatase single crystal (101) surface and the thin-film electrode. Comparison of the E_{FB} values reveals that the addition of methanol to the electrolyte does not lead to a significant shift for all investigated TiO$_2$ electrodes. Since adsorption of ions

or polar molecules usually leads to a shift of E_{FB}, this result strongly suggests that methanol adsorption on the electrodes does not occur in this case, i.e., that the adsorption of water molecules or OH^- ions is much stronger than that of methanol. Hence, direct charge transfer of free photogenerated holes from the valence band of TiO_2 to methanol is unlikely to happen, i.e., oxidation of methanol can only occur via $OH^{\bullet}_{s}$ radicals as described in the Theory chapter 2.3.3.

The N_D values measured at the (100) and (001) single crystals are of the same order of magnitude, which can be expected from the fact that the doping density should be a bulk property and doping in H_2 atmosphere has been carried out in the same way for all samples. However, the N_D value of the (110) crystal is about one order of magnitude lower. Often differences in N_D values can be related to surface properties, since a higher roughness of the surface would lead to a higher measured capacitance and therefore result in a higher calculated N_D value. However, this approach is not suitable in this case, since all rutile electrodes exhibit comparable roughness values (see section 4.1.3). The differences in the N_D values may therefore indicate different behaviour of the single crystals during the doping process, depending on their relation between geometry and crystallographic orientation, and therefore real differences between the doping densities of the electrodes.

Since anatase has a different crystal structure, the same doping conditions are expected to lead to different N_D values. Table 4.2 shows that the N_D values of anatase are up to one order of magnitude higher than those of rutile (100) and (001). The doping densities of all investigated electrodes is quite high and therefore the charge space capacitance cannot be ignored relative to the Helmholtz layer capacitance C_H. Thus, the tabulated flatband potential values

should be corrected by a factor according to Eq. 4.3. The correction terms are calculated to be 0.012 V, 0.018 V and 0.008 V for rutile TiO_2 (100), (001) and (110) surfaces, respectively, based on respective C_H values of 3 µF cm^2, 20 µF cm^2 and 10 µF cm^2 as obtained by fitting the IMPS results (see next section 4.2.2.2). In case of the anatase single crystal (101) surface and the anatase thin-film the correction terms are calculated to be 0.09 V and 0.07 V, respectively, by taking the respective C_H values of 4.3 µF cm^2 and 7.5 µF cm^2. The doping densities can be used to calculate the width of the space charge layer W at the surface of the TiO_2 electrodes employing Eq. 2.4.

Based on the values of E_{FB} and N_D of rutile TiO_2 (100), (001) and (110) single crystal surfaces given in Table 4.1 and those of anatase TiO_2 single crystal (101) surface and thin-film given in Table 4.2, the thickness of the space charge layers at -0.3 and 0 V vs. Ag/AgCl are calculated according to Eq. 2.4 and summarized in Table 4.3. Since the light absorption coefficients of rutile and anatase are around $4x10^4$ cm^{-1} [110] and $1x10^4$ cm^{-1} [112], respectively, in the wavelength region used for illumination of the employed electrodes during the IMPS measurements (UV-LED, 375-380 nm), the percentage of light absorbed within the space charge layer have been calculated by using the Beer–Lambert law. The calculated values are summarized in Table 4.3. These values clearly show that, depending on the potential and the kind of TiO_2 surfaces, only between 2 and 30 % of the light is absorbed within the space charge layer. As will be seen in the IMPS results (section 4.2.2.2), this limits the external quantum efficiency of the photoelectrochemical reactions investigated in this study, since only holes that are photogenerated within the space charge region or in its utmost vicinity reachable by diffusion will be transferred to the electrode surface and are thus able to contribute to the Gärtner flux and therefore to the photocurrent.

Table 4.3. Width of the space charge layer (SCL) extracted from Mott-Schottky plots measured at a frequency of 5 kHz in 0.1 M KCl and the corresponding expected percentage of absorbed light within it.

TiO$_2$ surface	W/nm at -0.3V vs. Ag/AgCl	W/nm at 0V vs. Ag/AgCl	% of light Absorbed in SCL at -0.3V	% of light absorbed in SCL at 0V
100	27	33	6	7
001	50	60	11	13
110	128	156	26	30
101	12	14	3	4
Thin-film	14	15	2	3

4.2.2.2. Intensity Modulated Photocurrent Spectroscopy (IMPS)

The intensity modulated photocurrent spectroscopy is a method using small perturbations in the light intensity that can be used to investigate the kinetics of photoelectrochemical processes. It involves sinusoidal modulation of the illumination intensity and it has been used extensively to investigate a variety of photoelectrochemical reactions at semiconductor electrodes [21, 43].

The potential and methanol concentration effects on the recombination and transfer rate constant on rutile and anatase TiO$_2$ electrodes have been investigated employing the IMPS technique. The complete response of IMPS measurements displayed in complex plane plots exhibit semicircles in the positive/positive quadrant (low frequency) and in the positive/ negative quadrant (high frequency) (see Theory section 2.4.1).

Rutile (100) surface: Figure 4.12.a and b illustrates the influence of the electrode potential in case of rutile TiO$_2$ (100) in aqueous 0.1M KCl before and after addition of 1 vol% methanol at different applied potentials, respectively. Towards positive potentials, a significant increase of I_1 is

observed, while I_2 also increases, however, to a lesser extent. According to Eq. 2.17 in the Theory section, this observation translates into a decrease in k_{rec} relative to k_{tr}.

Comparison of parts a and b in Figure 4.12 reveals that the addition of methanol (Figure 4.12.b) intensifies this trend as is evident from the tendency towards smaller semicircles. Obviously, the presence of methanol as an additional reactant leads to an increase in k_{tr} relative to k_{rec}. The increase of I_2 towards more positive potentials in Figure 4.12.a and b indicates an increase in the Gärtner flux and thereby the external quantum efficiency, which can be attributed to the increasing width of the space charge layer as discussed in section 4.2.2.1. The photon flux employed in these studies was $1.28\text{x}10^{15}$ photons s^{-1} at the electrode surface, with an area of 0.25 cm^2. A differential quantum efficiency of 1.0 under the given conditions (modulation of the light intensity by 8%) would translate into a photocurrent amplitude of $1.32\text{x}10^{-5}$ A, assuming that 20 % of the incident light is lost by reflection [108]. The I_2 values obtained from Figure 4.12 therefore correspond to quantum efficiencies between 2.9 % and 7.2 % at -0.3 V and 0V vs. Ag/AgCl, respectively. The latter value matches well with the value calculated based on light absorption within the space charge layer at 0 V vs. Ag/AgCl (see section 4.2.2.1 Table 4.3), whereas the former is lower than the calculated value, indicating that the rate of recombination within the space charge layer is higher at a potential of -0.3 V vs. Ag/AgCl. This is actually expected due to the increasing electron concentration at the electrode surface towards more negative potentials.
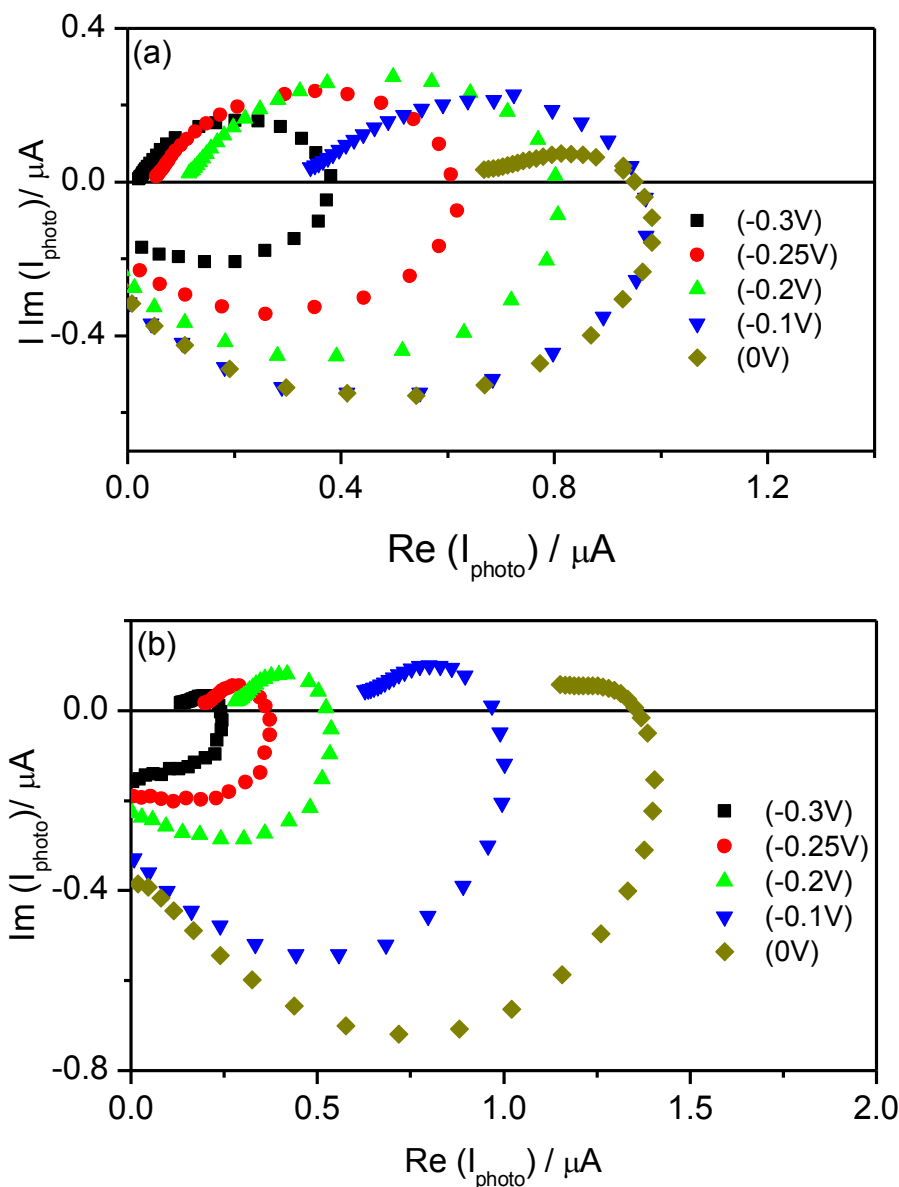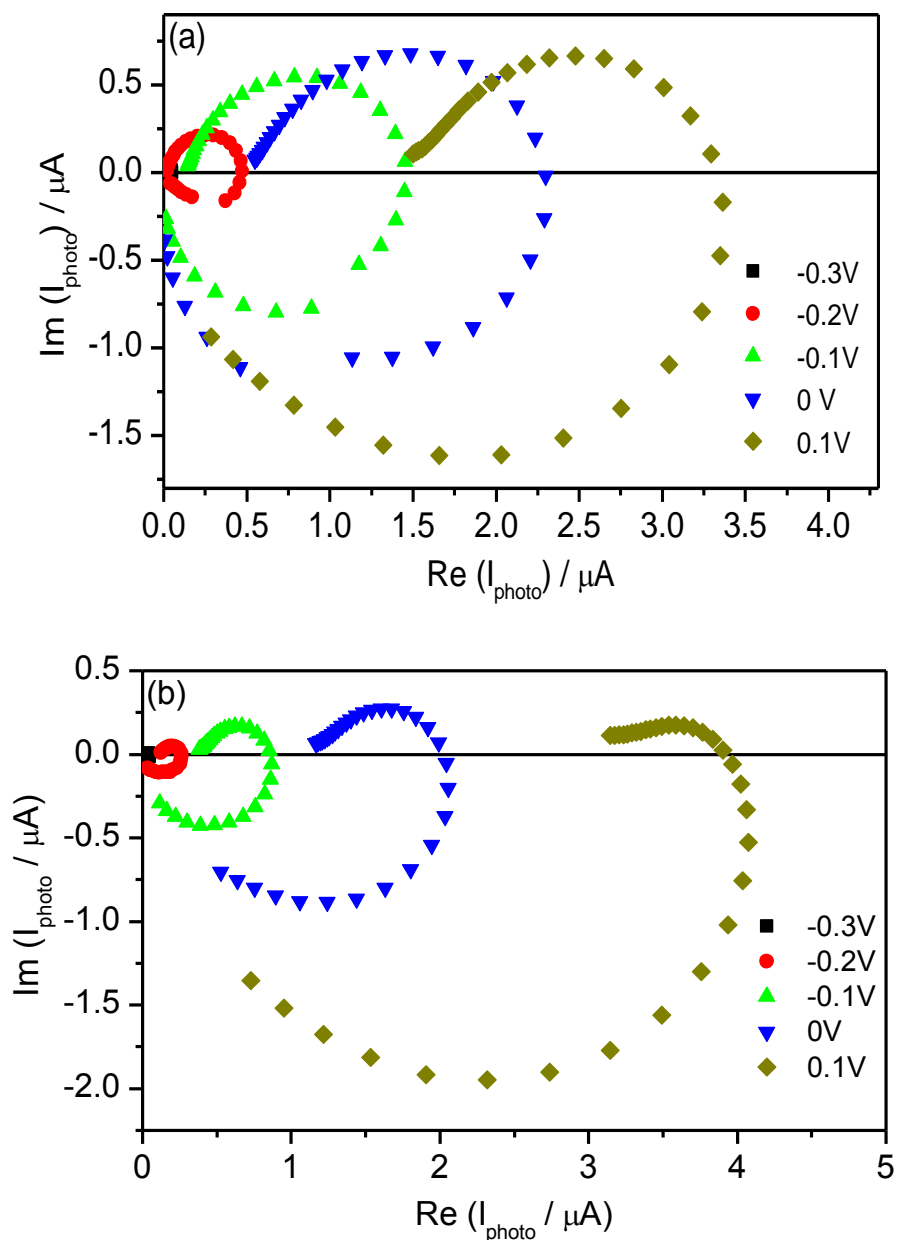
Figure 4.12. IMPS measured at the rutile TiO_2 (100) surface in aqueous 0.1M KCl (a) before and (b) after addition of 1 vol% methanol at different potentials vs. Ag/AgCl.

A clearer illustration of the impact of the methanol concentration can be found in Figure 4.13, where IMPS plots measured with different methanol concentrations at the (100) electrode can be seen. I_2 values are actually decreasing for a methanol content up to 10 % while they remain constant for further increases to 15 and 25%, whereas I_1 increases with increasing methanol concentration. The tendency towards smaller semicircles for higher methanol concentrations again translates into an increase in k_{tr} relative to k_{rec}.

Since the potential is held constant in this case, this is probably due to an absolute increase of k_{tr}, as the electron concentration and therefore the rate of recombination are expected to stay constant as a first approximation. Therefore, the addition of methanol seems to lead to a more efficient charge transfer at the electrode surface.
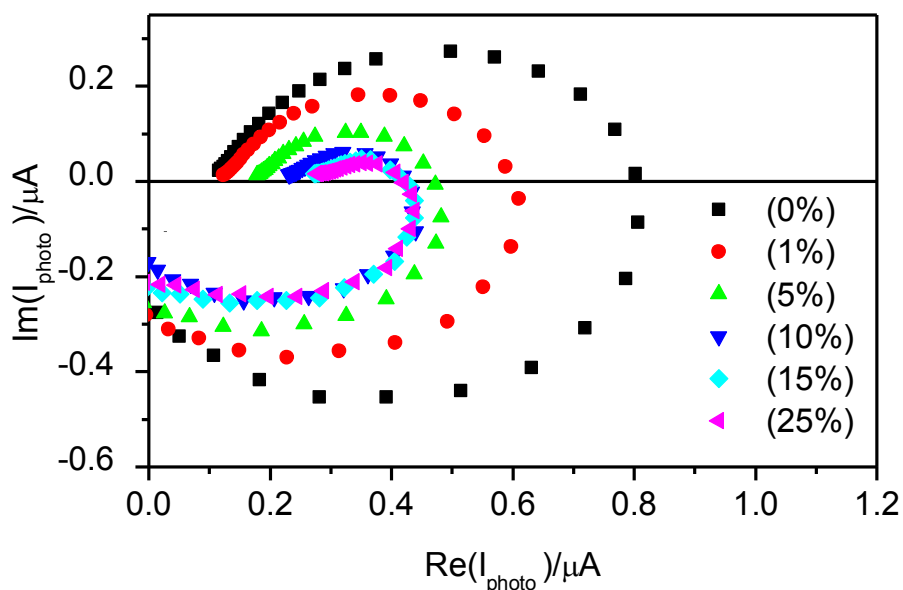
Figure 4.13. IMPS measured at the rutile TiO$_2$ (100) surface in aqueous 0.1M KCl with different methanol concentrations at -0.2 V vs. Ag/AgCl.

Rutile (001) surface: Figure 4.14.a and b shows the IMPS responses measured to investigate the behavior of rutile TiO$_2$ (001) in aqueous 0.1M KCl before and after the addition of 1 vol% methanol at different electrode potentials, respectively. The trends seen upon changing the potential are the same as those seen for the (100) surface, meaning that also at the (001) surface k_{rec} decreases relative to k_{tr} towards more positive potentials. However, as opposed to the behaviour seen for the (100) surface, there is almost no trend towards smaller semicircles upon methanol addition in case of the (001) surface, meaning that the k_{tr}/k_{rec} ratio is not increased by methanol in this case.
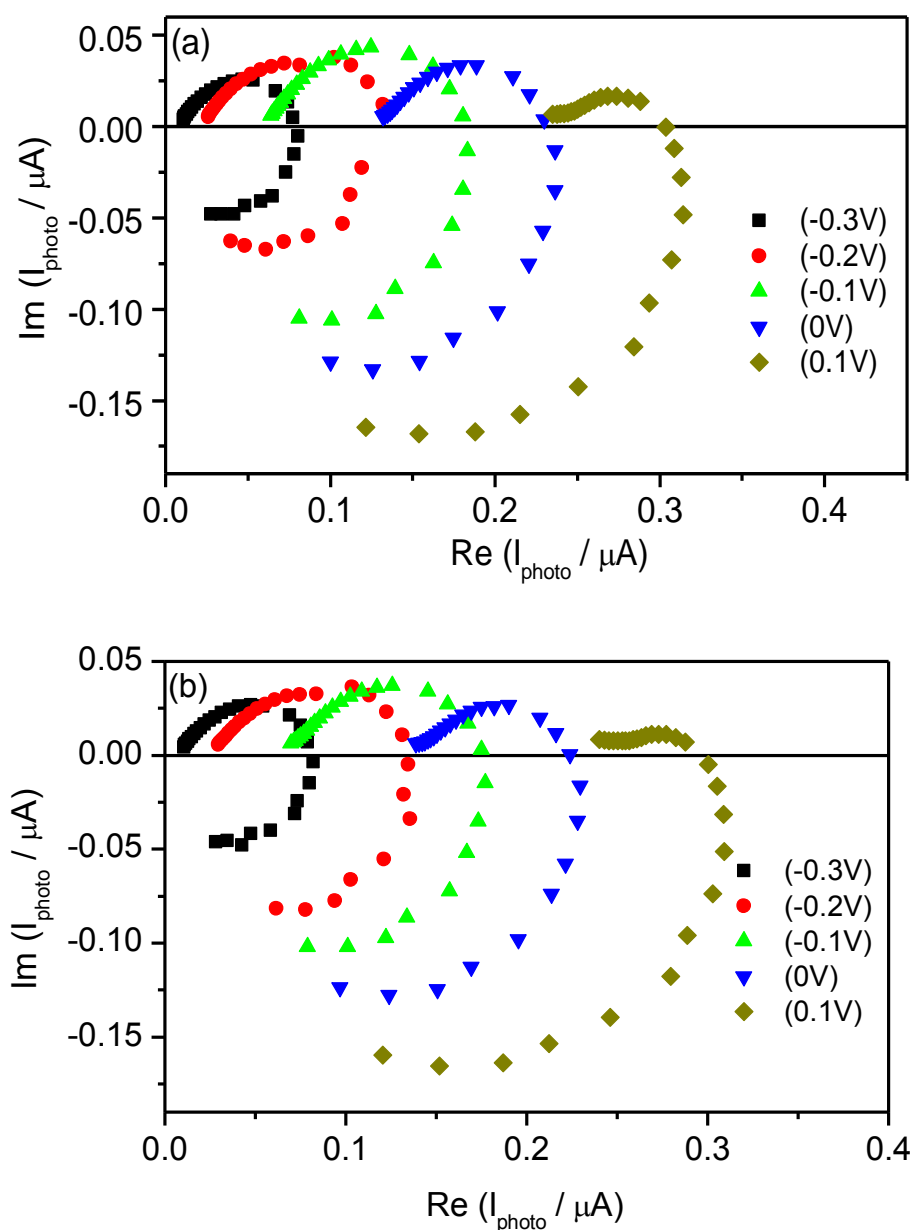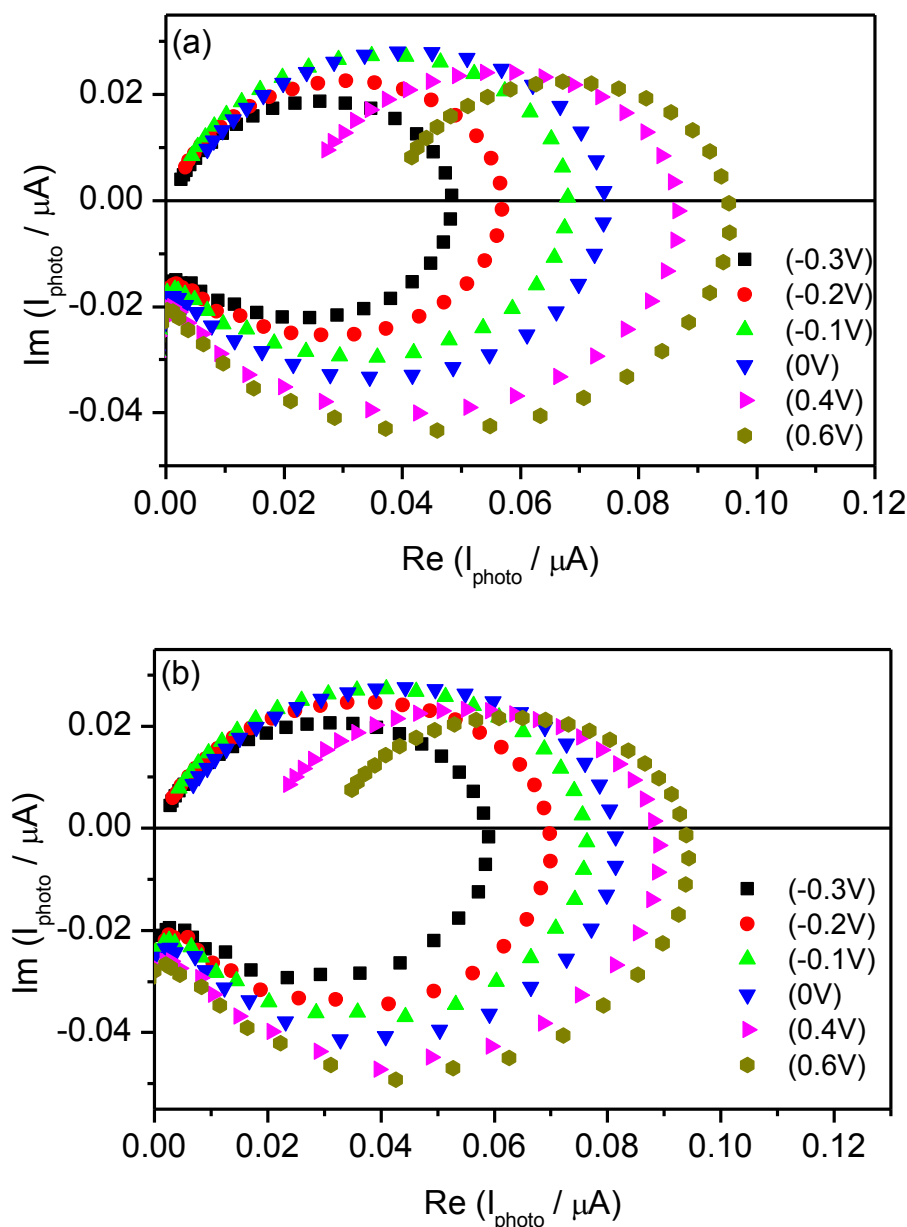
Figure 4.14. IMPS measured at the rutile TiO_2 (001) surface in aqueous 0.1M KCl (a) before and (b) after addition of 1 vol% methanol at different potentials vs. Ag/AgCl.

Again the increase of I_2 towards more positive potentials indicates an increase in the width of the space charge layer. In this case, the I_2 values seen in Figure 4.14 correspond to quantum efficiencies between 0.6 % and 1.7 % at -0.3V and 0V vs. Ag/AgCl, respectively. Both values are lower than those calculated based on the light absorption within the space charge layer (see

section 4.2.2.1 Table 4.3) which can be attributed to the recombination of the charge carriers within the space charge layer.

The influence of methanol addition on the IMPS response of rutile TiO_2 (001) is shown in Figure 4.15. As concluded from Figure 4.14.b in comparison to Figure 4.14.a, it is again clearly seen that methanol addition has a very small influence on the IMPS response compared to the influence which has been seen in the case of the (100) surface (Figure 4.13). Obviously, charge transfer to methanol is much less efficient in case of the (001) surface.
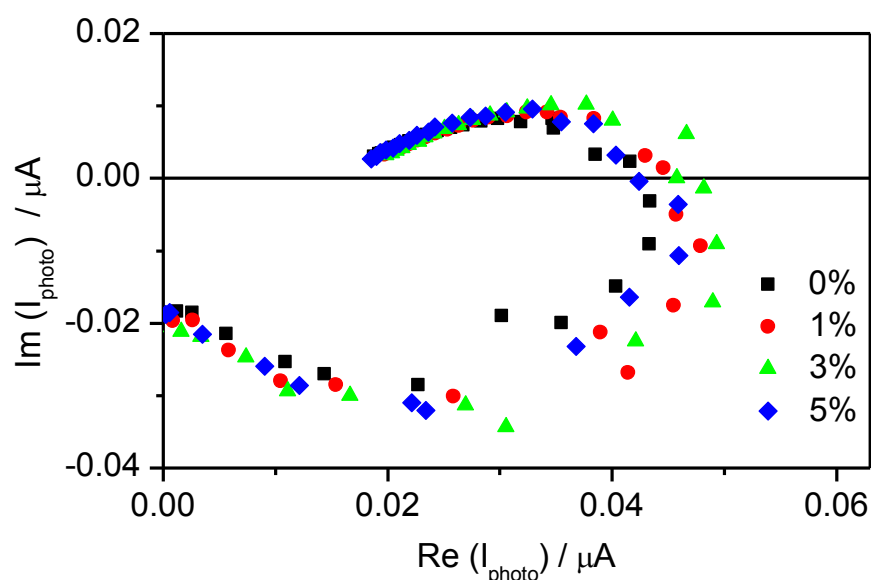
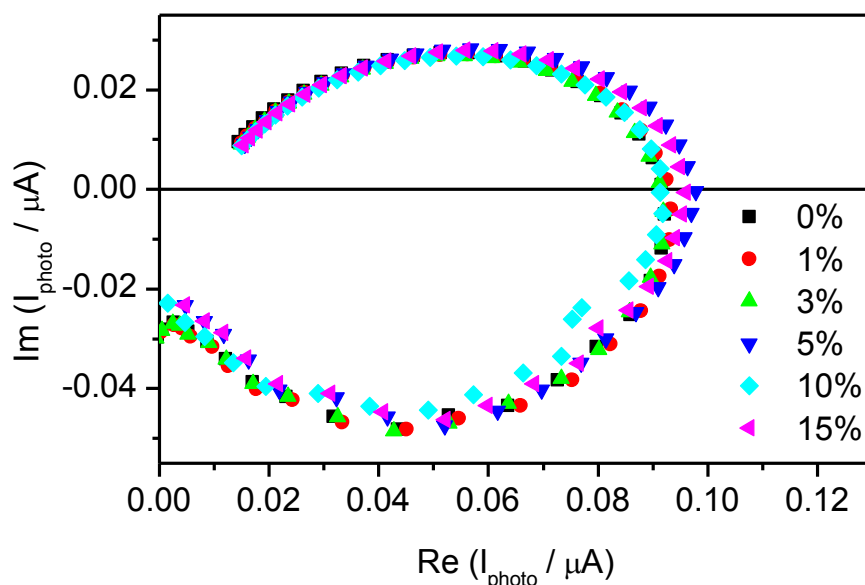**Figure 4.15.** IMPS measured at the rutile TiO_2 (001) surface in aqueous 0.1M KCl with different methanol concentrations at -0.2 V vs. Ag/AgCl.

Rutile (110) surface: The IMPS responses measured on the rutile (110) surface in aqueous KCl solution before and after addition of 1 vol% methanol at different electrode potential are shown in Figure 4.16.a and b, respectively. It is obvious from Figure 4.16.a and b that the I_1 and I_2 values are much more potential dependent than at the (100) and (001) surfaces. Comparison of parts a and b in Figure 4.16 reveals that the addition of methanol (Figure 4.16.b)

has almost the same increasing effect on the k_{tr}/k_{rec} ratio as in case of the (100) surface, which is obvious from the tendency towards smaller semicircles.
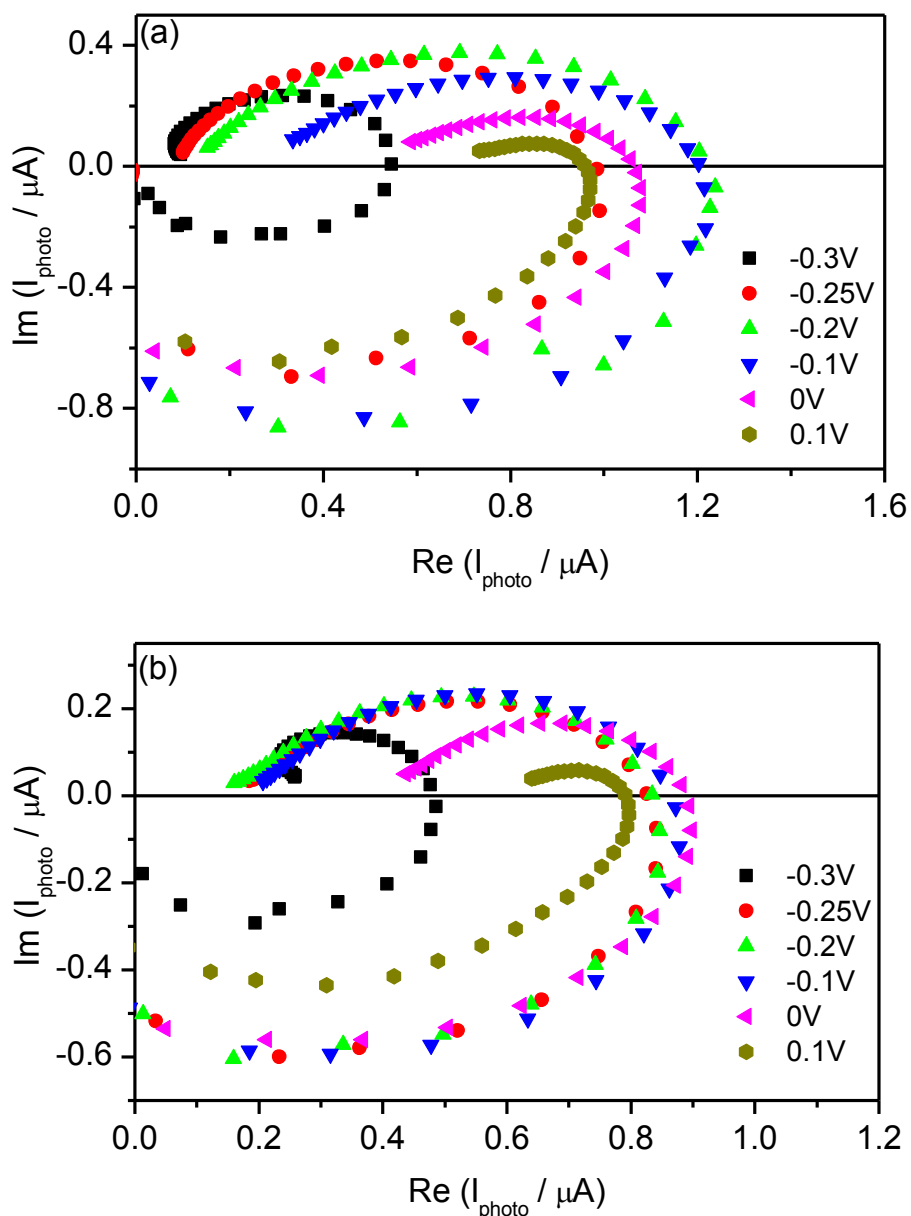

Figure 4.16. IMPS measured at the rutile TiO$_2$ (110) surface in aqueous 0.1M KCl (a) before and (b) after addition of 1 vol% methanol at different potentials vs. Ag/AgCl.

The increasing trend of I_2 towards more positive potential observed in case of (110) is more distinct than that observed for the other two rutile surfaces, i.e., the (100) and (001) surfaces. The I_2 values seen in Figure 4.16.a correspond to quantum efficiencies between 0.44% and 17% at -0.3 and 0V vs. Ag/AgCl, respectively. The later value is almost half of the expected value calculated based on the light absorption within the space charge layer whereas the former is much lower which is expected due to the increased recombination within the space charge layer at more negative potentials (see Table 4.3).

Figure 4.17 presents the influence of methanol addition on rutile TiO_2 (110) single crystals in more detail. As in the case of the (100) face (Figure 4.13), I_1 increases towards higher methanol concentrations. However, I_2 also increases, in case of the (110) face, as opposed to a decreasing trend for the (100) face. Furthermore, again a tendency to smaller semicircles with increasing methanol concentration indicates an increase in the k_{tr} / k_{rec} ratio.
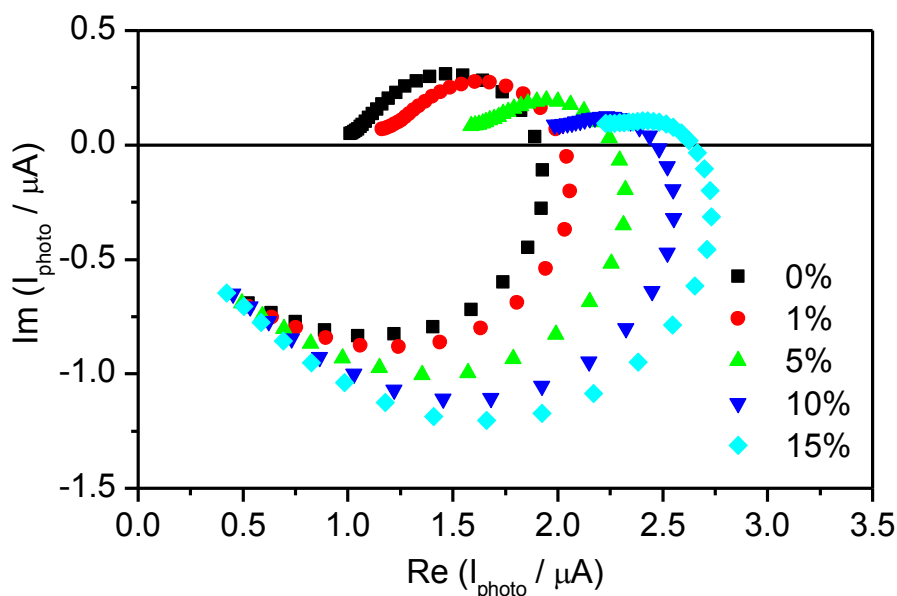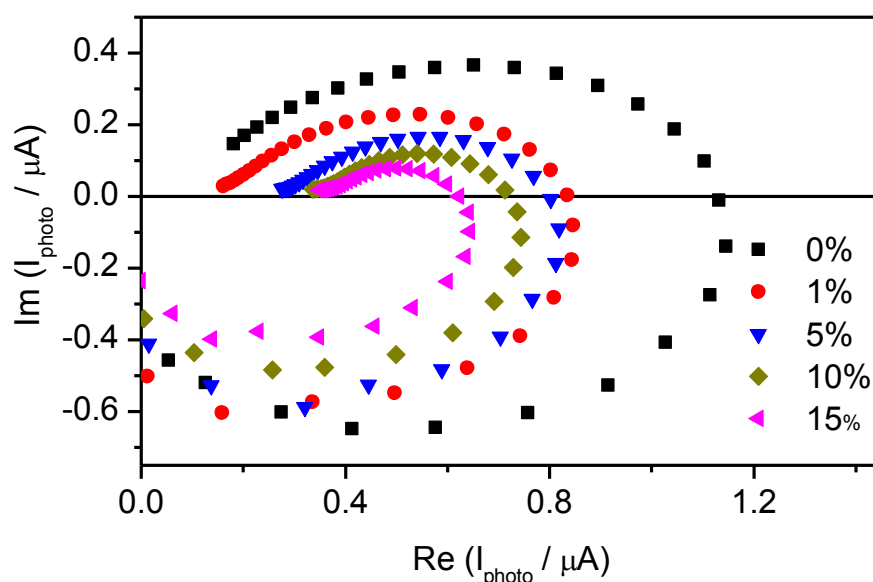

Figure 4.17. IMPS measured at the rutile TiO_2 (110) surface in aqueous 0.1M KCl with different methanol concentrations at -0.2 V vs. Ag/AgCl.

Anatase (101) surface: Figure 4.18.a and b display the IMPS response measured in aqueous 0.1M KCl before and after 1 vol% methanol addition at different electrode potential on the anatase TiO_2 (101) surface. The flattening in the semicircles of the IMPS response shown in Figure 4.18.a and b may be attributed to the roughness of the surface (see Figure 4.4.a).

Figure 4.18. IMPS measured at the anatase TiO_2 (101) surface in aqueous 0.1M KCl (a) before and (b) after addition of 1 vol% methanol at different potentials vs. Ag/AgCl.

Towards more positive potentials, both I_1 and I_2 increase by about the same values, meaning that the k_{tr}/k_{rec} ratio slightly decreases. However, the diameter of the semicircle is almost constant, meaning that even at +0.6V vs. Ag/AgCl there is a rather high rate of recombination. The addition of 1 vol% methanol has only little affect on the shapes and positions of the IMPS semicircles, as it clearly appears from the comparison of Figure 4.18.a and b. The increase of I_2 towards more positive potentials has a lesser extent than for the rutile TiO_2 electrodes. This indicates a smaller increase in the Gärtner flux and thereby the external quantum efficiency, which can be attributed to the small increase in the width of the space charge layer (from 12 nm at -0.3 V vs. Ag/AgCl to 14 nm at 0V vs. Ag/AgCl) as discussed in section 4.2.2.1. Since the light intensity was 4.62×10^{14} photons s^{-1} at the electrode surface with an area of 0.09 cm^2 and the light intensity modulation was 8%, a differential quantum efficiency of 1 under the given conditions would translate into a photocurrent amplitude of 4.74×10^{-6} A assuming 20% light reflection so that the I_2 values seen in Figure 4.18.a correspond to quantum efficiencies of 1.0 and 1.6 % at   -0.3 V and 0V vs. Ag/AgCl, respectively. The two values are close to that expected from the calculation of light absorption (see Table 4.3).

The influence of methanol concentration on the IMPS response of the anatase (101) surface has been investigated and is presented in Figure 4.19. It is clearly observed that the influence of methanol addition on the IMPS response is very small.

Figure 4.19. IMPS measured at the anatase TiO$_2$ single crystal (101) surface in aqueous 0.1M KCl with different methanol concentrations at -0.2V vs. Ag/AgCl.

Anatase thin-film: Figure 4.20.a and b displays the IMPS response measured at the anatase TiO$_2$ thin-film electrode in aqueous 0.1 M KCl solution before and after 1 vol% methanol addition at different potentials, respectively. It can be seen from Figure 4.20 that the I_2 value is highly increased with increasing the electrode potential from -0.3V to -0.2V vs. Ag/AgCl. At the same time, I_1 almost keeps constant. This means that the Gärtner flux significantly increases even due to this small potential change, but the constant value of I_1 indicates that almost all the additionally photogenerated holes reaching the electrode surface are eventually lost by recombination. A further increase of the potential leads to a significant reduction of the recombination as seen in the smaller semicircles and the decreasing k_{rec}/k_{tr} ratio. In this potential region I_1 increases, while I_2 slightly decreases. This behaviour can be attributed to the degradation of the thin-film electrode, i.e., the photoelectrochemical active area decreases in size.

Figure 4.20. IMPS measured at the anatase TiO$_2$ thin-film surface in aqueous 0.1M KCl (a) before and (b) after addition of 1 vol% methanol at different potentials vs. Ag/AgCl.

Similar to the anatase single crystal, a differential quantum efficiency of 1.0 under the given conditions (photon flux 5.14x10^{15} photons s^{-1}, 20% reflection, 1 cm^2 electrode area) would translate into a photocurrent amplitude of 5.27x10^{-5} A, so that the I_2 values seen in Figure 4.20.a correspond to quantum efficiencies of 1.0 % and 2.0 % at -0.3 V and 0V vs. Ag/AgCl,

respectively. The quantum efficiency values are nearly the same as the values calculated depending on the width of space charge layer (see Table 4.3).

The impact of the methanol concentration on the IMPS response measured at an anatase thin-film is shown in Figure 4.21. It has been noted from this figure that the I_2 values decrease and I_1 increases with increasing methanol concentration. This behaviour is similar to that observed at the rutile (100) electrodes. The tendency towards smaller semicircles translates into a decrease in k_{rec} relative to k_{tr}, indicating a much higher activity towards methanol photooxidation compared to the anatase single crystal electrode.

Figure 4.21. IMPS measured at the anatase TiO_2 thin-film surface in aqueous 0.1M KCl with different methanol concentrations at -0.2 V vs. Ag/AgCl.

4.3. Photocatalytic Activity

In the photocatalytic processes on TiO_2, active oxygen species such as hydroxyl radicals ($OH^\bullet$), superoxide anion radicals ($O_2^{\bullet-}$), and hydrogen peroxide (H_2O_2) are usually formed and regarded as the key oxidizing species [105, 113]. In general, it is assumed that photoinduced valance band holes oxidize hydroxide ions (or water molecules) adsorbed on the surface to produce highly oxidizing ($OH^\bullet$), which subsequently attack the pollutant molecules. The ($OH^\bullet$) radicals produced are often considered to be the major species responsible for the photocatalytic oxidation reaction. In this study, the photocatalytic activities of rutile TiO_2 (100), (001), and (110) surfaces as well as the anatase TiO_2 (101) surface have been assessed by terephthalic acid hydroxylation evincing the formation of $OH^\bullet$ radicals. Terephthalic acid reacts with $OH^\bullet$ radicals according to Eq. 3.2 yielding 2-hydroxyterephthalic acid. The latter exhibits a characteristic fluorescence at 425 nm when excited by 315 nm light. Figure 4.22.a, b, c, and d shows the change in the fluorescence spectra recorded for the terephthalic acid solution under UV illumination in the presence of rutile (100), (001), (110) surfaces and the anatase (101) surface, respectively. The increased fluorescence intensity of 2-hydroxyterephthalic acid at 425 nm upon illumination evinces the photocatalytic formation of $OH^\bullet$ radicals.
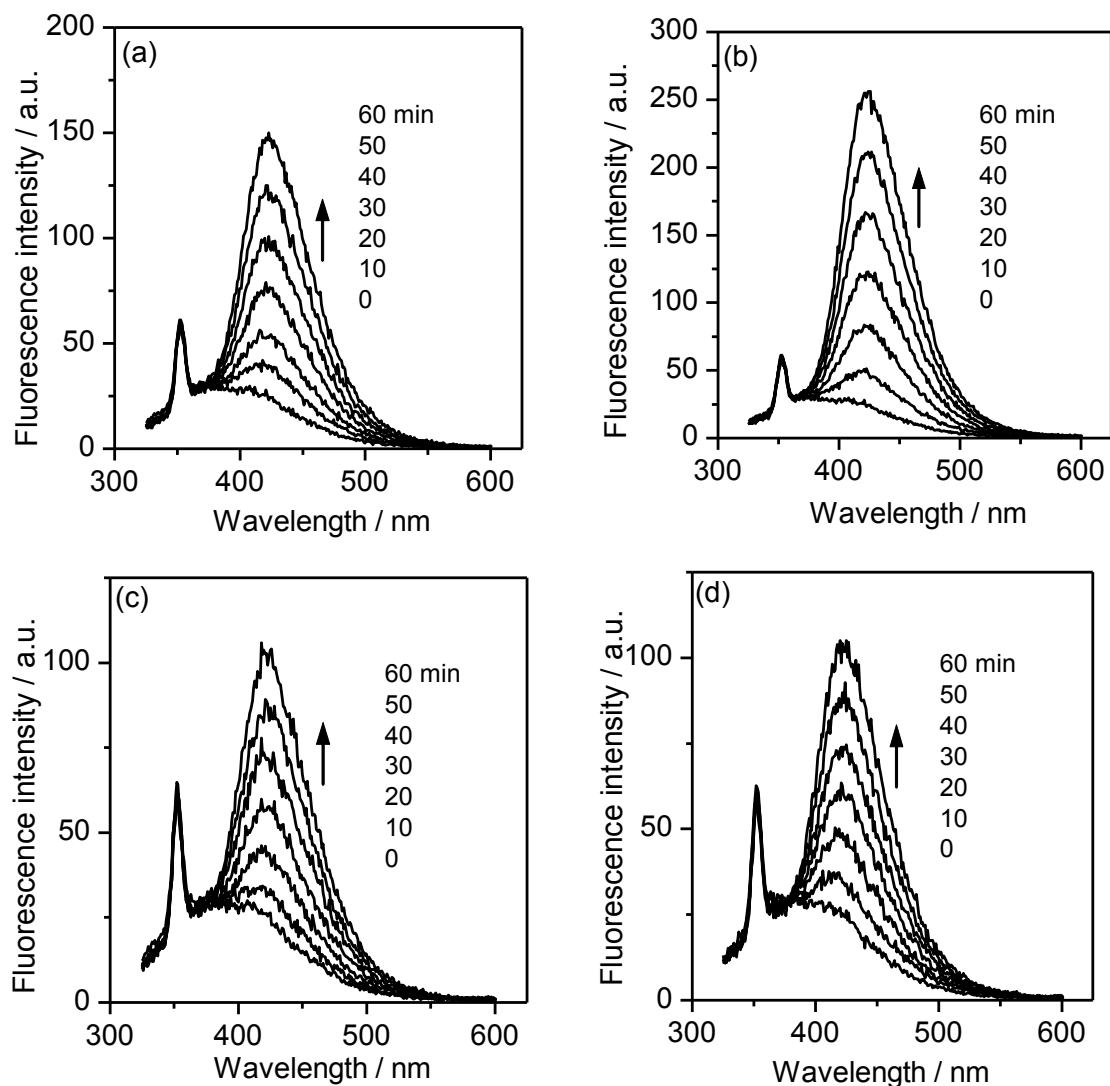
Figure 4.22. Fluorescence spectra of 4×10^{-4} M basic solution of terephthalic acid excited at 315 nm as function of illumination time of (a, b and c) rutile TiO_2 single crystal (100), (001) and (110) surfaces, respectively and (d) anatase TiO_2 single crystal (101) surface.

The photocatalytic activities of the rutile TiO_2 (100), (001), and (110) surfaces as well as of the anatase TiO_2 (101) surface have also been assessed by methanol photooxidation. Methanol is photooxdized by the photogenerated valance band hole either directly or through $OH^{\bullet}_s$ radicals leading to formaldehyde formation according to Eq. 2.7 to 13. Figure 4.23 shows the time course of formaldehyde formation on the different TiO_2 single-crystal surfaces. It is obvious from the results shown in Figure 4.23 that the anatase

(101) surface exhibits a higher photocatalytic activity than any of the investigated rutile surfaces.
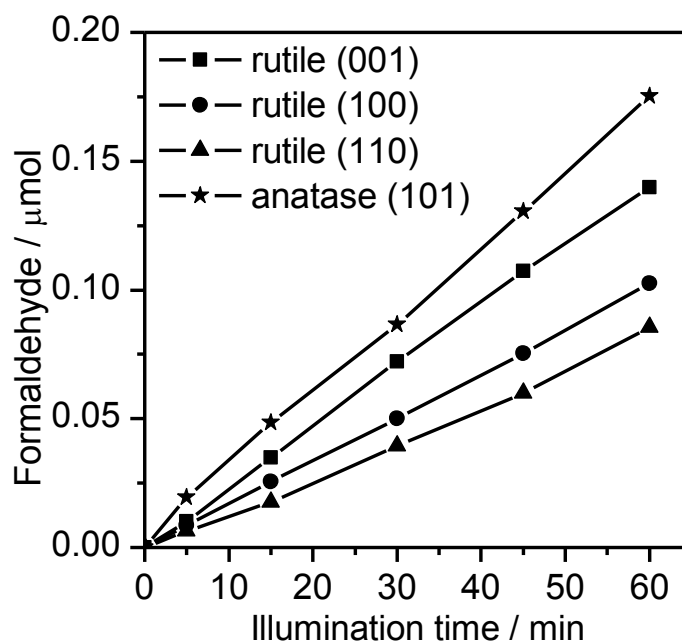
Figure 4.23. Photocatalytic methanol oxidation to formaldehyde on different TiO$_2$ single-crystal surfaces under 35 mW/cm^2 UV(A) illumination as a function of time; the illuminated area of rutile and anatase surfaces are 0.25 and 0.09 cm^2, respectively. Note: the amount of formaldehyde formed on the anatase surface has been normalized to a surface area of 0.25 cm^2.

5. Discussion

5.1. Photoelectrochemical Behaviour

5.1.1. Adaption of the IMPS Model for Multistep Electron Transfer to the Water/ Methanol System

Since the photoelectrochemical measurements have been carried out employing aqueous solutions, there is, in principle, a competition between the photooxidation of methanol and water at the TiO_2 surface. The details of these photooxidation processes are still not fully understood. For example, there is still a debate whether the photooxidations proceeds via mobile or immobile $OH^{\bullet}$ radicals. Since both types of species are potentially active towards the oxidation of organic compounds, they will be named hereafter as surface hydroxyl radicals ($OH^{\bullet}_s$) unless the difference in surface structure of the different investigated TiO_2 surface, i.e, rutile (100), (001), and (110) surfaces and anatase (101) and thin-film surfaces, will be discussed. Regardless of the nature of the photogenerated radical species, methanol has often been employed as a scavenger for photogenerated radicals in order to determine the quantum yield or the photonic efficiency of radical generation at the TiO_2 surface [75-77]. The photooxidation of methanol and/or water is known to proceed through multi electron transfer processes. For instance, both water and methanol lose two electrons to be photooxidised to peroxide and formaldehyde, respectively.

In order to investigate the nature of the intermediates involved in the photooxidation of water and methanol at the different investigated TiO_2 electrodes, the IMPS response measured at different electrode potential in the presence as well as in the absence of methanol (see section 4.2.2.2) have been analysed employing a phenomenological IMPS model [98] to describe the multistep electron transfer reactions that also considers the involvement of

immobile (Case I) and mobile (Case II) intermediates (see Theory section 2.4.2 for further details). According to this model, the general mechanisms considered for water oxidation for the two cases can be described by the following elementary steps:

$$OH^- / (H_2O - H^+) + h^+ \xrightarrow{k_1} OH_s^\bullet \qquad\qquad\qquad \text{(Eq. 5.1.a)}$$

$$OH_s^\bullet + h^+ \xrightarrow{k_2} 1/2\, O_2 + H^+ \qquad \text{(Case I)} \qquad \text{(Eq. 5.1.b)}$$

$$OH_s^\bullet + H^+ + e^- \xrightarrow{k_3} H_2O \qquad\qquad\qquad \text{(Eq. 5.1.c)}$$

$$OH_s^\bullet + OH_s^\bullet \xrightarrow{k_4} OH^- + 1/2 O_2 + H^+ \qquad \text{(Case II)} \qquad \text{(Eq. 5.1.d)}$$
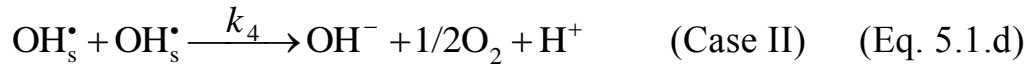
The OH^- anions or water molecules at the TiO_2 surface are the hole trapping sites and the surface hydroxyl radicals $OH_s^\bullet$ are the intermediates, which are either mobile and can therefore react with another $OH_s^\bullet$ (Eq. 5.1.d, Case II) or they are immobile and can therefore react by catching a hole (Eq. 5.1.b, Case I).

In the presence of methanol in the electrolyte, another reaction with a fifth rate constant needs to be added to the model, taking into account the reaction between methanol and $OH_s^\bullet$:

$$OH_s^\bullet + CH_3OH \xrightarrow{k_5} {}^\bullet CH_2OH + H_2O \qquad\qquad \text{(Eq. 5.1.e)}$$
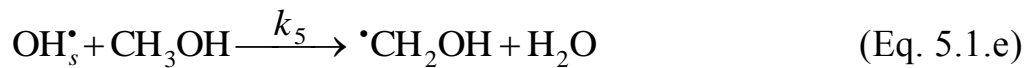
This reaction opens a new charge-transfer route for the intermediate, so that the charge transfer from the intermediate would proceed with a rate constant of $k_2 + k_5$ (instead of k_2) in Case I and with a rate constant of $k_4 + k_5$ (instead of k_4) in Case II. Based on the model of Peter et al.[98], the following expressions for k_{tr} and k_{rec} as functions of k_1 to k_5 are obtained:

Case I:

$$k_{tr}^{I} = \frac{2(k_2 + k_5)(k_1 p_0 + k_3 X_0)}{k_1 + (k_2 + k_5)(p_0 + X_0) + k_3} \qquad \text{(Eq. 5.2.a)}$$

$$k_{rec}^{I} = \frac{k_3(k_1 - (k_2 + k_5)X_0)}{k_1 + (k_2 + k_5)(p_0 + X_0) + k_3} \qquad \text{(Eq. 5.2.b)}$$

Case II:

$$k_{tr}^{II} = \frac{8k_1(k_4 + k_5)X_0}{k_1 + 8(k_4 + k_5)X_0 + k_3} \qquad \text{(Eq. 5.2.c)}$$

$$k_{rec}^{II} = \frac{k_1 k_3}{k_1 + 8(k_4 + k_5)X_0 + k_3} \qquad \text{(Eq. 5.2.d)}$$

5.1.2. Analysis of IMPS Measurements

The analysis of the IMPS results has been performed by fitting all the IMPS plots shown in section 4.2.2.2 according to Eq. 2.14 presented in the Theory section 2.4.1. The fitting has been done according to the model for the full experimental IMPS response (including the part in the positive/negative quadrant measured at high frequencies). The fitted values were k_{tr}, k_{rec} and C_{sc}, while experimental and calculated values were used for g_1, R, and C. For calculating the Gärtner flux g_1, the photon flux has been determined by measuring the light intensity using ferrioxlate actinometery. From the resulting value, g_1 has been calculated separately for each potential based on the width of the space charge layer and the fraction of photons absorbed within it (see Table 4.3). For potentials between -0.3 V to 0 V vs. Ag/AgCl, the g_1 values are found to be between 7.90×10^{-7} and 9.22×10^{-7} A cm^{-2} for rutile (100), 1.45×10^{-6} to 1.71×10^{-6} A cm^{-2} for rutile (001), 3.42×10^{-6} to 3.95×10^{-6} A cm^{-2} for rutile (110), 1.42×10^{-7} A cm^{-2} to 1.90×10^{-7} A cm^{-2} for anatase (101) and 1.05×10^{-6} A cm^{-2} to 1.58×10^{-6} A cm^{-2} for anatase thin-film.

The g_1 has been kept close to these ranges during the fitting process. R and C values have been extracted from impedance measurements. The R values estimated at high frequency and RC values for rutile, anatase (101) and thin-film are 0.0002, 0.06 and 0.007 s^{-1}, respectively. Figure 5.1. shows an example of the fitting of the IMPS response (data point) and the fitted curve (solid line).
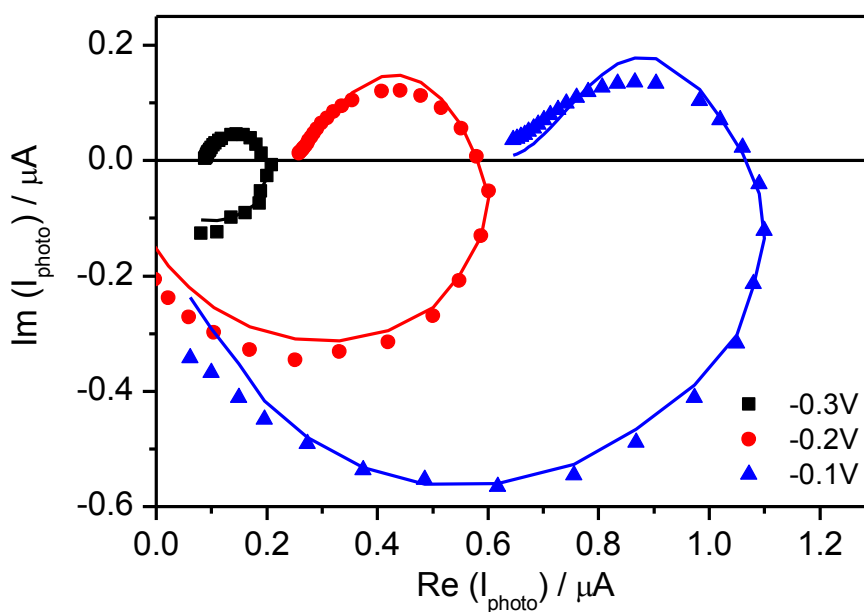
Figure 5.1. Experimental IMPS response measured at the rutile (100) surface in aqueous 0.1 M KCl with a methanol concentration of 1.0 vol % and fitted data (solid line). At different applied potential vs. Ag/AgCl.

5.1.3. Influence of Electrode Potential

In the simplest case of a one-electron charge transfer process at an ideal surface, the electrode potential is expected to influence the rate of recombination and thereby k_{rec} due to the changing concentration of majority carriers at the electrode surface, while k_{tr} should not be influenced. In the present study, however, changes in the potential clearly lead to changes in both k_{rec} and k_{tr}. This is consistent with the multi-electron charge transfer model presented in the Theory section 2.4.2, since based upon this model k_{rec} and k_{tr} are phenomenological rate parameters, which are both functions of the rate constants associated with the elementary steps of both, the recombination and the charge transfer processes. In the following, the values of k_{rec} and k_{tr} extracted from the IMPS response by the fitting are plotted and compared with the potential dependences expected from theory for Case I and Case II according to the IMPS model.

Influence of electrode potential on k_{rec}: Figure 5.2 shows the influence of the potential on the k_{rec} values for the rutile TiO_2 single crystal (100), (001) and (110) surface electrodes. It is clearly seen that k_{rec} decreases with increasing potential for all the investigated rutile surfaces in aqueous 0.1 M KCl in the presence as well as in the absence of 1 vol% methanol, which is expected for both Case I and Case II.

Based on the approximation that $k_{rec} \approx k_3$ and the fits according to Eq. 2.19 with E_{FB} values taken from the Mott-Schottky plots (see 4.2.2.1), the calculations yielded the β and k_3^0 values tabulated in Table 5.1. Note that the fits were made for the k_{tr} values measured in the absence of methanol (solid symbols in Figure 5.2.b), omitting the value measured at -0.3 V vs. Ag/AgCl in case of the (001) surface, since this value clearly deviates from the linear behaviour and is less reliable due to the very small photocurrent at this

potential. The k_{rec} values of the rutile (001) surface are found to be almost the same before and after the addition of methanol, while they become considerably lower after methanol addition at the other two surfaces. This again indicates that the addition of methanol leads to a reduction in the charge carrier recombination rate at the rutile (100) and (110) surfaces, while there is not much influence on the recombination rate on the rutile (001) surface.
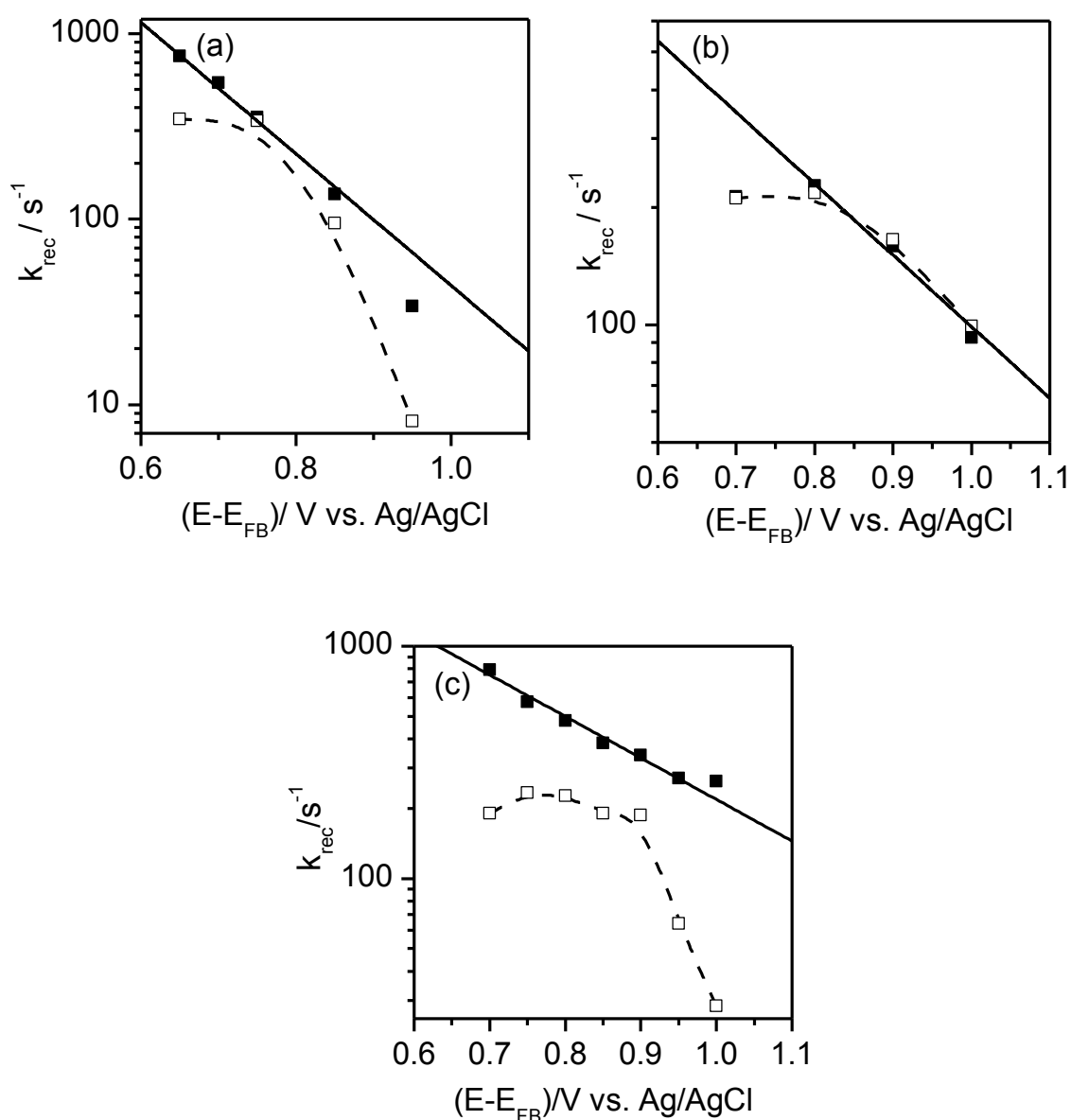
Figure 5.2. Potential dependence of k_{rec} for rutile TiO_2 (a) (100), (b) (001) and (c) (110) surfaces measured with 0 vol% (solid symbols) and 1 vol% (open symbols) methanol in the 0.1 M KCl electrolyte. Solid lines are fits to Eq. 2.19. Dashed lines are for illustration purposes only.

The same kind of analysis has also been carried out for the anatase TiO_2 single crystal (101) and the anatase thin-film electrodes, with k_{rec} values plotted vs. potential in Figures 5.3.a and b, respectively. Decreasing trends are also seen in this case, except for the anatase thin-film electrode after addition of methanol, where k_{rec} stays almost constant. Comparison of the β and k_3^0 values for rutile and anatase electrodes (Table 5.1) reveals that both β and k_3^0 values are the lowest in case of the anatase (101) surface, indicating a much higher surface excess charge that can be explained by the population of interband surface states and a much slower recombination rate at this surface [108]. The contrast is seen in case of anatase thin-film (see Table 5.1), which shows the fastest recombination of all surfaces. Furthermore, the k_{rec} values for anatase, especially in case of the anatase (101) electrode, are higher in the presence of 1 vol% methanol, which is opposite to the behaviour in case of the rutile electrodes.
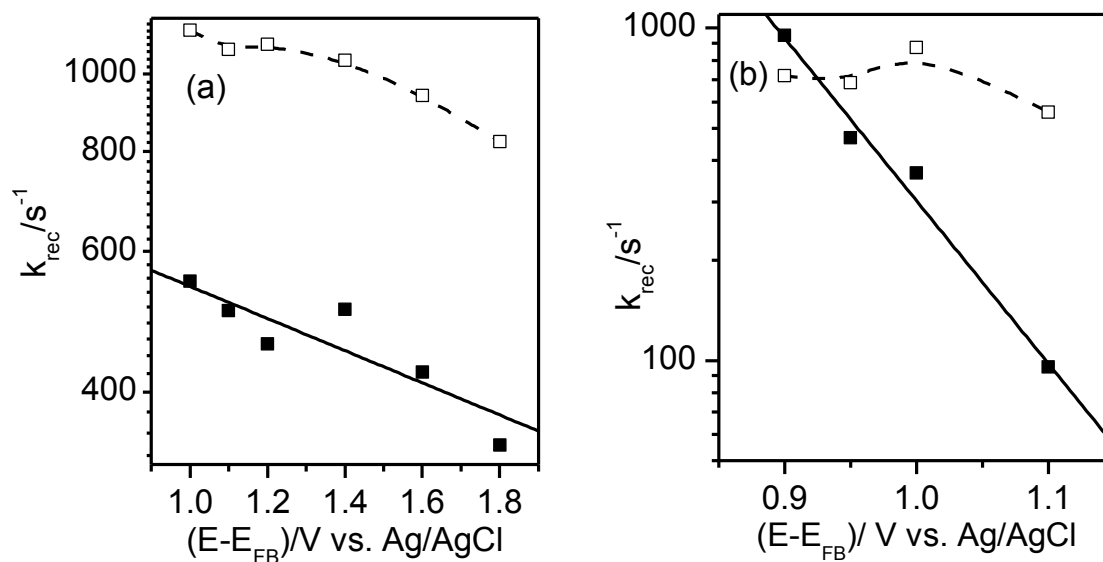
Figure 5.3. Potential dependence of k_{rec} for anatase TiO_2 (a) single crystal (101) and (b) thin-film surfaces measured with 0 vol% (solid symbols) and 1 vol% (open symbols) methanol in the 0.1 M KCl electrolyte. Solid lines are fits to Eq. 2.19. Dashed lines are for illustration purposes only.

Table 5.1. k_3^0, β, k_4 and k_5 values calculated from the fitting for the different investigated TiO_2 surfaces.

Surface	β	k_3^0/s^{-1}	k_4/cm^2s^{-1}	k_5'/cm^2s^{-1}
Rutile (100)	0.21 ± 0.1	$(1.55\pm0.6)10^5$	$(9.9\pm0.5)10^{-10}$	$(8\pm0.5)10^{-8}$
Rutile (001)	0.11 ± 0.02	$(6.7\pm3.1)10^3$	$(4.8\pm0.1)10^{-9}$	$(8\pm0.6)10^{-9}$
Rutile (110)	0.1 ± 0.01	$(1.34\pm0.3)10^4$	$(2.3\pm0.04)10^{-9}$	$(8.5\pm0.2)10^{-8}$
Anatase (101)	0.01 ± 0.003	$(8.62\pm1.4)10^2$	$(3\pm0.3)10^{-8}$	$(4.6\pm0.6)10^{-9}$
Anatase (thin-film)	0.29 ± 0.01	$(2.39\pm0.1)10^7$	$(4.5\pm0.1)10^{-8}$	$(9\pm0.7)10^{-8}$

Influence of electrode potential on k_{tr}: By investigating the influence of the electrode potential on the k_{tr} values, it was found that for the rutile TiO_2 (001) and the anatase TiO_2 (101) faces, k_{tr} increases towards more positive electrode potentials (increased band bending) in the absence of methanol as well as in the presence of 1 vol% methanol as shown Figures 5.4.b and 5.5.a, respectively. This behaviour is typical for Case II, indicating the involvement of mobile $OH_s^{\bullet}$ radicals as intermediates in the processes occuring at these two surfaces. The expected saturation behaviour towards positive potentials is not very distinct under the employed conditions, indicating that the concentration of the $OH_s^{\bullet}$ radicals is not yet saturated at the surface under the employed low light intensity [98]. In the presence of methanol, the k_{tr} values are slightly increased due to k_5 becoming > 0 in Eq. 5.2.c (see section 5.1.1).

For the rutile TiO_2 (100) and (110) surfaces and the anatase thin-film surface, the increasing trend of the k_{tr} values towards more positive electrode potentials is only observed in the absence of methanol, this time with a clear saturation behaviour in case of the rutile (100) electrode, while a distinct decreasing trend typical for Case I is seen in the presence of 1 vol% methanol as shown in Figures 5.4.a and c and 5.5.b, respectively. This indicates that water oxidation at these surfaces occurs via the reaction of two mobile $OH_s^{\bullet}$

radicals like in the case of the other two surfaces, while methanol oxidation involves surface trapped holes on these electrodes.
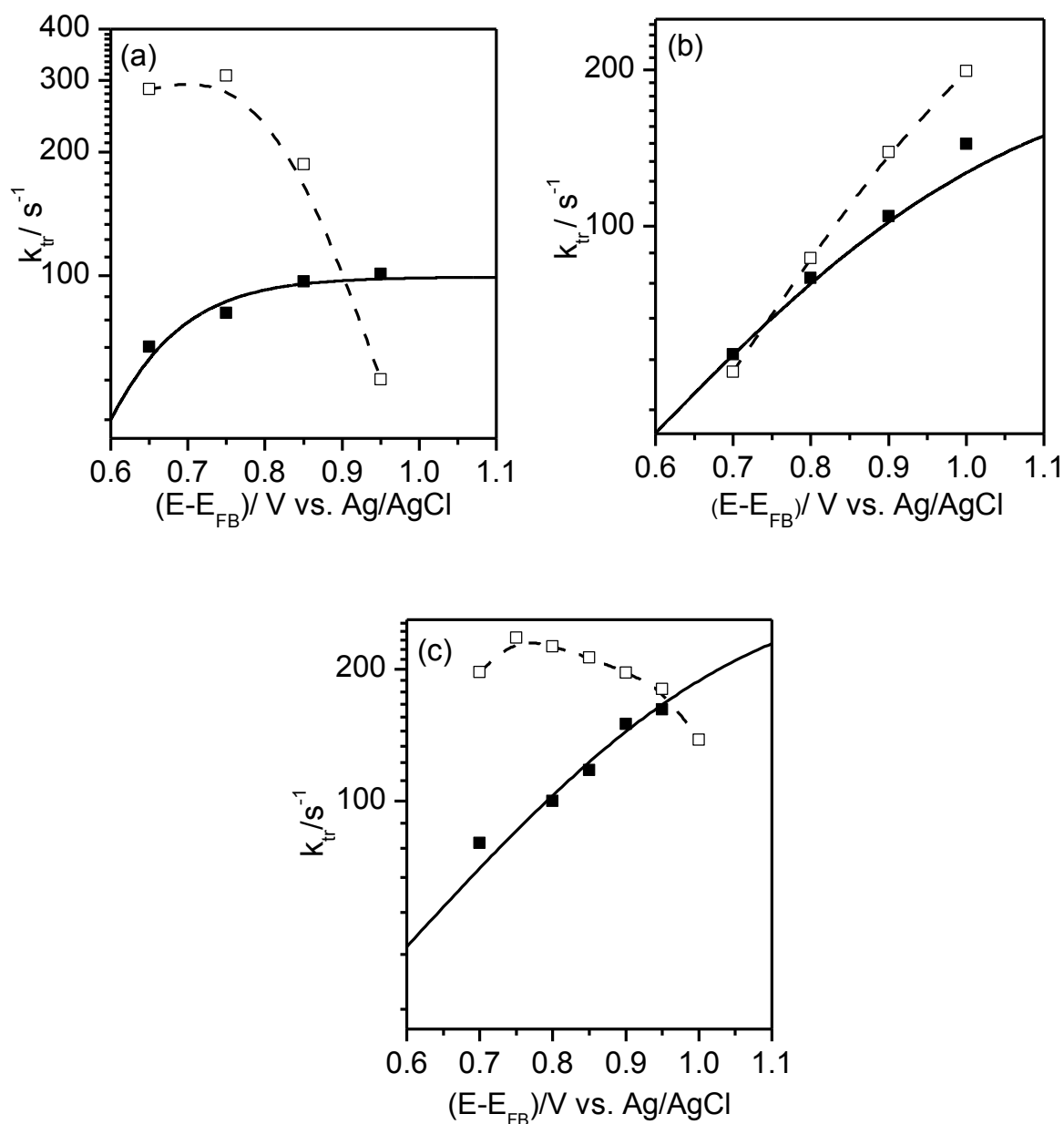
Figure 5.4. Potential dependence of k_{tr} for rutile TiO_2 single crystal (a) (100), (b) (001), and (c) (110) surfaces measured with 0 vol% (solid symbols) and 1 vol% (open symbols) methanol in the 0.1 M KCl electrolyte. Solid lines are fits to Eq. 5.2.c with X_0 and k_3 replaced by Eq. 2.38 and 19, respectively, and $k_5 = 0$. Dashed lines are for illustration purposes only.
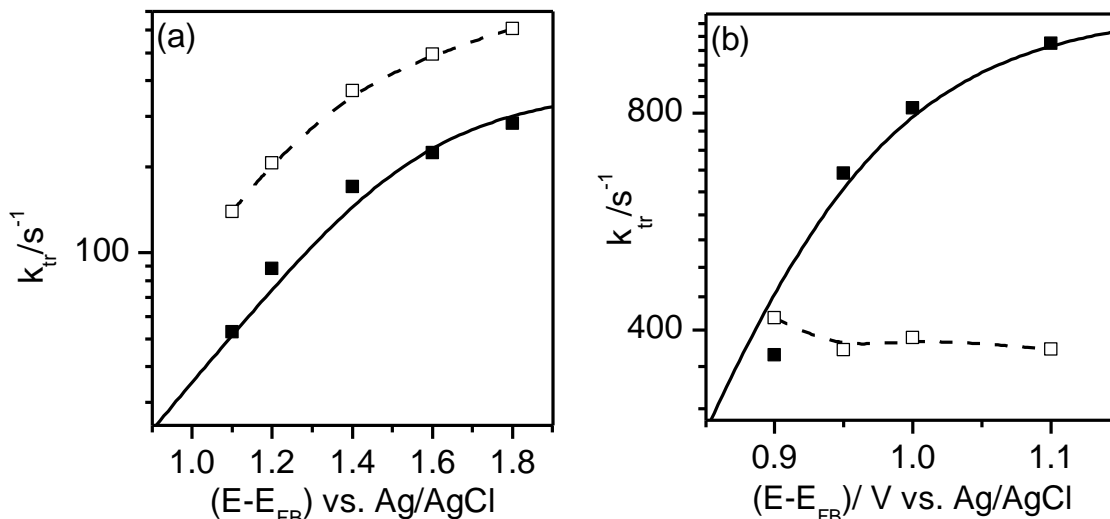
Figure 5.5. Potential dependence of k_{tr} for the anatase TiO_2 (a) single crystal (101) and (b) thin-film surfaces measured with 0 vol% (solid symbols) and 1 vol% (open symbols) methanol in the 0.1 M KCl electrolyte. Solid lines are fits to Eq. 5.2.c with X_0 and k_3 replaced by Eq. 2.38 and 19, respectively, and $k_5 = 0$. Dashed lines are for illustration purposes only.

While the influence of the methanol concentration is analyzed in more detail in the subsequent section (see section 5.1.4), the k_{tr} values measured in the absence of methanol (solid symbols in Figure 5.4 and 5) have been used to determine k_4. For this purpose, these values were fitted to Eq. 5.2.c by replacing X_0 by Eq. 2.38, setting $k_5 = 0$ and considering a potential dependence of k_3 according to Eq. 2.19 (Theory section 2.4.2) with k_3^0 and β fixed to the values determined from Figures 5.2 and 5.3. The resulting k_4 values are calculated and collected in Table 5.1. A comparison of these values shows that the coupling of $OH^\bullet_s$ radicals is about one order of magnitude faster on the anatase surfaces compared to the rutile surfaces.

5.1.4. Influence of the Methanol Concentration

Influence of the methanol concentration on k_{tr}: Figures 5.6 and 5.7 show the methanol concentration dependence of k_{tr} for rutile and anatase TiO$_2$ surfaces, respectively. It is obvious from Figure 5.6 that the increase of k_{tr} with increasing methanol concentration occurs at all rutile surfaces. However, there is faster saturation in case of the (100) surface and especially the (110) surface, indicating a stronger interaction of methanol with these two surfaces.
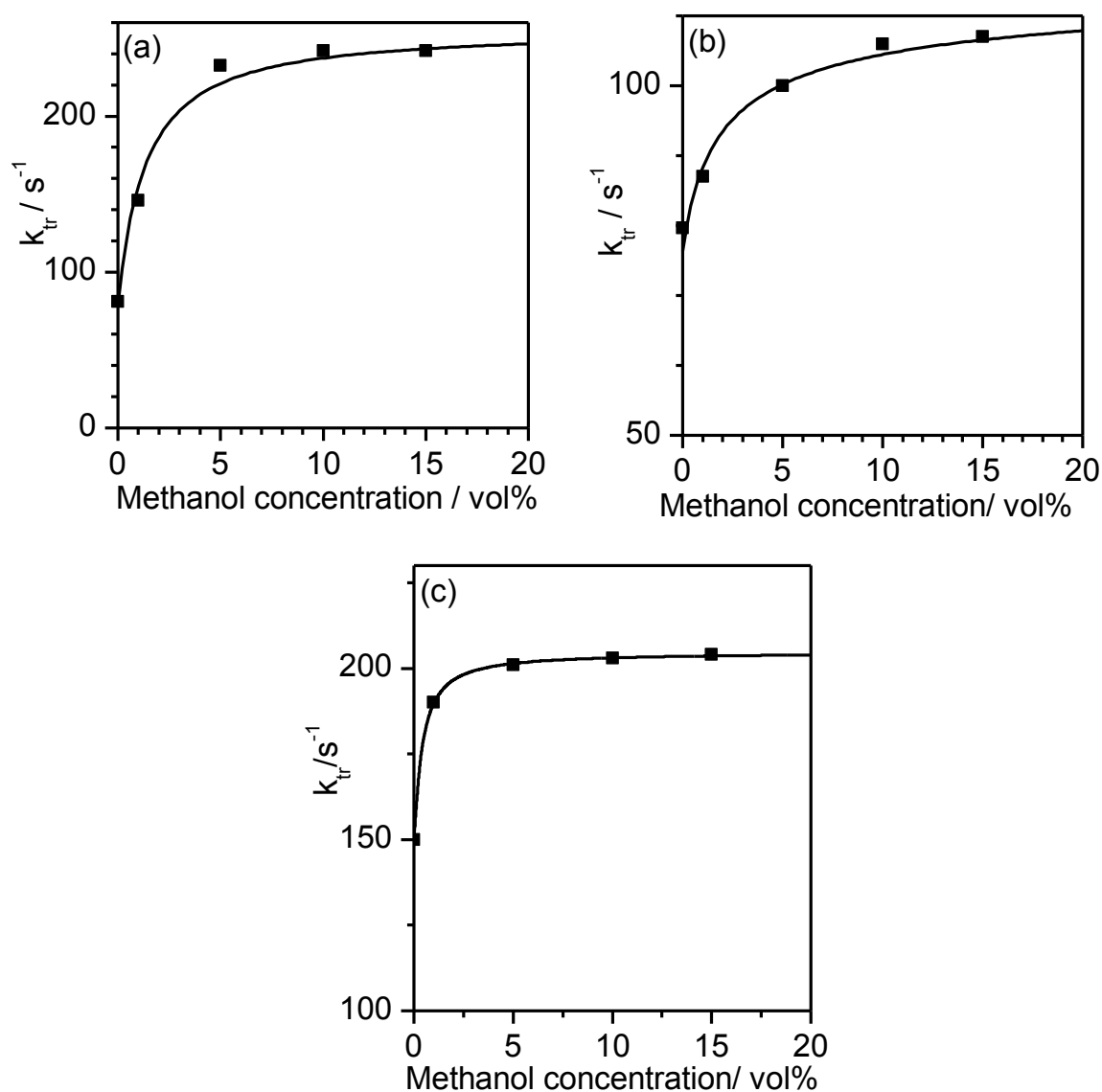
Figure 5.6. Methanol concentration dependence of k_{tr} for: (a) rutile (100), (b) rutile (001), and (c) rutile (110) surfaces at -0.2 V vs. Ag/AgCl, lines correspond to fits to Eq. 5.2.c (b) and to Eq. 5.2.a (a,c), respectively.

Figure 5.7.a and b show the methanol concentration dependence of k_{tr} at the anatase TiO$_2$ (101) and the thin-film surfaces, respectively. Figure 5.7.a illustrates that the increase in k_{tr} with increasing methanol concentration at the anatase TiO$_2$ (101) surface is slow and the saturation level is still not reached at 20 vol%, whereas for the anatase thin-film surface shown in Figure 5.7.b, k_{tr} increases much more steeply and the saturation is clearly visible.
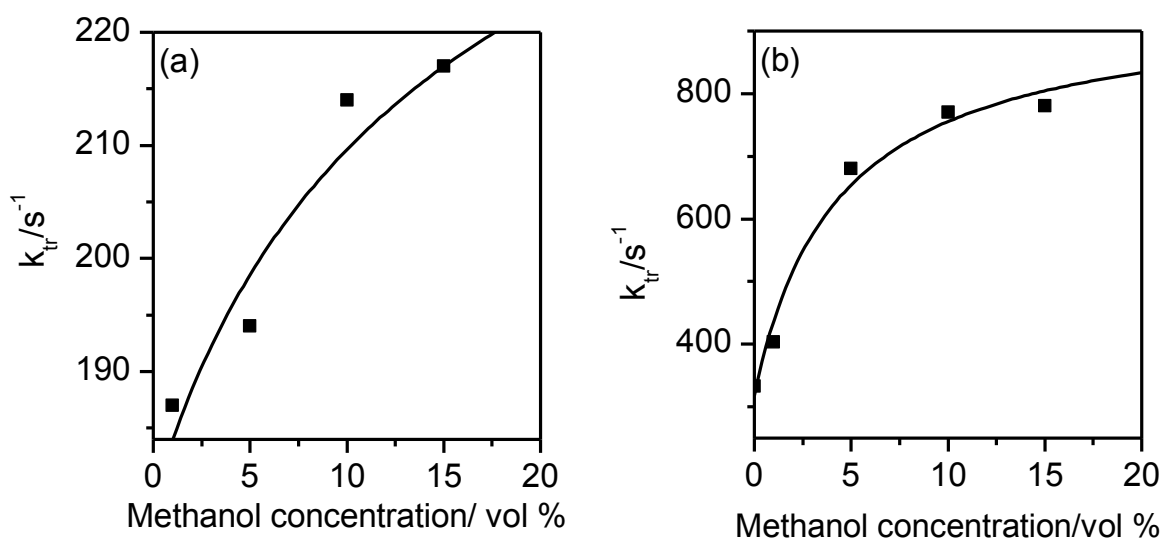
Figure 5.7. Methanol concentration dependence of k_{tr} for the anatase TiO$_2$ (a) single crystal (101) and the (b) thin-film surfaces at -0.2 V vs. Ag/AgCl, lines correspond to fits to Eq. 5.2.c (a) and to Eq. 5.2.a (b), respectively.

The saturation behaviour of k_{tr} with increasing methanol concentration, which is observed at a more or less pronounced extent for all surfaces, is actually expected with increasing k_5 (reflecting the increasing methanol concentration) according to Eq. 5.2.a (Case I) and c (Case II). Depending on the results of the potential dependence in the forgoing section, the fitting of the k_{tr} values in Figures 5.6 and 5.7 has been made according to Eq. 5.2.c (Case II) in case of the rutile TiO$_2$ (001) and the anatase TiO$_2$ (101) faces and according to Eq. 5.2.a (Case I) in case of the rutile TiO$_2$ (100) and (110) surfaces and the anatase thin-film faces after replacing k_5 by k_5'[MeOH] and X_0 by Eq. 2.38 and 22, respectively. The k_5' values obtained from this fitting

are collected in Table 5.1. Comparison of the k_5' values for all the surfaces reveals a clearly faster (by a factor of 10) charge transfer to methanol from immobile $OH_s^{\bullet}$ radicals on the rutile (100) and (110) and the anatase thin-film surfaces as compared to the charge transfer from mobile $OH_s^{\bullet}$ radicals on the (001) and anatase (101) faces.

Influence of the methanol concentration on k_{rec}: The methanol concentration dependences of k_{rec} have been investigated for the rutile and the anatase surfaces as well, as shown in Figures 5.8 and 5.9, respectively.
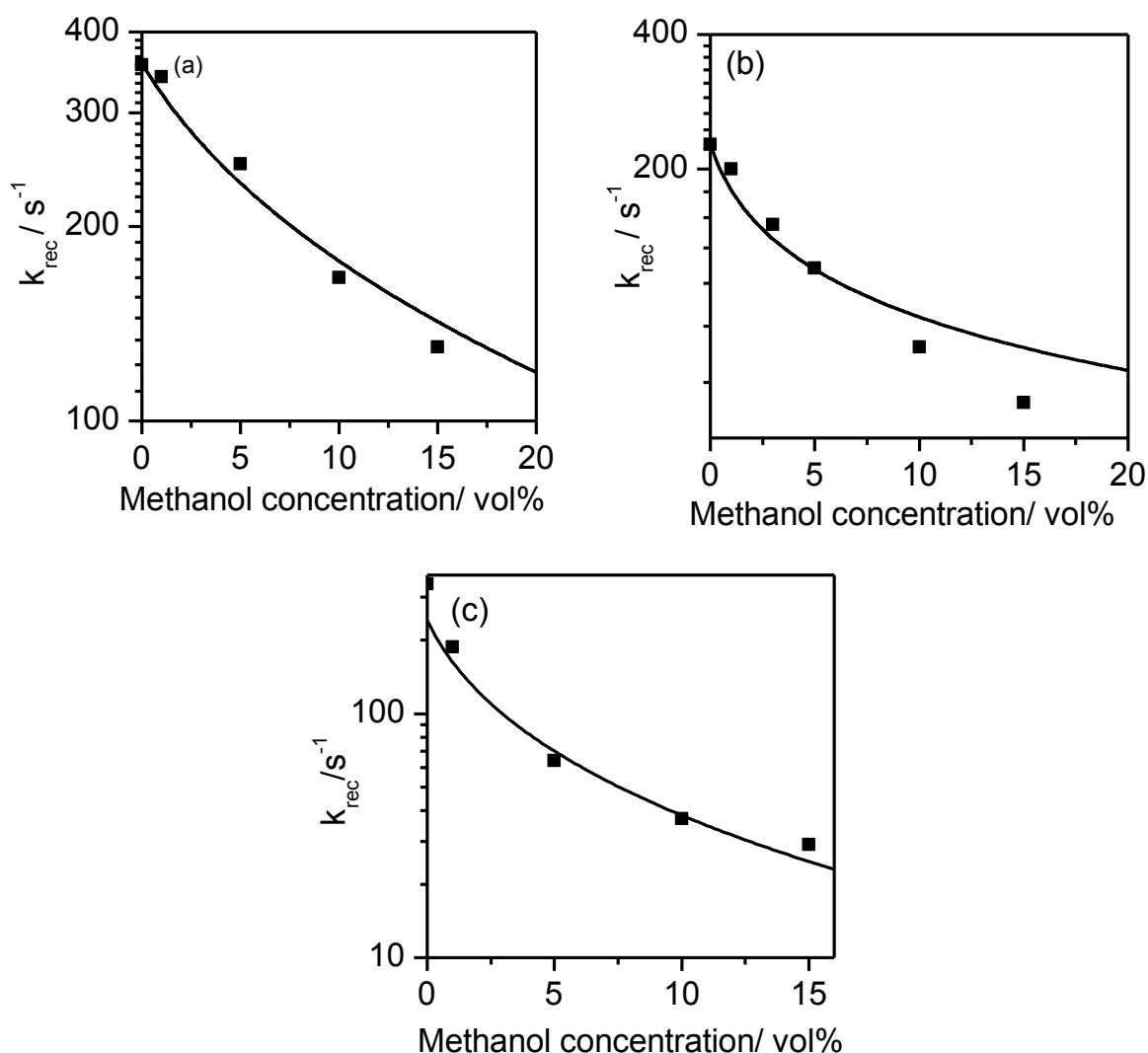
Figure 5.8. Methanol concentration dependence of k_{rec} for (a) rutile (100), (b) rutile (001), and (c) rutile (110) surfaces at -0.2 V vs. Ag/AgCl. Lines are simulations corresponding to Eq. 5.2.d (b) and Eq. 5.2.b (a, c), respectively.
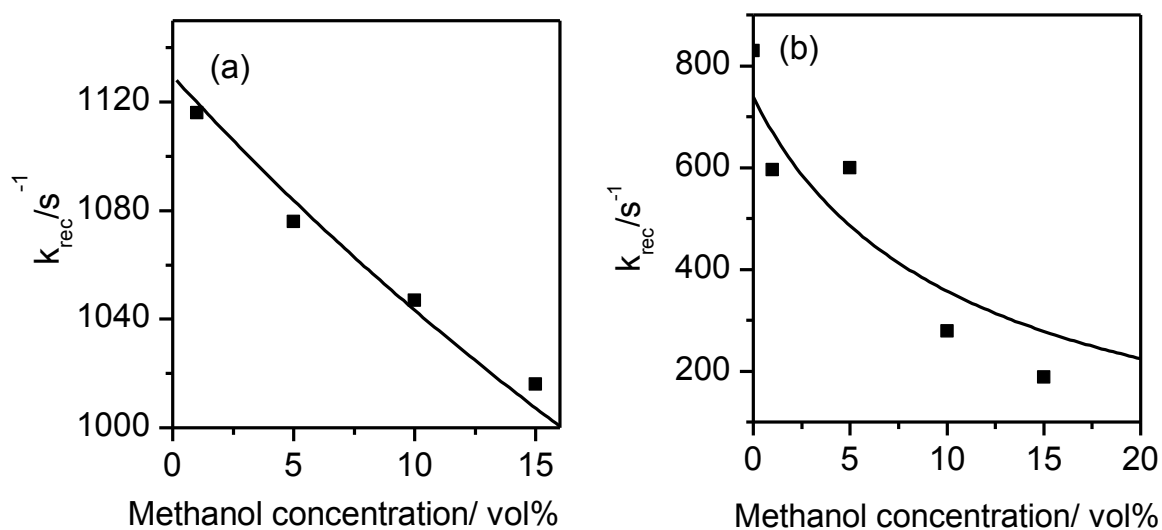
Figure 5.9. Methanol concentration dependence of k_{rec} for (a) anatase single crystal (101) and (b) thin-film surfaces at -0.2 V vs. Ag/AgCl. Lines are simulations corresponding to Eq. 5.2.d (a) and Eq. 5.2.b (b), respectively.

All the faces exhibit significantly higher k_{rec} values at small concentrations of methanol, followed by a decrease in k_{rec} with increasing methanol concentration. This decrease with increasing k_5 value is expected according to Eq. 5.2.b and d. Simulation of the results according to Eq. 5.2.b and d with the same substitutions for X_0 and k_5 as mentioned above (in the k_{tr} dependence) yielded reasonable fits using the same k values as obtained from the foregoing fits. This can be taken as clear evidence that the chosen model is consistent with the observed concentration dependences of both k_{tr} and k_{rec}.

5.1.5. Correlations between Photooxidation Mechanisms and Surface Structures

Like most partially ionic metal oxides, TiO_2 also exhibits two types of intrinsic ionic surface states associated with unsaturated titanium and oxygen terminal ions, respectively, as shown in Figure 5.10.a [26, 73]. These surface states are able to electronically interact with electrolyte species (water molecules, hydroxyl ions, protons and/or dissolved organic compounds). The 3d orbitals of 5-fold coordinated terminal titanium cations (Ti_t) behave like Lewis acid sites able to form strong bonds with the lone electron pairs of water species while the 2p orbitals of 2-fold coordinated terminal oxygen ions, known as bridging oxygen ($>OH^{2-}_{br}$) species, behave like Lewis base sites able to share a pair of valence band electrons with the otherwise empty 1s orbitals of H^+ cations of the aqueous electrolyte [62]. Assuming dissociative adsorption of water, two types of hydroxyl groups are thus present at the TiO_2 surface: (a) OH^- adsorbed hydroxyl groups 1-fold coordinated to Ti_t terminal titanium atoms, (b) terminal hydroxyl ions resulting from the protonation of terminal, 2-fold coordinated bridging oxygen ions ($>OH^-_{br}$) [62].

However, there is still a controversy in the literature concerning the nature of the $OH^•_s$ radical species initially formed on the TiO_2 surface upon illumination. While it is often assumed that the photogenerated free holes in the valence band of TiO_2 are trapped by adsorbed water species to produce adsorbed $OH^•_s$ radicals, it was recently reported that this process should be kinetically and thermodynamically hindered, because the O:2p energy level of the adsorbed water molecules is far below the upper valance band edge of TiO_2 as comfirmed by the analysis of the electronic structure of adsorbed water employing metastable impact electron spectroscopy and ultraviolet photoemission spectroscopy [26, 58, 62, 64, 65]. Therefore, the

photogenerated holes should be preferrably trapped at bridging 2-fold coordinated terminal oxygen ions ($>OH^-_{br}$), leading to the formation of surface $>OH^\bullet_{br}$ radicals [26, 62] as shown in Figure 5.10.b.
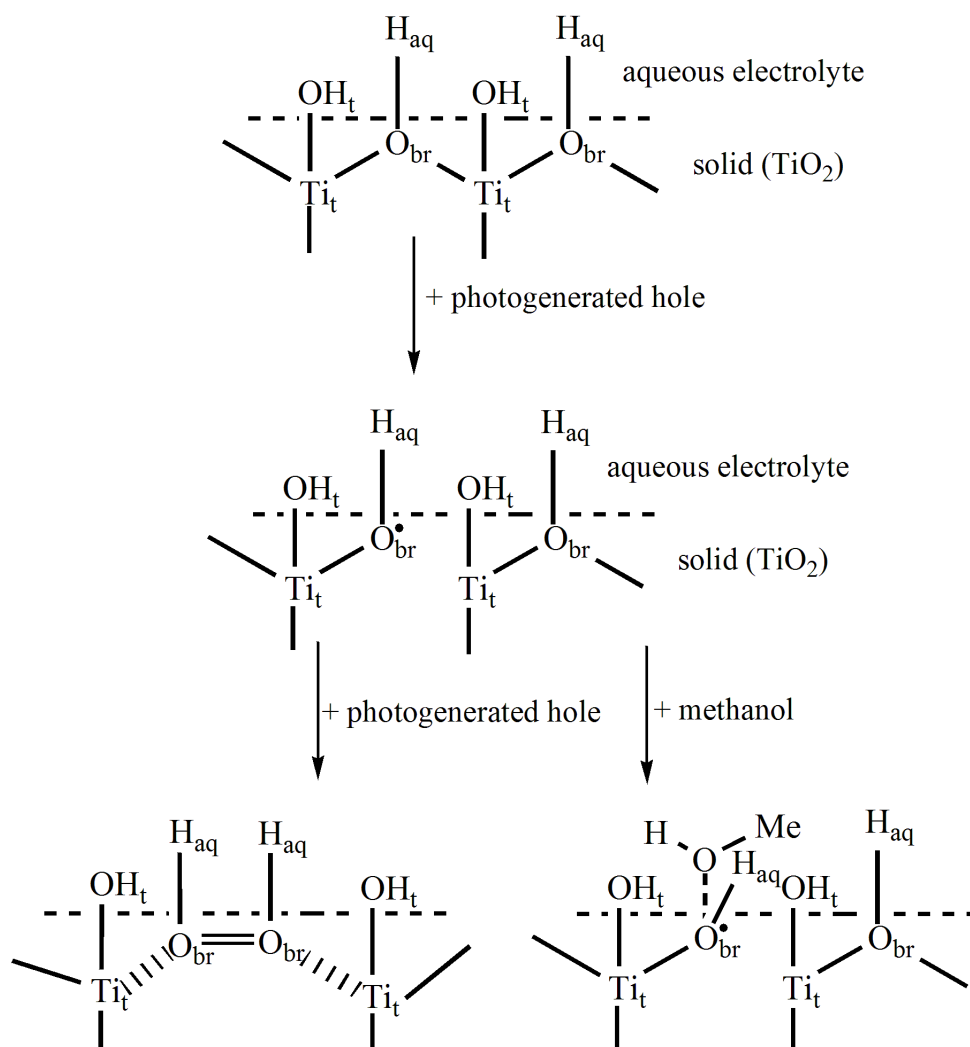
Figure 5.10. Schematic illustration of (a) the two types of surface hydroxyl groups resulting from the dissociative adsorption of water on the TiO_2 surface [62], (b) the preferred trapping position of the photogenerated hole, and (c, d) the different reaction pathways of the photogenerated trapped hole.

In the absence of other oxidizable species such as methanol, two of the photogenerated surface $>OH^\bullet_{br}$ radicals react with each other on all surfaces as shown in Figure 5.10.c (Case II). In the presence of methanol, different

trends have been observed for the different surfaces. The rutile (001) and the anatase (101) surfaces still behave like in the presence of water (Case II), while the rutile (100) and (110) surfaces and the anatase thin-film surface behave according to Case I, i.e., no reaction between the two hydroxyl radical intermediates occurs. This difference can be explained considering that the photogenerated $>OH^{\bullet}_{br}$ radicals on the rutile (100) and (110) surfaces and the anatase thin-film surface are more reactive towards methanol oxidation than towards the reaction with another $>OH^{\bullet}_{br}$ radical. This consideration is in agreement with the finding that the $k_5{'}$ values (see Table 5.1), which are representing the charge transfer to methanol, are about 10 times higher on the rutile (100) and (110) surfaces and on the anatase thin-film surface than on the rutile (001) and the anatase (101) surfaces.

Comparing the rutile surfaces with each other, it is also found that the k_4 values of the (100) and (110) surfaces are five times and two times smaller, respectively than that of the (001) surface. This observation appears to be reasonable considering the structure of these surfaces: The distance between two bridging oxygen anions occupying adjacent positions is 2.54 Å at the (001) face, i.e., 0.42 Å smaller than the distance of 2.96 Å at the (100) and (110) faces [26], thus the reaction of two adjacent $>OH^{\bullet}_{br}$ radicals is more likely and therefore faster on the (001) surface than on the TiO_2 (100) and (110) surfaces. The rutile (001) surface can be considered as being non-polar as previously reported [54, 114], while the rutile (100) and (110) surfaces are polar. Thus, the interaction of methanol with its polar OH group and the rutile (100) and (110) surfaces may be preferred in comparison to the (001) surface. Consequently, surface $>OH^{\bullet}_{br}$ radicals on the rutile (100) and (110) surfaces will preferrably react with methanol (Figure 5.10.d), leading to an overall decrease of their accumulated surface concentration and thereby lowering the probability of the reaction of two $>OH^{\bullet}_{br}$ radicals with one another. In fact, it

has been reported that these surface trapped holes at the 2-fold coordinated terminal oxygen ions, >$OH^{\bullet}_{br}$, react mainly with dissolved species that do not interact strongly with the semiconductor surface, (i.e., in the absence of specific adsorption) [68, 115]. This is consistent with our observation that the presence of methanol does not lead to a shift in the flatband potential of TiO_2, i.e., that methanol does not adsorb strongly on the electrode surface. On the rutile (001) surface, reaction between two >$OH^{\bullet}_{br}$ radicals is faster and interaction with methanol is weaker, hence, the processes at the electrode surface are dominated by the coupling of two >$OH^{\bullet}_{br}$ radicals (Figure 5.10.c) and therefore by the photooxidation of water even in the presence of methanol.

By comparing the k_4 of the anatase single crystal (101) surface with that of the anatase thin-film, it was found that k_4 of the later is 1.5 time higher than that of the former. This observation can be attributed to the fact that the anatase thin-film is polycrystalline. Both, the anatase single crystal (101) and the thin-film exhibit higher k_4 values than the rutile surfaces, i.e., the k_4 values are about one order of magnitude higher, despite the fact that the distance between two bridging oxygen anions occupying adjacent positions in anatase (3.04 Å) is higher than that in rutile [107]. This can be explained depending upon the surface structure of anatase, which has a saw tooth profile that might facilitate the coupling of two adjacent >$OH^{\bullet}_{br}$ radicals (see Theory section 2.3.2).

5.2. Photocatalytic Activity

In the previous section, the rate constants of charge carrier transfer and recombination on the TiO_2 single crystal electrodes have been investigated using IMPS studies in the presence as well as in the absence of methanol from aqueous 0.1M KCl solutions. These measurements have been performed employing a bias potential. By the analysis of the IMPS data as discussed before, some mechanistic conclusions could be drawn about the nature of the intermediates involved in the photooxidation of water and/or methanol. In this section the photocatalytic activities of the different investigated electrodes have also been assessed, but in this case without any external bias potential, studying the $OH^\bullet$ radical generation and the photooxidation of methanol under UV(A) illumination. In fact, the electron transfer reactions at the interface of TiO_2 upon excitation by the light can be considered as a typical photoelectrochemical processes, with the TiO_2 surfaces being referred to as microelectrodes, although they are not part of an electrical circuit in the usual sense.

5.2.1. Photocatalytic Hydroxyl Radical Generation

The photocatalytic activities of the rutile single crystal (100), (001), (110) surfaces and the anatase single crystal (101) surface have been evaluated by the photocatalytic hydroxylation of terephthalic acid which is usually regarded as an indirect detection of $OH^\bullet$ radicals (see Eq. 3.2). Consequently, the $OH^\bullet$ radical formation at the TiO_2 surfaces has been detected by measuring the fluorescence intensity of 2-hydroxyterephthalic acid at 425 nm excited by 315 nm light. The single crystal surfaces have been immersed in standard rectangular quartz cuvettes containing 2 ml 4×10^{-4} M basic solution of terephthalic acid and have been illuminated by UV(A) light filtered

through 320 nm longpass cut-off filter for different illumination times using a high-pressure Xe-lamp. Terephthalic acid reacts with the OH$^\bullet$ radicals leading to the formation of 2-hydroxyterephthalic acid [105]. The change in the fluorescence spectra recorded for the terephthalic acid solution under UV illumination in the presence of the rutile and anatase surfaces are shown in Figure 4.22. The change in fluorescence intensity recorded for the basic terephthalic acid solution under UV(A) illumination at 315 nm as a function of irradiation time for the rutile (001), (100) and (110) surfaces and for anatase (101) surface are presented in Figure 5.11. The linear relationship between the fluorescence intensity and irradiation time observed in Figure 5.11 indicates that the amount of OH$^\bullet$ generated on the TiO$_2$ surface is proportional to the irradiation time during the photocatalytic process. Figure 5.11 clearly shows that the rate of OH$^\bullet$ radical formation on the anatase (101) surface is comparable to that on the rutile (001) surface and higher than that on the rutile (100) and (110) surfaces.

The lower reactivity of OH$^\bullet$ radicals generation on the rutile (110) surface in comparison to that on the anatase (101) surface is in agreement with the behavior observed on rutile and anatase powders reported by Hirakawa *et al* [116]. For example, comparing two of the investigated TiO$_2$ materials by Hirakawa *et al*., i.e., ST-21 (Ishihara, 100 % anatase, BET surface area 56.1 m^2 g^{-1}) [117] and PT101 (Ishihara, 100 % rutile, BET surface area 25 m^2 g^{-1}) [117], it is obvious that the formation rate of OH$^\bullet$ radicals, normalized to the BET surface area, on ST-21 is approx. 3 times higher than that on PT101. In the present results, the formation rate of OH$^\bullet$ radicals, normalized to the surface area, on the anatase (101) surface is ca. 2.8 times higher than that on the rutile (110) surface. This good agreement with the ratio of the formation rates of OH$^\bullet$ radicals on anatase and rutile powders and the ratio of the formation rates of OH$^\bullet$ radicals on anatase (101) and rutile (110) surfaces, can

be explained by the fact that anatase (101) and rutile (110) are the thermodynamically most stable surfaces, and hence, anatase and rutile powders possess, thus, a large percentage of (101) and (110) surfaces, respectively. This might support the importance of the exposed surface on the photocatalytic activity and highlight the importance of investigating different well-defined surfaces and comparing the results with nanomaterials exhibiting the corresponding exposed surface.
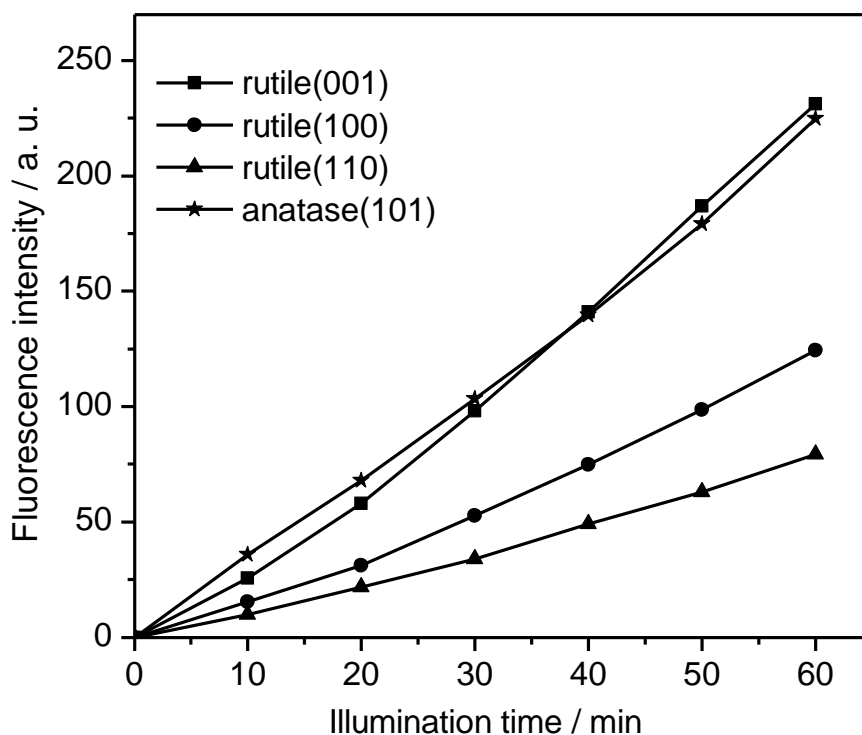
Figure 5.11. Fluorescence intensity of 4×10^{-4} M basic solution of terephthalic acid at 425 nm as a function of the illumination time; excitation wavelength 315 nm, illuminated area of rutile and anatase surfaces are 0.25 and 0.09 cm^2, respectively. Note: the fluorescence intensity on the anatase surface has been normalized to 0.25 cm^2.

5.2.2. Photocatalytic Methanol Oxidation

The photocatalytic activities of the rutile and the anatase TiO_2 single crystal surfaces have also been assessed by the photocatalytic oxidation of methanol. Methanol is photocatalytically oxidized to formaldehyde according to Eq. 2.7 to 13. The produced formaldehyde has been analyzed employing HPLC using the Nash reagent [106]. Figure 4.23 in the results section 4.3 shows the time course of formaldehyde formation on the different TiO_2 single crystal surfaces. It is obvious from the results shown in this Figure that the anatase (101) surface exhibits a higher photocatalytic activity than any of the investigated rutile surfaces. The photonic efficiencies (ζ) of the methanol photooxidation on the different TiO_2 single crystal surfaces have been calculated by dividing the rate of formaldehyde formation (r) by the incident photon flux (I_0) according to the following equation [118]:

$$\zeta = r \times 100 / I_0 \qquad\qquad\qquad\qquad \text{(Eq. 5.3)}$$

The incident photon flux per 0.25 cm^2 of illuminated surface area has been calculated to be 1.54 µEinstein min^{-1} based upon the UV-A light meter measurements and assuming an average illumination wavelength of $\lambda=350$ nm. The rates of formaldehyde formation (µmol min^{-1} per 0.25 cm^2 of electrode surface area) have been calculated from the slope of the time course of formaldehyde formation presented in Figure 4.23. The photonic efficiency of the anatase (101) surface has been calculated to be $\zeta= 0.190$ %, while the photonic efficiencies of the rutile (100), (001), and (110) surfaces have been calculated to be $\zeta= 0.110, 0.153$, and 0.089 %, respectively. The results are present in Figure 5.12. The photonic efficiency values of all well-defined TiO_2 surfaces investigated here are higher than the reported value ($\zeta= 0.036$)

[119] for methanol photooxidation on nanocrystalline TiO_2 layers and also higher than the reported values for methylene blue photodegradation on anatase and on Pilkington Active[®] films [120], evincing that a tuning of the exposed surface should be possible to further enhance the photocatalytic activity of TiO_2 coatings.
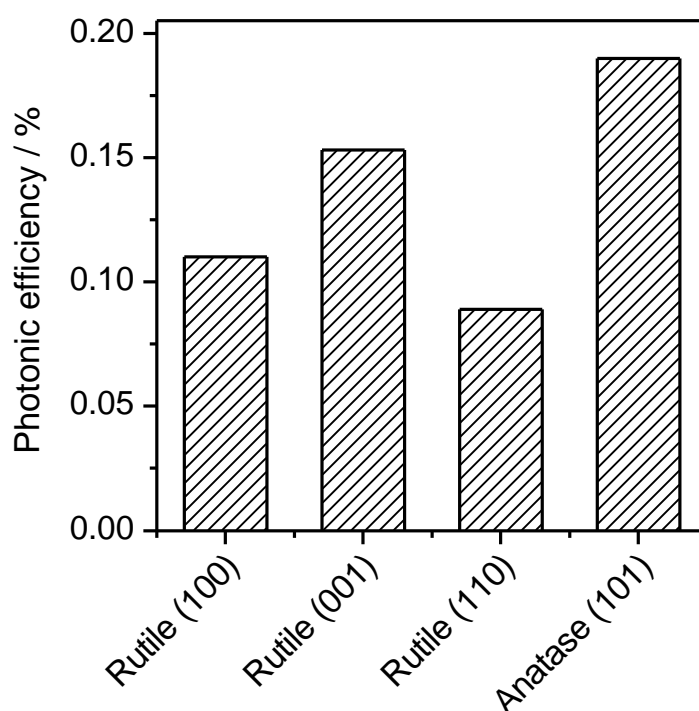
Figure 5.12. Photonic efficiencies of methanol oxidation to formaldehyde on different TiO_2 single crystal surfaces under 35 mW/cm^2 UV(A) illumination; illuminated area of rutile and anatase surfaces are 0.25 and 0.09 cm^2, respectively. Note: the amount of formaldehyde formed on the anatase surface has been normalized to 0.25 cm^2.

By comparing the photocatalytic activities of OH[•] generation and methanol oxidation on rutile and anatase surfaces, it is obvious that the trend of OH[•] generation is the same as that observed for the photocatalytic oxidation of methanol except that anatase (101) and rutile (001) exhibit about the same photocatalytic activities toward OH[•] generation. The higher activity of the

photocatalytic methanol oxidation on the anatase (101) surface as compared with that on the rutile (001) surface despite the fact that both surfaces show the same OH$^\bullet$ radical generation activity, can be explained assuming that the photogenerated OH$^\bullet$ radicals on the anatase (101) surface are more reactive than those on the rutile (001) surface at least towards methanol photooxidation.

Since the photocatalytic tests have been carried out employing aqueous methanol solutions, there will be a competition between the direct photooxidation of methanol and that of water on the TiO_2 surfaces. According to the IMPS results presented in section 5.1, it is obvious that methanol is either directly oxidized by reacting with trapped holes (Case I) or by mobile OH$^\bullet$ (Case II) depending on the employing TiO_2 surface. Methanol reacts with surface trapped holes and/or OH$^\bullet$ radicals leading to the formation of $^\bullet CH_2OH$ radicals. The latter are further oxidized by reacting with molecular oxygen leading to the formation of formaldehyde. The possible reaction steps are illustrated in Figure 5.13.
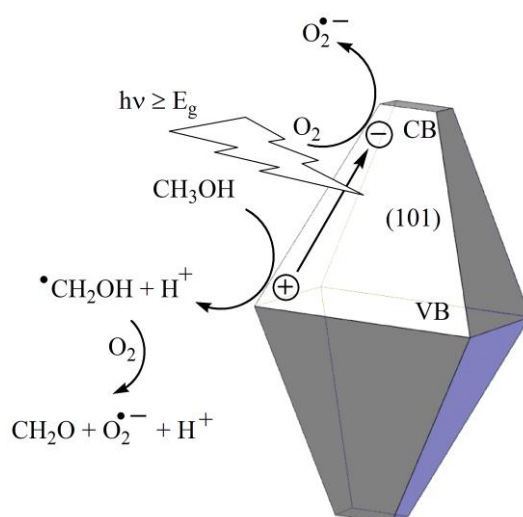
Figure 5.13. Scheme representing the photocatalytic steps of methanol photooxidation on the anatase TiO_2 single crystal (101) surface. Note: for simplicity, the formation of hydroxymethyl radicals ($^\bullet CH_2OH$) by OH$^\bullet$ radicals is represented by the hole oxidation step.

5.3. Correlation between the IMPS and the Photocatalytic Activity Results

When comparing the photolectrochemical and the photocatalytic activity results it is important to note, however, that the former have been obtained under bias potential in a three electrode cell while the latter have been obtained from photocatalytic measurements without any bias potential. There are two main observations:

Firstly, it could be observed from the IMPS analysis that on all investigated TiO_2 single crystal surfaces, i.e., rutile (100), (001) and (110) or anatase (101), the photoelectrochemical oxidation of water proceeds through Case II, i.e., the coupling of two surface mobile $OH_s^{\bullet}$ radicals and hence the formation of peroxide species as intermediates. This is in agreement with the mechanism proposed for the water photooxidation at TiO_2 surfaces (see section 2.3.3). In the presence of methanol, the rutile (001) and anatase (101) still behave like in the absence of methanol Case II, while the rutile (100) and (110) surfaces behave according to Case I where the $OH^{\bullet}$ radical reaction with methanol dominates. Comparing these mechanistic aspects with the rates of the photocatalytic $OH_s^{\bullet}$ radical generation and the methanol oxidation on TiO_2 single crystal surfaces, it is obvious that anatase (101) and rutile (001) exhibit the highest photocatalytic activities. At the same time these are the same surfaces where a coupling of surface mobile $OH_s^{\bullet}$ radicals was seen in the IMPS results. It was also found from the IMPS results that the recombination rate on these two surfaces are the lowest among all of the investigate surfaces, evincing that reaction of surface mobile $OH_s^{\bullet}$ radicals with each other mediate the charge transfer and reduce the recombination processes. This agrees well with the fact that the peroxide species in the TiO_2 photocatalytic system accelerate the $OH_s^{\bullet}$ radicals formation thus improving the photocatalytic activity [116]. The coupling of two $OH_s^{\bullet}$ at the anatase (101) and the rutile

(001) surfaces can thus enhance the rate of $OH_s^{\bullet}$ radical generation on these two surface in comparison with the other investigated surfaces as indeed observed here (see Figure 5.11). In the photocatalytic system in the presence of molecular oxygen, the $OH_s^{\bullet}$ radical generation from peroxide species proceeds usually by the reduction by conduction band electron, e_{CB}^{-}, or by the reaction with superoxide radicals, $O_2^{\bullet-}$, as shown in the following:

$$H_2O_2 + e_{CB}^{-} \longrightarrow OH^{\bullet} + OH^{-} \qquad\qquad \text{(Eq. 5.4)}$$

$$H_2O_2 + O_2^{\bullet-} \longrightarrow OH^{\bullet} + OH^{-} + O_2 \qquad\qquad \text{(Eq. 5.5)}$$
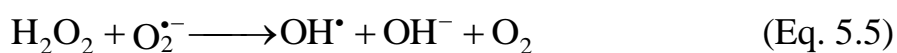
Furthermore, H_2O_2 can also be oxidized by valence band holes according to the following reactions:

$$H_2O_2 + h_{VB}^{+} + 2OH^{-} \longrightarrow O_2^{\bullet-} + 2H_2O \qquad\qquad \text{(Eq. 5.6)}$$

$$H_2O_2 + OH^{\bullet} + OH^{-} \longrightarrow O_2^{\bullet-} + 2H_2O \qquad\qquad \text{(Eq. 5.7)}$$
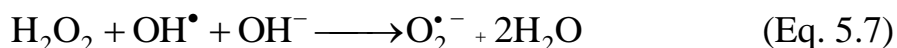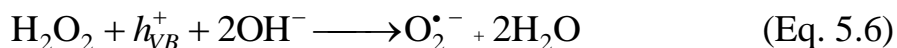
Secondly, it was observed that the photocurrent on the anatase (101) surface is smaller than that of all investigated rutile surfaces; however, the anatase surface has a higher photocatalytic activity. This behaviour could be explained by the higher band gap energy of anatase (3.2 eV) as compared with that of rutile (3.0 eV) which allows more light to be absorbed in the rutile case. This is in agreement with the results published by Kavan et al. [108].

6. Final Conclusions and Outlook

Analysis of the IMPS results shows that water photooxidation proceeds via mobile surface $OH_s^{\bullet}$ radicals on all investigated surfaces, while methanol addition leads to different properties, according to which the surfaces can be divided into two groups, denoted as group A and group B surfaces in the following:

At group A surfaces, which include the rutile (100) and (110) surfaces and the anatase thin-film, methanol addition gives rise to the involvement of immobile $OH_s^{\bullet}$ radicals. Detailed analysis in view of the surface structures suggests that this observation is due to efficient electron transfer from bridging $OH_s^{\bullet}$ radicals on the group A surfaces to methanol, while coupling of two of these radicals occurs in the absence of methanol, making them appear as mobile $OH_s^{\bullet}$ radicals. At group B surfaces, which include the rutile (001) and the anatase (101) surfaces, the coupling reaction of two surface $OH_s^{\bullet}$ radicals has higher rate constants than at the group A surfaces, while lower rate constants are observed for the hole transfer from surface $OH_s^{\bullet}$ radicals to methanol. Consequently, group B surfaces are dominated by the coupling of $OH_s^{\bullet}$ radicals even in the presence of methanol. In the case of the rutile (001) surface, this is explained by the smaller distance between the bridging oxygen anions occupying adjacent positions as compared with the other two rutile surfaces, making the reaction of two adjacent $OH_s^{\bullet}$ radicals more likely. In the case of the anatase (101) surface, it is attributed to the saw tooth profile structure which might geometrically facilitate the coupling of two $OH_s^{\bullet}$ radicals.

Looking at the overall photocatalytic activities, a higher efficiency towards the formation of free $OH^{\bullet}$ radicals in solution and the photooxidation of methanol is seen in case of the group B surfaces, despite their lower rate

constant of direct hole transfer to methanol. The higher photocatalytic activity of the group B surfaces is, however, in a good agreement with the lower rate constants of recombination seen for these surfaces in the IMPS measurements. Furthermore, the coupling of surface mobile $OH^{\bullet}_s$ radicals was found to be faster in case of these surfaces, evincing that this reaction mediates the overall photooxidation process. This eventually leads to a higher photocatalytic activity compared to surfaces with an efficient direct charge transfer from $OH^{\bullet}_s$ radicals to methanol but an inefficient coupling of surface $OH^{\bullet}_s$ radicals.

The results obtained here show that significant differences between differently oriented TiO_2 surfaces exist regarding their photocatalytic activity. Furthermore, IMPS has been proven to be a quite powerful tool to study the photoelectrochemical processes at these surfaces and to explain their different activities. In future studies, the investigations should be expanded to include different anatase surfaces, provided that suitable single crystal electrodes can be prepared. Since the anatase sol-gel films with a less defined surface were found to exhibit a lower photocatalytic activity than the anatase (101) single crystal surface, it can be expected that differently oriented anatase surfaces also exhibit different photocatalytic activities as found for the different rutile surfaces. Such investigations will also be important to better understand the factors determining the photocatalytic activity of anatase surfaces, since the rather high efficiency of surface $OH^{\bullet}_s$ radical coupling despite the rather large distance between them (compared to rutile surfaces) indicates that other geometrical factors of the surfaces may also play a role.

Finally, the detailed knowledge of reaction mechanisms and its connection with the photocatalytic activities of different TiO_2 surfaces gained by this and the further proposed studies can be used to improve commercial TiO_2-based

photocatalysts. Since TiO_2 nanomaterials are usually used in technical applications due to their much higher surface area, the preparation of well-defined nanoparticles containing, compared to their overall surfaces, a high fraction of the most active surfaces will be of great interest.

7. References

[1] Fujishima, A.; Honda, K., Electrochemical photolysis of water at a semiconductor electrode. *Nature* **1972,** *238*, 37.

[2] Nozik, A. J., Photoelectrolysis of water using semiconducting TiO_2 crystals. *Nature* **1975,** *257* (5525), 383-386.

[3] Salvador, P.; Decker, F., On the generation of H_2O_2 during water photoelectrolysis at n-TiO_2. *J. Phys. Chem.* **1984,** *88* (25), 6116-6120.

[4] Salvador, P., Kinetic approach to the photocurrent transients in water photoelectrolysis at n-TiO_2 electrodes .1. Analysis of the ratio of the instantaneous to steady-state photocurrent. *J. Phys. Chem.* **1985,** *89* (18), 3863-3869.

[5] Tafalla, D.; Salvador, P.; Benito, R. M., Kinetic approach to the photocurrent transients in water photoelectrolysis at n-TiO_2 electrodes .2. Analysis of the photocurrent-time dependence. *J. Electrochem. Soc.* **1990,** *137* (6), 1810-1815.

[6] Jaeger, C. D.; Bard, A. J., Spin trapping and electron-spin resonance detection of radical intermediates in the photo-decomposition of water at TiO_2 particulate systems. *J. Phys. Chem.* **1979,** *83* (24), 3146-3152.

[7] Sato, S.; White, J. M., Photo-decomposition of water over p- TiO_2 catalysts. *Chem. Phys. Lett.* **1980,** *72* (1), 83-86.

[8] Mills, A.; Porter, G., Photosensitized dissociation of water using dispersed suspensions of n-type semiconductors. *J. Chem. Soc.-Faraday Trans. I* **1982,** *78*, 3659-3669.

[9] Kiwi, J.; Gratzel, M., Optimization of conditions for photochemical water cleavage - aqueous pt/TiO_2 (anatase) dispersions under ultraviolet-light. *J. Phys. Chem.* **1984,** *88* (7), 1302-1307.

[10] Hashimoto, K.; Irie, H.; Fujishima, A., TiO_2 photocatalysis: A historical overview and future prospects. *Japn. J. Appl. Phys.* **2005,** *44* (12), 8269-8285.

[11] Fujishima, A.; Zhang, X.; Tryk, D. A., Heterogeneous photocatalysis: From water photolysis to applications in environmental cleanup. *Int. J. Hydrogen Energy* **2007,** *32* (14), 2664-2672.

[12] Bahnemann, D., Photocatalytic water treatment: Solar energy applications. *Solar Energy* **2004,** *77* (5), 445-459.

[13] Maness, P. C.; Smolinski, S.; Blake, D. M.; Huang, Z.; Wolfrum, E. J.; Jacoby, W. A., Bactericidal activity of photocatalytic TiO_2 reaction: Toward an understanding of its killing mechanism. *Appl. Environ. Microbiol.* **1999,** *65* (9), 4094-4098.

[14] Paz, Y.; Luo, Z.; Rabenberg, L.; Heller, A., Photooxidative self-cleaning transparent titanium-dioxide films on glass. *J. Mater. Res.* **1995,** *10* (11), 2842-2848.

[15] Poulios, I.; Spathis, P.; Grigoriadou, A.; Delidou, K.; Tsoumparis, P., Protection of marbles against corrosion and microbial corrosion with TiO$_2$ coatings. *J. Environ. Sci. Health A* **1999,** *34* (7), 1455-1471.

[16] Cai, R.; Hashimoto, K.; Itoh, K.; Kubota, Y.; Fujishima, A., Photokilling of malignant-cells with ultrafine TiO$_2$ powder. *Bull. Chem. Soc. Jpn.* **1991,** *64* (4), 1268-1273.

[17] Fujishima, A.; Cai, R.; Hashimoto, K.; Sakai, H.; Kubota, Y., Biochemical application of TiO$_2$ photocatalysts. In *Photocatalytic purification and treatment of water and air*, Ollis, D. F.; Alekabi, H., Eds. Elsevier Science Ltd: **1993**; Vol. 3, pp 193-205.

[18] Sakai, H.; Baba, R.; Hashimoto, K.; Kubota, Y.; Fujishima, A., Selective killing of a single cancerous T24 cell with TiO$_2$ semiconducting microelectrode under irradiation. *Chem. Lett.* **1995,** (3), 185-186.

[19] Mills, A.; Davies, R. H.; Worsley, D., Water-purification by semiconductor photocatalysis. *Chem. Soc. Rev.* **1993,** *22* (6), 417-425.

[20] Hoffmann, M. R.; Martin, S. T.; Choi, W. Y.; Bahnemann, D. W., Environmental applications of semiconductor photocatalysis. *Chem. Rev.* **1995,** *95* (1), 69-96.

[21] Peter, L. M., Dynamic aspects of semiconductor photoelectrochemistry. *Chem. Rev.* **1990,** *90* (5), 753-769.

[22] Linsebigler, A. L.; Lu, G. Q.; Yates, J. T., Photocatalysis on TiO$_2$ surfaces - principles, mechanisms, and selected results. *Chem. Rev.* **1995,** *95* (3), 735-758.

[23] Fujishima, A.; Rao, T. N.; Tryk, D. A., Titanium dioxide photocatalysis. *J. Photochem. Photobiol. C: Photochem. Rev.* **2000,** *1*, 1-21.

[24] Thompson, T. L.; Yates, J. T., Surface science studies of the photoactivation of TiO$_2$-new photochemical processes. *Chem. Rev.* **2006,** *106* (10), 4428-4453.

[25] Ohtani, B., Photocatalysis A to Z-what we know and what we do not know in a scientific sense. *J. Photochem. Photobiol. C:Photochem. Rev.* **2010,** *11* (4), 157-178.

[26] Salvador, P., Mechanisms of water photooxidation at n-TiO$_2$ rutile single crystal oriented electrodes under uv illumination in competition with photocorrosion. *Prog. Surf. Sci.* **2011,** *86* (1-2), 41-58.

[27] Prieto-Mahaney, O. O.; Murakami, N.; Abe, R.; Ohtani, B., Correlation between photocatalytic activities and structural and physical properties of titanium(iv) oxide powders. *Chem. Lett.* **2009,** *38* (3), 238-239.

[28] Morrison, S. R., *Electrochemistry at semiconductor and oxidized metal electrodes.* Plenum Press: New York, **1980**.

[29] Memming, R., *Semiconductor electrochemistry*. Wiley-VCH Verlag GmbH: Weinheim, **2001**.

[30] Rajeshwar, K., Fundamentals of semiconductor electrochemistry and photoelectrochemistry. In *Encyclopedia of electrochemistry*, Bard, A. L.; Stratmann, M.; Licht, S., Eds. Wiley-VCH Verlag GmbH & Co. KGaA: Weinheim, **2002**; Vol. 6, pp 1-30.

[31] Pankove, J., *Optical processes in semiconductors*. Dover Publ. Inc.: New York, **1976**.

[32] Hamnett, A.; Compton, R. G., Chapter 2 semiconductor electrochemistry. In *Comprehensive chemical kinetics*, Elsevier B. V.: **1988**; Vol. 27, pp 61-246.

[33] Pleskov, Y. V.; Gurevich, Y. Y., *Semiconductor photoelectrochemistry*. **1986**.

[34] Tan, M. X.; Laibinis, P. E.; Nguyen, S. T.; Kesselman, J. M.; Stanton, C. E.; Lewis, N. S., Principles and applications of semiconductor photoelectrochemistry. *Prog. Inorg. Chem.,* **1994**, *41*, 21-144.

[35] Kuznetsov, A. M., *Charge transfer in physics, chemistry and biology: Physical mechanisms of elementary processes and an introduction to the theory*. CRC Press: **1995**.

[36] Miller, R. J. D.; McLendon, G. L.; Nozik, A. J.; Schmickler, W.; Willig, F., *Surface electron transfer processes*. Wiley-VCH Verlag GmbH & Co. KGaA: Weinheim, **1995**.

[37] Schmickler, W., *Interfacial electrochemistry*. Oxford Univ Press: New York, **1996**.

[38] Memming, R., Photoelectrochemical solar-energy conversion. *Top. Curr. Chem.* **1988**, *143*, 79-112.

[39] Gratzel, M., The artificial leaf, molecular photovoltaics achieve efficient generation of electricity from sunlight. *Coord. Chem. Rev.* **1991**, *111*, 167-174.

[40] Oregan, B.; Gratzel, M., A low-cost, high-efficiency solar-cell based on dye-sensitized colloidal TiO_2 films. *Nature* **1991**, *353* (6346), 737-740.

[41] Kay, A.; Gratzel, M., Low cost photovoltaic modules based on dye sensitized nanocrystalline titanium dioxide and carbon powder. *Sol. Energy Mater. Sol. Cells* **1996**, *44* (1), 99-117.

[42] Newman, J. S.; Thomas-Alyea, K. E., *Electrochemical systems*. J. Wiley: **2004**.

[43] Peter, L. M.; Vanmaekelbergh, D., Time and frequency resolved studies of photoelectrochemical kinetics. In *Advances in electrochemical science and engineering*, Alkire, R. C.; Kolb, D. M., Eds. Wiley-VCH Verlag GmbH: Weinheim, **1999**; Vol. 6, pp 77-163.

[44] Gartner, W. W., Depletion-layer photoeffects in semiconductors. *Phys. Rev.* **1959**, *116* (1), 84-87.

[45] Ramamoorthy, M.; Vanderbilt, D.; Kingsmith, R. D., 1st-principles calculations of the energetics of stoichiometric TiO_2 surfaces. *Phys. Rev. B* **1994,** *49* (23), 16721-16727.

[46] Diebold, U., The surface science of titanium dioxide. *Surf. Sci. Rep.* **2003,** *48* (5-8), 53-229.

[47] Vittadini, A.; Selloni, A.; Rotzinger, F. P.; Gratzel, M., Structure and energetics of water adsorbed at TiO_2 anatase (101) and (001) surfaces. *Phys. Rev. Lett.* **1998,** *81* (14), 2954-2957.

[48] Lindan, P. J. D.; Harrison, N. M.; Gillan, M. J., Mixed dissociative and molecular adsorption of water on the rutile (110) surface. *Phys. Rev. Lett.* **1998,** *80* (4), 762-765.

[49] Ramamoorthy, M.; Vanderbilt, D.; King-Smith, R. D., First-principles calculations of the energetics of stoichiometric TiO_2 surfaces. *Phys. Rev. B* **1994,** *49* (23), 16721.

[50] Bredow, T.; Jug, K., Theoretical investigation of water-adsorption at rutile and anatase surfaces. *Surf. Sci.* **1995,** *327* (3), 398-408.

[51] Lazzeri, M.; Vittadini, A.; Selloni, A., Structure and energetics of stoichiometric TiO_2 anatase surfaces. *Phys. Rev. B* **2001,** *63* (15).

[52] Lazzeri, M.; Vittadini, A.; Selloni, A., Structure and energetics of stoichiometric TiO_2 anatase surfaces (vol 63, art no 155409, 2001). *Phys. Rev. B* **2002,** *65* (11).

[53] Diebold, U.; Ruzycki, N.; Herman, G. S.; Selloni, A., One step towards bridging the materials gap: Surface studies of TiO_2 anatase. *Catal. Today* **2003,** *85* (2-4), 93-100.

[54] Henrich, V. E.; Kurtz, R. L., Surface electronic-structure of TiO_2 - atomic geometry, ligand coordination, and the effect of adsorbed hydrogen. *Phys. Rev. B* **1981,** *23* (12), 6280-6287.

[55] Henderson, M. A., Structural sensitivity in the dissociation of water on TiO_2 single-crystal surfaces. *Langmuir* **1996,** *12* (21), 5093-5098.

[56] Herman, G. S.; Dohnalek, Z.; Ruzycki, N.; Diebold, U., Experimental investigation of the interaction of water and methanol with anatase-TiO_2(101). *J. Phys. Chem. B* **2003,** *107* (12), 2788-2795.

[57] He, Y. B.; Tilocca, A.; Dulub, O.; Selloni, A.; Diebold, U., Local ordering and electronic signatures of submonolayer water on anatase TiO_2(101). *Nature Mater.* **2009,** *8* (7), 585-589.

[58] Felipe Montoya, J.; Peral, J.; Salvador, P., Surface chemistry and interfacial charge-transfer mechanisms in photoinduced oxygen exchange at O_2-TiO_2 interfaces. *Chemphyschem* **2011,** *12* (5), 901-907.

[59] Somasundaram, S.; Chenthamarakshan, C. R. N.; de Tacconi, N. R.; Rajeshwar, K., Photocatalytic production of hydrogen from electrodeposited p-Cu$_2$O film and sacrificial electron donors. *Int. J. Hydrogen Energy* **2007,** *32* (18), 4661-4669.

[60] Nian, J. N.; Hu, C. C.; Teng, H., Electrodeposited p-type Cu$_2$O for H$_2$ evolution from photoelectrolysis of water under visible light illumination. *Int. J. Hydrogen Energy* **2008,** *33* (12), 2897-2903.

[61] Kitano, M.; Tsujimaru, K.; Anpo, M., Hydrogen production using highly active titanium oxide-based photocatalysts. *Top. Catal.* **2008,** *49* (1-2), 4-17.

[62] Salvador, P., On the nature of photogenerated radical species active in the oxidative degradation of dissolved pollutants with TiO$_2$ aqueous suspensions: A revision in the light of the electronic structure of adsorbed water. *J. Phys. Chem. C* **2007,** *111* (45), 17038-17043.

[63] Fitts, J. P.; Machesky, M. L.; Wesolowski, D. J.; Shang, X. M.; Kubicki, J. D.; Flynn, G. W.; Heinz, T. F.; Eisenthal, K. B., Second-harmonic generation and theoretical studies of protonation at the water/alpha-TiO$_2$ (110) interface. *Chem. Phys. Lett.* **2005,** *411* (4-6), 399-403.

[64] Kurtz, R. L.; Stockbauer, R.; Madey, T. E.; Roman, E.; Desegovia, J. L., Synchrotron radiation studies of H$_2$O adsorption on TiO$_2$(110). *Surf. Sci.* **1989,** *218* (1), 178-200.

[65] Krischok, S.; Hofft, O.; Gunster, J.; Stultz, J.; Goodman, D. W.; Kempter, V., H$_2$O interaction with bare and Li-precovered TiO$_2$: Studies with electron spectroscopies (MIES and UPS(HeI and II)). *Surf. Sci.* **2001,** *495* (1-2), 8-18.

[66] Bogdanoff, P.; Alonsovante, N., A kinetic approach of competitive photoelectrooxidation of HCOOH and H$_2$O on TiO$_2$ anatase thin-layers via online mass detection. *J. Electroanal. Chem.* **1994,** *379* (1-2), 415-421.

[67] Harding, L. B., Theoretical-studies of the hydrogen-peroxide potential surface .2. An abinitio, long-range, OH($^2\Pi$) + OH($^2\Pi$) potential. *J. Phys. Chem.* **1991,** *95* (22), 8653-8660.

[68] Villarreal, T. L.; Gomez, R.; Gonzalez, M.; Salvador, P., A kinetic model for distinguishing between direct and indirect interfacial hole transfer in the heterogeneous photooxidation of dissolved organics on TiO$_2$ nanoparticle suspensions. *J. Phys. Chem. B* **2004,** *108* (52), 20278-20290.

[69] Villarreal, T. L.; Gomez, R.; Neumann-Spallart, M.; Alonso-Vante, N.; Salvador, P., Semiconductor photooxidation of pollutants dissolved in water: A kinetic model for distinguishing between direct and indirect interfacial hole transfer. I. Photoelectrochemical experiments with polycrystalline anatase electrodes under current doubling and absence of recombination. *J. Phys. Chem. B* **2004,** *108* (39), 15172-15181.

[70] Nogami, G.; Kennedy, J. H., Investigation of current doubling mechanism of organic-compounds by the rotating-ring disk electrode technique. *J. Electrochem. Soc.* **1989,** *136* (9), 2583-2588.

[71] Ohno, T.; Izumi, S.; Fujihara, K.; Masaki, Y.; Matsumura, M., Vanishing of current-doubling effect in photooxidation of 2-propanol on TiO_2 in solutions containing Fe(iii) ions. *J. Phys. Chem. B* **2000,** *104* (29), 6801-6803.

[72] Mandelbaum, P. A.; Regazzoni, A. E.; Blesa, M. A.; Bilmes, S. A., Photo-electro-oxidation of alcohols on titanium dioxide thin film electrodes. *J. Phys. Chem. B* **1999,** *103* (26), 5505-5511.

[73] Hykaway, N.; Sears, W. M.; Morisaki, H.; Morrison, S. R., Current-doubling reactions on titanium-dioxide photoanodes. *J. Phys. Chem.* **1986,** *90* (25), 6663-6667.

[74] Fermin, D. J.; Ponomarev, E. A.; Peter, L. M., Dynamics of photo-processes at the n-TiO_2 aqueous electrolyte interface. In *Proceedings of the symposium on photoelectrochemistry*, ELECTROCHEMICAL SOCIETY INC: Pennington, **1997**; Vol. 97, pp 62-71.

[75] Sun, L. Z.; Bolton, J. R., Determination of the quantum yield for the photochemical generation of hydroxyl radicals in TiO_2 suspensions. *J. Phys. Chem.* **1996,** *100* (10), 4127-4134.

[76] Wang, C. Y.; Rabani, J.; Bahnemann, D. W.; Dohrmann, J. K., Photonic efficiency and quantum yield of formaldehyde formation from methanol in the presence of various TiO_2 photocatalysts. *J. Photochem. Photobiol. A: Chem.* **2002,** *148* (1-3), 169-176.

[77] Marugan, J.; Hufschmidt, D.; Lopez-Munoz, M. J.; Selzer, V.; Bahnemann, D., Photonic efficiency for methanol photooxidation and hydroxyl radical generation on silica-supported TiO_2 photocatalysts. *Appl. Catal. B: Environ.* **2006,** *62* (3-4), 201-207.

[78] Micic, O. I.; Zhang, Y. N.; Cromack, K. R.; Trifunac, A. D.; Thurnauer, M. C., Trapped holes on TiO_2 colloids studied by electron-paramagnetic-resonance. *J. Phys. Chem.* **1993,** *97* (28), 7277-7283.

[79] Micic, O. I.; Zhang, Y. N.; Cromack, K. R.; Trifunac, A. D.; Thurnauer, M. C., Photoinduced hole transfer from TiO_2 to methanol molecules in aqueous-solution studied by electron-paramagnetic-resonance. *J. Phys. Chem.* **1993,** *97* (50), 13284-13288.

[80] Wang, C. Y.; Groenzin, H.; Shultz, M. J., Direct observation of competitive adsorption between methanol and water on TiO_2: An in situ sum-frequency generation study. *J. Am. Chem. Soc.* **2004,** *126* (26), 8094-8095.

[81] Dutoit, E. C.; Cardon, F.; Gomes, W. P., Electrochemical reactions involving holes at illuminated TiO_2 (rutile) single-crystal electrode. *Berichte Der Bunsen-Gesellschaft-Phys. Chem. Chem. Phys.* **1976,** *80* (12), 1285-1288.

[82] Draper, R. B.; Fox, M. A., Titanium-dioxide photosensitized reactions studied by diffuse reflectance flash-photolysis in aqueous suspensions of TiO_2 powder. *Langmuir* **1990,** *6* (8), 1396-1402.

[83] Li, J.; Peter, L. M.; Potter, R., Photoelectrochemical response of TiO_2 pigmented membranes. *J. Appl. Electrochem.* **1984,** *14* (4), 495-504.

[84] Nogami, G.; Nishiyama, Y.; Nakamura, H., New approach to a rotating-ring disk electrode. *J. Electrochem. Soc.* **1988,** *135* (4), 877-884.

[85] Chazalviel, J. N., Electrochemical transfer via surface-states - a new formulation for the semiconductor electrolyte interface. *J. Electrochem. Soc.* **1982,** *129* (5), 963-969.

[86] Albery, W. J.; Bartlett, P. N.; Wilde, C. P., Modulated light studies of the electrochemistry of semiconductors - theory and experiment. *J. Electrochem. Soc.* **1987,** *134* (10), 2486-2491.

[87] Schefold, J., Impedance and intensity modulated photocurrent spectroscopy as complementary differential methods in photoelectrochemistry. *J. Electroanal. Chem.* **1992,** *341* (1-2), 111-136.

[88] Modestov, A. D.; Zhou, G. D.; Ge, H. H.; Loo, B. H., A study of copper electrode behavior in alkaline-solutions containing benzotriazole-type inhibitors by the photocurrent response method and intensity-modulated photocurrent spectroscopy. *J. Electroanal. Chem.* **1994,** *375* (1-2), 293-299.

[89] Goossens, A., Intensity-modulated photocurrent spectroscopy of thin anodic films on titanium. *Surf. Sci.* **1996,** *365* (3), 662-671.

[90] Oskam, G.; Schmidt, J. C.; Searson, P. C., Electrical properties of n-type (111) Si in aqueous $K_4Fe(CN)_4$ solution .2. Intensity modulated photocurrent spectroscopy. *J. Electrochem. Soc.* **1996,** *143* (8), 2538-2543.

[91] Schlichthorl, G.; Park, N. G.; Frank, A. J., Estimation of the charge-collection efficiency of dye-sensitized nanocrystalline TiO_2 sol. cells. *Z. Phys. Chem.* **1999,** *212*, 45-50.

[92] Li, J.; Peter, L. M., Surface recombination at semiconductor electrodes .3. Steady-state and intensity modulated photocurrent response. *J. Electroanal. Chem.* **1985,** *193* (1-2), 27-47.

[93] de Jongh, P. E.; Vanmaekelbergh, D., Investigation of the electronic transport properties of nanocrystalline particulate TiO_2 electrodes by intensity-modulated photocurrent spectroscopy. *J. Phys. Chem. B* **1997,** *101* (14), 2716-2722.

[94] Semenikhin, O. A.; Kazarinov, V. E.; Jiang, L.; Hashimoto, K.; Fujishima, A., Suppression of surface recombination on TiO_2 anatase photocatalysts in aqueous solutions containing alcohol. *Langmuir* **1999,** *15* (11), 3731-3737.

[95] Oekermann, T.; Schlettwein, D.; Jaeger, N. I., Charge transfer and recombination kinetics at electrodes of molecular semiconductors investigated by intensity modulated photocurrent spectroscopy. *J. Phys. Chem. B* **2001,** *105* (39), 9524-9532.

[96] Peat, R.; Peter, L. M., A study of the passive film on iron by intensity modulated photocurrent spectroscopy. *J. Electroanal. Chem.* **1987,** *228* (1-2), 351-364.

[97] Gartner, W. W., Depletion-layer photoeffects in semiconductors. *Phys. Rev.* **1959,** *116* (1), 84-87.

[98] Peter, L. M.; Ponomarev, E. A.; Fermin, D. J., Intensity-modulated photocurrent spectroscopy: Reconciliation of phenomenological analysis with multistep electron transfer mechanisms. *J. Electroanal. Chem.* **1997,** *427* (1-2), 79-96.

[99] Ponomarev, E. A.; Peter, L. M., A comparison of intensity-modulated photocurrent spectroscopy and photoelectrochemical impedance spectroscopy in a study of photoelectrochemical hydrogen evolution at p-InP. *J. Electroanal. Chem.* **1995,** *397* (1-2), 45-52.

[100] Imanishi, A.; Suzuki, H.; Murakoshi, K.; Nakato, Y., Crystal-face dependence and photoetching-induced increases of dye-sensitized photocurrents at single-crystal rutile TiO_2 surfaces. *J. Phys. Chem. B* **2006,** *110* (42), 21050-21054.

[101] Imanishi, A.; Suzuki, H.; Ohashi, N.; Kondoh, H.; Ohta, T.; Nakato, Y., Pretreatment dependence of adsorption properties of merocyanine dye at rutile (110) and (100) TiO_2 surfaces studied by C K-Edge NEXAFS. *J. Phys. Chem. C* **2009,** *113* (39), 17254-17261.

[102] Arconada, N.; Duran, A.; Suarez, S.; Portela, R.; Coronado, J. M.; Sanchez, B.; Castro, Y., Synthesis and photocatalytic properties of dense and porous TiO_2-anatase thin films prepared by sol-gel. *Appl. Catal. B-Environ.* **2009,** *86* (1-2), 1-7.

[103] Hatchard, C. G.; Parker, C. A., A new sensitive chemical actinometer .2. Potassium ferrioxalate as a standard chemical actinometer. *Proc. R. Soc. Ser. A* **1956,** *235* (1203), 518-536.

[104] Kirk, A. D.; Namasivayam, C., Errors in ferrioxalate actinometry. *Anal. Chem.* **1983,** *55* (14), 2428-2429.

[105] Ishibashi, K.; Fujishima, A.; Watanabe, T.; Hashimoto, K., Detection of active oxidative species in TiO_2 photocatalysis using the fluorescence technique. *Electrochem. Commun.* **2000,** *2* (3), 207-210.

[106] Jones, S. B.; Terry, C. M.; Lister, T. E.; Johnson, D. C., Determination of submicromolar concentrations of formaldehyde by liquid chromatography. *Anal. Chem.* **1999,** *71* (18), 4030-4033.

[107] Tang, H.; Berger, H.; Schmid, P. E.; Levy, F.; Burri, G., Photoluminescence in TiO_2 anatase single-crystals. *Solid State Commun.* **1993,** *87* (9), 847-850.

[108] Kavan, L.; Gratzel, M.; Gilbert, S. E.; Klemenz, C.; Scheel, H. J., Electrochemical and photoelectrochemical investigation of single-crystal anatase. *J. Am. Chem. Soc.* **1996,** *118* (28), 6716-6723.

[109] Degryse, R.; Gomes, W. P.; Cardon, F.; Vennik, J., Interpretation of mott-schottky plots determined at semiconductor-electrolyte systems. *J. Electrochem. Soc.* **1975,** *122* (5), 711-712.

[110] Salvador, P., Hole diffusion length in n-TiO$_2$ single-crystals and sintered electrodes - photoelectrochemical determination and comparative-analysis. *J. Appl. Phys.* **1984,** *55* (8), 2977-2985.

[111] Sanjines, R.; Tang, H.; Berger, H.; Gozzo, F.; Margaritondo, G.; Levy, F., Electronic-structure of anatase TiO$_2$ oxide. *J. Appl. Phys.* **1994,** *75* (6), 2945-2951.

[112] Zallen, R.; Moret, M. P., The optical absorption edge of brookite TiO$_2$. *Solid State Commun.* **2006,** *137* (3), 154-157.

[113] Nosaka, Y.; Kishimoto, M.; Nishino, J., Factors governing the initial process of TiO$_2$ photocatalysis studied by means of in-situ electron spin resonance measurements. *J. Phys. Chem. B* **1998,** *102* (50), 10279-10283.

[114] Wang, R.; Sakai, N.; Fujishima, A.; Watanabe, T.; Hashimoto, K., Studies of surface wettability conversion on TiO$_2$ single-crystal surfaces. *J. Phys. Chem. B* **1999,** *103* (12), 2188-2194.

[115] Monllor-Satoca, D.; Gomez, R.; Gonzalez-Hidalgo, M.; Salvador, P., The "Direct-indirect" Model: An alternative kinetic approach in heterogeneous photocatalysis based on the degree of interaction of dissolved pollutant species with the semiconductor surface. *Catal. Today* **2007,** *129* (1-2), 247-255.

[116] Hirakawa, T.; Yawata, K.; Nosaka, Y., Photocatalytic reactivity for O$_2^{-\bullet}$ and OH$^\bullet$ radical formation in anatase and rutile TiO$_2$ suspension as the effect of H$_2$O$_2$ addition. *Appl. Catal. A: Gen.* **2007,** *325* (1), 105-111.

[117] Ohno, T.; Sarukawa, K.; Tokieda, K.; Matsumura, M., Morphology of a TiO$_2$ photocatalyst (Degussa, P-25) consisting of anatase and rutile crystalline phases. *J. Catal.* **2001,** *203* (1), 82-86.

[118] Salinaro, A.; Emeline, A. V.; Zhao, J. C.; Hidaka, H.; Ryabchuk, V. K.; Serpone, N., Terminology, relative photonic efficiencies and quantum yields in heterogeneous photocatalysis. Part ii: Experimental determination of quantum yields (technical report). *Pure Appl. Chem.* **1999,** *71* (2), 321-335.

[119] Gao, R. M.; Stark, J.; Bahnemann, D. W.; Rabani, J., Quantum yields of hydroxyl radicals in illuminated TiO$_2$ nanocrystallite layers. *J. Photochem. Photobiol. A-Chem.* **2002,** *148* (1-3), 387-391.

[120] Fateh, R.; Ismail, A. A.; Dillert, R.; Bahnemann, D. W., Highly active crystalline mesoporous TiO$_2$ films coated onto polycarbonate substrates for self-cleaning applications. *J. Phys. Chem. C* **2011,** *115* (21), 10405-10411.

8. Appendix

8.1. List of Symbols and Abbreviations

Symbol	Meaning	Usual dimension
A	Photocurrent amplitude	A cm^{-2}
A	Electrode area	cm^2
c	Speed of light (2.998 x 10^8)	m s^{-1}
C	Effective capacitance = $C_{SC}C_H/(C_{SC}+C_H)$	F cm^{-2}
C_H	Helmholtz capacitance	F cm^{-2}
C_{SC}	Space charge capacitance	F cm^{-2}
d	Thickness	cm
D_p	Hole diffusion coefficient	cm^2 s^{-1}
E	Energy / Electrode potential	V
E_{CB}	Energy of the lower edge of the conductance band	eV
E_F	Fermi level energy	eV
E_{FB}	Flatband potential	V
$E_{F,redox}$	Fermi level energy at equilibration	eV
E_g	Bandgab energy	eV
E_{ph}	Photon energy	eV
E_{VB}	Energy of the upper edge of the valence band	eV
f	Frequency	Hz
g	Gärtner flux	A cm^{-2}
h	Planck's constant	J s
h_f^+	Free holes	
i	Imaginary unit $i^2 = -1$	
I	Transmitted light intensity	W cm^{-2}
I_0	Incident light intensity	W cm^{-2}
I_1, I_2	Intersection with the real axis in IMPS plot	A
j_{photo}	Photocurrent density measured in external circuit	A cm^{-2}
k_B	Boltzmann´s constant	J K^{-1}
k_3	Pseudo first-order rate constant for the recombination	s^{-1}
k_3^0	Value of k_3 at the flatband potential	s^{-1}
k_4, k_5	Electrochemical rate constants	cm^2 s^{-1}

k_{tr}	Charge transfer rate constant	s^{-1}
k^{I}_{tr}	Charge transfer rate constant of Case I	s^{-1}
k^{II}_{tr}	Charge transfer rate constant of Case II	s^{-1}
k_{rec}	Recombination rate constant	s^{-1}
k^{I}_{rec}	Recombination rate constant of Case I	s^{-1}
k^{II}_{rec}	Recombination rate constant of Case II	s^{-1}
L_p	Diffusion length of holes in a semiconductor	cm
n_{bulk}	Bulk electron concentration	cm^{-3}
n_s	Surface electron concentration	cm^{-3}
n_x	Electron concentration	cm^{-3}
N_{CB}	Effective density of states in the conduction band	cm^{-3}
N_D	Donor density of the semiconductor	cm^{-3}
N_{VB}	Effective density of states valence band	cm^{-3}
p	Momentum	kg.m s^{-1}
p	Surface concentrations of holes	cm^{-3}
p_0	Steady state surface concentration of holes	cm^{-3}
q	Elementary charge	C
Q_{sc}	Photogenerated charge across the space charge layer	C cm^{-2}
Q_H	Photogenerated charge across the Helmholtz layer	C cm^{-2}
r	Rate of formation	mole s^{-1}
R	Resistance	Ohm
R_a	Roughness	nm
T	Temperature	K
W	Width of space charge layer	nm
X^+	Surface mobile intermediate	
X_0	Steady state concentration of surface mobile intermediate	cm^{-3}

Greek

α	Absorption coefficient	cm^{-1}
β	Empirical factor associated with Fermi-Level pinning	
ε	Dielectric constant of the semiconductor	
ε_0	Vacuum permittivity	F cm^{-1}
λ	Wavelength of light	nm

$\Delta\phi_{SC}$	Potential drop across the space charge layer	V
$\Delta\phi_{H}$	Potential drop across the Helmholtz layer	V
$\Delta\phi_{G}$	Potential drop across the Gouy layer	V
ΔV	Shift in Potential	V
Φ_0	Steady state quantum efficiency	%
θ	Angle in Bragg´s law	°
τ	RC time constant	s^{-1}
τ_n	Lifetime of electrons	s
τ_p	Lifetime of holes	s
ω	Radial frequency $2\Pi f$	Hz
ζ	Photonic efficiency	%

Abbreviations

AFM	Atomic force microscopy
FE-SEM	Field-emission scanning electron microscopy FE-SEM
FTO	Fluorine doped tin oxide
HPLC	High performance liquid chromatography
IMPS	Intensity modulated photocurrent spectroscopy
LED	Light emitting diode
MIES	Metastable impact electron spectroscopy
SCL	Space charge layer
SFG	Sum frequency generation
UPS	Ultraviolet photoelectron spectroscopy
UV	Ultraviolet light
UV (A)	Ultraviolet light in the range from 315 nm to 380 nm
XRD	X-ray diffraction

8.2. List of Figures

8.3. List of Tables

8.4. Publications

8.4.1. Papers

1- **Amira Y. Ahmed**, Tarek A. Kandiel, Torsten Oekermann, and Detlef W. Bahnemann, Photocatalytic activities of different well-defined single crystal TiO_2 surfaces: Anatase versus rutile, *J. Phys. Chem. Lett.*, **2011,** 2 (19), 2461-2465.

2- **Amira Y. Ahmed**, Torsten Oekermann, Patrick Lindner, and Detlef W. Bahnemann, Comparison of the photoelectrochemical oxidation of methanol on rutile TiO_2 (001) and (100) single crystal faces studied by intensity modulated photocurrent spectroscopy, *PCCP*, **2012,** 14 (8), 2774-2783.

3- **Amira Y. Ahmed**, Torsten Oekermann, Tarek A. Kandiel, and Detlef W. Bahnemann, Mechanistic investigations of photoelectrochemical water and methanol oxidation on rutile TiO_2 (110) and anatase (101) single crystal surfaces studied by intensity modulated photocurrent spectroscopy, *in preparation*

8.4.2. Conferences

1- **Amira Y. Ahmed** and <u>Torsten Oekermann,</u> Investigation of photocatalytic reactions at TiO_2 electrodes using intensity-modulated photocurrent spectroscopy, Bunsentagung 2009, Köln Universität, 21-23 May **2009**, Köln, Germany.

2- **Amira Y. Ahmed**, <u>Tarek A. Kandiel</u>, Torsten Oekermann, and Detlef W. Bahnemann, Photocatalytic activities of different well-defined single crystal TiO_2 surfaces: Anatase versus rutile, 7th European Meeting on Solar Chemistry and Photocatalysis: Environmental Applications (SPEA7), 17-20 June **2012**, Oporto, Portugal.

8.5. Curriculum Vitae

Personal date:

Name   Amira Yehya Mohamed Ahmed

Date of Birth   01.10.1977

Gender   Female

Nationality   Egyptian

Marital Status Married, 3 children

Academic qualifications:

1999: Bachelor of Science in Chemistry, Chemistry Department, Faculty of Science (Sohag), South Valley University (Sohag Branch).

2001: Preliminary of Master of Science in Chemistry (Physical and Electrochemistry), Chemistry Department, Faculty of Science (Sohag), South Valley University (Sohag Branch).

2006: Master of Science in Chemistry, Chemistry Department, Faculty of Science (Sohag), South Valley University (Sohag Branch).

Work experience:

2001-2007: Teaching Assistant and Assistant Lecturer at the Chemistry Department, Faculty of Science (Sohag), South Valley University (Sohag Branch), Egypt.

2008-2012: PhD work at Institute of Physical Chemistry and Electrochemistry at Gottfried Wilhelm Leibniz University of Hannover, Germany.